UNIVERSITY OF CALIFORNIA
SANTA CRUZ

VERY-HIGH-ENERGY BLAZARS: A BROAD(BAND) PERSPECTIVE

A dissertation submitted in partial satisfaction of the requirements for the degree of

DOCTOR OF PHILOSOPHY

in

PHYSICS

by

Amy Kathryn Furniss

June 2013

The Dissertation of Amy Kathryn Furniss is approved:

Joel Primack, Chair

David A. Williams

Steven Ritz

Dean Tyrus Miller
Vice Provost and Dean of Graduate Studies

Table of Contents

List of Figures

List of Tables

Abstract

Very-High-Energy Blazars:

A Broad(band) Perspective

by

Amy Kathryn Furniss

Very high energy (VHE; $E \geq 100$ GeV) blazars are a type of active galaxy detected above 100 GeV with a jet pointed toward the observer. This work investigates VHE blazars through broadband observations, starting with a description of the VHE-discovery and time-independent modeling of the non-thermal emission from RX J0648.7+1516. Additionally, synchrotron self-Compton models are applied to six non-VHE blazars, with the VHE flux of each blazar being constrained by non-detection during observation by VERITAS. The general lack of physical measurements of model parameters is highlighted and a scheme of supplementary observations involving millimeter carbon monoxide (CO) luminosity and soft X-ray absorption measurements is explored for three VHE blazars. The limited sample supports a possible connection between the existence of CO in the vicinity of the blazar and additional soft X-ray absorption beyond what can be attributed to the Milky Way. RGB J0710+590 and W Comae both lack a significant level of CO and do not require additional absorption for the description of the soft X-ray

emission as observed by *Swift* XRT. 1ES 1959+650, on the other hand, shows a significant level of CO in the vicinity of the blazar and requires additional absorption to describe the soft X-ray emission. The positive detection of CO in the vicinity of 1ES 1959+650 is used as motivation to apply a mirrored emission scenario to broadband variability data. Limits on the redshifts of the two VHE blazars 3C 66A and PKS 1424+240 are derived from HST/COS observations of intervening Lyman absorption. These observations show 3C 66A to reside at a redshift below the tentative $z = 0.444$ at 99.9% confidence and reveal PKS 1424+240 to be the most distant VHE-detected blazar thus far. The redshift information is paired with VERITAS and *Fermi* Large Area Telescope gamma-ray observations to probe the density of the extragalactic background light and correct the observed gamma-ray spectra to the intrinsically emitted spectra, allowing insight into the acceleration mechanisms at work within the blazar jets and the propagation of gamma-ray photons through intergalactic space.

To Chris

Acknowledgments

First and foremost, I would like to thank my Mom and Dad. Their support and encouragement are the source of my strength and ambition. This degree is the product of a supportive family, and would not have been possible without my brother and sister, who never question my career choice and always remind me to relax. Throughout the completion of this work, Chris has gently encouraged me to stay true to myself, supported me through moments of self-doubt and kept me grounded, reminding me of what is truly important. Finally, I would like to thank the VERITAS Collaboration for the willingness to help me in the beginning of my studies and the encouragement to explore independently as I slowly build a foundation of rewarding research.

Part I

Introduction to the Study of Very-High-Energy Emitting Blazars

"...by observing with the vast panoply of sensors now available, they can see the processes in many different *lights* and hence thoroughly explore the phenomenon. It is thus advantageous to use every conceivable band of the electromagnetic spectrum at its maximum sensitivity."

– T. C. Weekes, *Very High Energy Gamma-ray Astronomy* (2003)

Blazars are one of the most violently variable astrophysical sources, exhibiting energetic particle processes far beyond that attainable by terrestrial accelerators. These extreme galaxies are understood to be active galactic nuclei, powered by accretion onto supermassive black holes and producing relativistic jets which are pointed within a few degrees of our line of sight (Urry & Padovani, 1995).

A number of blazars have been found to emit very high energy (VHE; E$\geq$ 100

GeV) photons[1] and are the most commonly detected extragalactic source above 100 GeV. A significant portion of the power released by VHE blazars is in the form of gamma rays, making the observation of the VHE spectral properties an important ingredient for understanding what type of relativistic processes and particle environments lead to VHE emission.

Blazars produce a non-thermal spectral energy distribution (SED), characterized by two broad peaks in the νF_ν representation. The source of the lower-energy peak is no mystery, resulting from synchrotron radiation of relativistic leptons in the presence of a tangled magnetic field. The origin of the higher-energy peak, however, has remained a source of scrutiny for more than 20 years.

The most common broadband blazar emission models attribute the higher-energy SED peak to inverse-Compton up-scattering of photons by relativistic leptons. This up-scattering can occur with either the synchrotron photons themselves, known as synchrotron self-Compton (SSC) emission, or a photon field external to the jet, known as external Compton (EC) emission. Alternative models attribute the higher-energy peak to hadronic pion production and the resulting cascade emission.

In order to determine which of these models is appropriate to describe the relativistic particle populations and emission processes at work within VHE gamma-ray jets, it is necessary to collect a broad overview of the multiwavelength char-

[1] `http://tevcat.uchicago.edu/`

acteristics of the VHE blazar population. Expanding the catalog of gamma-ray emitting AGN and having enough high-quality contemporaneous multiwavelength data to understand them remains a high priority and is an overarching goal of this work.

The relatively low number of VHE-detected blazars as compared to other wavebands can, in part, be explained by the fact that the field of view of imaging atmospheric Cherenkov telescopes (such as VERITAS) is limited to a few degrees, which is too small to easily survey the extragalactic sky. Moreover, blazars, which are the dominant population of extragalactic VHE sources are highly variable in every waveband and often reside in long-term faint states with short episodes of flaring activity.

The VHE emission is also absorbed by the lower-energy extragalactic background light (EBL) photons in a redshift and energy dependent manner. More specifically, VHE gamma rays which propagate through the intergalactic medium are absorbed by low energy EBL photons via pair production, $\gamma + \gamma \rightarrow e^+ + e^-$ (Nikishov, 1962; Gould & Shréder, 1967). There exists a strong correlation in energy between the VHE gamma rays and EBL photons with which they interact, such that for each energy band of low energy EBL photons, a band of VHE gamma rays has the highest probability for interaction. The absorption process deforms the intrinsic VHE gamma-ray spectra and results in a "gamma-ray hori-

zon," limiting the distance out to which VHE sources can be detected.

For several years, 3C 279 was the most distant VHE-detected blazar, residing at $z = 0.536$ (Marziani et al., 1996), observed above 50 GeV by MAGIC during a flare (Albert et al., 2008b). More recently, my work has led to the discovery that the VHE emitting blazar PKS 1424+240 resides at a redshift of $z \geq 0.6035$, making it the most distance VHE-detected blazar. PKS 1424+240 was discovered as a VHE emitting source (Acciari et al., 2010) after the launch of the *Fermi* Large Area Telescope (LAT; Atwood et al. (2009)).

The discovery of PKS 1424+240 at VHE is a prime example of using broad-band spectral characteristics for VHE-candidate selection. Historically, a number of methods have been utilized for VHE candidate selection, each using spectral information from other wavebands. These methods have been used to build a population of VHE-detected blazars over the last 20 years. A few of the more successful candidate lists include:

- Nearby (source redshift $z < 0.3$) BL Lac objects, recommended as potential VHE emitters by Costamante & Ghisellini (2002), Perlman (2000), and Stecker et al. (1996). The selection criteria utilized in these publications highlighted radio- and X-ray-bright blazars as prime VHE candidates.

- The X-ray brightest high-frequency-peaked BL Lac objects ($z < 0.3$) in the recent Sedentary (Giommi et al., 2005) and ROXA (Turriziani et al., 2007)

surveys were also highlighted as VHE-candidates.

The selection criteria applied in the past have proven to be successful, so far resulting in the detection of 24 of the 36 recommended targets. Additionally, half of all nearby EGRET-detected blazars have been detected by VHE instruments (Mukherjee, 2001).

More recently, the pair-conversion telescope *Fermi* LAT has presented a historic opportunity for the improved gamma-ray-based selection of possible VHE emitters. *Fermi* typically observes the entire sky between 100 MeV and 300 GeV every three hours with nearly ten times the sensitivity of its predecessor EGRET onboard the Compton Gamma Ray Observatory. Within the first eleven months of operation, over 1450 sources were detected at high significance (Abdo et al., 2010a), with a majority of these ($\sim$1300) being sources that were associated with AGN in the second *Fermi* catalog (Nolan et al., 2012). *Fermi* has now been in operation for more than four years, and the number of significantly detected sources continues to increase. Notably, all extragalactic VHE-detected sources have been detected by the *Fermi* LAT at more than 5 standard deviations (σ).

I used a method of TeV-candidate selection which concentrated on *Fermi*-detected sources. This selection process involved VHE flux estimates which were calculated by extrapolating the LAT power-law fits up to the VERITAS energy band while taking flux absorption by the leading EBL models into account. The

VERITAS observations of the *Fermi* LAT-selected candidates immediately resulted in the discovery of VHE emission from four blazars, namely PKS 1424+240, RBS 0413, 1ES 0502+675 and RX J0648.7+1516 (Acciari et al., 2010; Aliu et al., 2012a, 2013b, 2011b). The VHE detection of RX J0648.7+1516 is presented in Chapter 1 of this work. In addition to the successful TeV-blazar discoveries which resulted from this VHE extrapolation method, various non-detections also resulted, six of which are summarized in Chapter 2.

VERITAS blazar discoveries are often paired with contemporaneous broadband data collection, allowing the study of the non-thermal jet emission. A technique commonly used to investigate the extreme processes within VHE blazar jets is the application of non-thermal broadband emission models to contemporaneous data. These models routinely describe blazar emission with a region containing relativistic particles (a "blob") in the presence of a magnetic field and are most accurately applied when information regarding the main parameters is known. Namely, knowledge of the cosmological distance to the blazar, the emission mechanism and environment density as well as the identity of the constituent relativistic particles allow for a physically motivated application of the model. Unfortunately, the beamed, non-thermal emission from blazars makes the extraction of information on these model parameters difficult.

Some of the measurement challenges and possible methods for observationally

constraining these input parameters are summarized below:

- **Blazar Redshift:**

  Obtaining the cosmological distance to a blazar is not a simple task. Attempts to spectroscopically measure the redshift of some of the VHE-detected galaxies have been unsuccessful, which is not surprising considering that VHE blazars are most commonly of the BL Lacertae type that, by definition, display weak or no spectroscopic host galaxy lines. Out of the more than 30 known northern VHE emitting blazars, nearly one-third have an uncertain or unknown redshift[2].

  Alternative approaches to obtaining spectroscopic redshifts often focus on the brightness of the underlying host galaxy (e.g. Sbarufatti et al. (2005)) and can offer an estimate on the blazar redshift. These estimates are susceptible to large systematic error and depend sensitively on the presumed prior for the host galaxy luminosity function. In light of the featureless optical and UV spectra displayed by these targets, a technique using the blazar as a back-light for the observation of far UV low-redshift Lyman forest absorption features can be used to set strict lower limits and statistical upper limits on the distance of the blazar. More details regarding this method for red-

[2]A number of these have redshifts reported in NED or SIMBAD; however a careful review of the underlying literature, see e.g. Miller et al. (1978), reveals that they are highly uncertain or unreliable.

shift estimation and the cosmological studies made possible by knowledge of the VHE blazar distance will be provided in Part II of this work.

- **Blazar Emission Mechanism and Environment:**

  The photon and particle densities of the jet region responsible for the gamma-ray emission are parameters that might be accessible through the observation of the molecular carbon monoxide (CO) mass in the vicinity of the blazars with millimeter radio telescopes (Fumagalli et al., 2012), as done for three blazars in Furniss et al. (2013c). Only one of the three blazars investigated in the latter work shows a significant level of intrinsic molecular CO.

  A significant level of molecular mass requires the existence of an appreciable column density to shield the molecules from the non-thermal UV radiation from the jet that would otherwise photo-dissociate the CO. Therefore, detection of CO gas provides evidence that the blazar jet environment may not be devoid of matter. The thermal radiation from this matter can provide an external field of photons for Compton up-scattering by the relativistic particles.

  Insight into the emission environment, such as that which could be accessed through radio observations of CO line luminosity, might also provide a method to constrain the energy distribution of the highest energy particles

emitting synchrotron radiation in the X-ray band, a critical input parameter for blazar emission modeling. The blazar synchrotron radiation undergoes an energy-dependent absorption of soft X-rays by intervening gas. This intervening gas, routinely assumed to be solely within our own Galaxy, is characterized by a general neutral hydrogen column density for the convenience of the modeling. However, a portion of this intervening gas might also reside in the vicinity of, or along the extragalactic path to, the blazar.

The locality of any intervening gas is a critical component in the accurate modeling of the observed blazar emission. Without measurements such as CO line luminosity, the X-ray emission from blazars can be degenerately fit with two models, each resulting from a fundamentally different underlying relativistic particle energy spectrum. The first model is a power-law model which allows both Galactic and blazar neutral hydrogen densities, while the second model is a log-parabolic model absorbed solely by Galactic neutral hydrogen. According to photo-dissociation models, the blazar column density can be empirically derived from a relationship between neutral hydrogen and the blazar molecular CO line intensity (Young et al., 1991).

Moreover, the X-ray emission constraints provided by the radio observations can be used to extract information about the underlying acceleration mechanism. Due to its synchrotron origin, the emission observed by the

Swift X-ray Telescope (XRT) traces the energy spectrum of the emitting particles, meaning that the index of the log-parabolic or power-law model which is derived for the X-ray emission can be translated into the injection index (q) of the relativistic particles. Fundamentally different acceleration methods produce different indices. For example, indices within the range $2.2 < q < 2.3$ are derived from parallel shock acceleration (Achterberg et al., 2001), while harder ($1.7< q <2.0$) indices result from oblique subluminal, stochastic or spine/sheath type shocks (Summerlin et al., 2012; Virtanen et al., 2005). The unique combination of radio CO and synchrotron X-ray measurements might allow a possible path to elucidate the blazar particle population energetics (more specifically q) and the corresponding acceleration mechanisms within relativistic jets.

- **Blazar Constituent Particle Identity:**

  The non-thermal emission resulting from leptonic and hadronic models can produce nearly indistinguishable time-averaged SEDs. An effective method for differentiating between emission model degeneracies is through the simultaneous observation and subsequent time-dependent modeling of broadband spectral variability. Correlated variability between the lower and higher-energy SED peaks, for example, can be well described by leptonic SSC emission, whereas non-correlated variability patterns (such as the

"orphan" TeV flare displayed by 1ES 1959+650; Krawczynski et al. (2006)) require more complex, possibly hybrid leptonic/hadronic, emission models (e. g. Böttcher (2005); Dimitrakoudis et al. (2012)). Non-simultaneous observations do not provide the means to firmly characterize the particle acceleration or non-thermal emission mechanism at work within a blazar due to the rapidly varying nature of blazars (variability timescales as fast as a few minutes, as observed in PKS 2155-304; Aharonian et al. (2007)).

Part I of this work summarizes the contemporaneous observations and broadband modeling of the newly discovered VHE blazar RX J0648.7+1516 (Chapter 1) as well as the non-detection of six promising candidate VHE blazars selected from bright, hard high-energy spectral characteristics (Chapter 2). There is no observation of significant, model-constraining variability for RX J0648.7+1516 or the six non-detected blazars, and the lack of parameter constraint makes firm conclusions on the blazar non-thermal emission processes impossible. An attempt to probe the non-thermal emission environment and relativistic particle population is presented in Chapter 3, searching for signatures of soft X-ray absorption which might be occuring in the vicinity of three blazars which also have CO luminosity measurements. Finally, the insight gained from soft X-ray absorption in the VHE emitting blazar 1ES 1959+650 is applied to time-dependent modeling of broadband variability in Chapter 4.

Chapter 1

Multiwavelength Observations of the Previously Unidentified Blazar RX J0648.7+1516

This work has been published in the Astrophysical Journal (*Aliu E. et al. 2011, ApJ, 742, 127*). The corresponding author of the work is Amy Furniss. No content was modified aside from formatting. The full author list of this work can be found in Appendix A.

Abstract

We report on the VERITAS discovery of very-high-energy (VHE) gamma-ray emission above 200 GeV from the high-frequency-peaked BL Lac RX J0648.7+1516 (GB J0648+1516), associated with 1FGL J0648.8+1516. The photon spectrum above 200 GeV is fit by a power law $dN/dE = F_0(E/E_0)^{-\Gamma}$ *with a photon index* Γ *of* $4.4 \pm 0.8_{stat} \pm 0.3_{syst}$ *and a flux normalization* F_0 *of* $(2.3 \pm 0.5_{stat} \pm 1.2_{sys}) \times 10^{-11}$ $TeV^{-1} cm^{-2} s^{-1}$ *with* $E_0 = 300$ *GeV. No VHE variability is detected during VERITAS observations of RX J0648.7+1516 between 2010 March 4 and April 15. Following the VHE discovery, the optical identification and spectroscopic redshift were obtained using the Shane 3–m Telescope at the Lick Observatory, showing the unidentified object to be a BL Lac type with a redshift of* $z = 0.179$. *Broadband multiwavelength observations contemporaneous with the VERITAS exposure period can be used to sub-classify the blazar as a high-frequency-peaked BL Lac (HBL) object, including data from the MDM observatory, Swift-UVOT and XRT, and continuous monitoring at photon energies above 1 GeV from the Fermi Large Area Telescope (LAT). We find that in the absence of undetected, high-energy rapid variability, the one-zone synchrotron self-Compton model (SSC) overproduces the high-energy gamma-ray emission measured by the Fermi-LAT over 2.3 years. The SED can be parameterized satisfactorily with an external-Compton or lepto-hadronic model, which have two and six additional free parameters, respectively, compared to the one-zone SSC model.*

1.1 Introduction

1FGL J0648.8+1516 was detected by *Fermi*-LAT in the first 11 months of operation at greater than 10 standard deviations, σ (Abdo et al., 2010a). This source was flagged as a very-high-energy (VHE; E>100 GeV) emitting candidate by the *Fermi*-LAT collaboration by searching for $\geq$30 GeV photons. This information triggered the VERITAS observations reported here. 1FGL J0648.8+1516 is found to be associated with RX J0648.7+1516, which was first discovered by ROSAT (Brinkmann et al., 1997). A radio counterpart was identified in the NRAO Green Bank survey (Becker et al., 1991). Two subsequent attempts to identify an optical counterpart were unsuccessful (Motch et al., 1998; Haakonsen et al., 2009).

At 6° off the Galactic plane and without optical spectroscopy, the nature of this object remained unknown until optical spectroscopy was obtained in response to the VERITAS detection. These observations allow the active galactic nucleus (AGN) to be classified as a BL Lac, a type of AGN that has a jet co-aligned closely with the Earth's line of sight and displays weak emission lines. These AGN are characterized by non-thermal, double-peaked broadband spectral energy distributions (SED). Based on the radio and X-ray flux, the BL Lac can further be classified as a high-frequency-peaked BL Lac (HBL) (Padovani & Giommi, 1995), or if classified by the location of its low-energy peak, a high-synchrotron-peaked BL Lac (HSP) (Abdo et al., 2010c).

1.2 Observations and Analysis

1.2.1 VERITAS

VERITAS comprises four imaging atmospheric Cherenkov telescopes and is sensitive to gamma-rays between ∼100 GeV and ∼30 TeV (Weekes et al., 2002; Holder et al., 2006). The VERITAS observations of RX J0648.7+1516 were completed between 2010 March 4 and April 15 (MJD 55259-55301), resulting in 19.3 hours of quality-selected live time. These observations were taken at 0.5° offset in each of four directions to enable simultaneous background estimation using the reflected-region method (Fomin et al., 1994).

The VERITAS events are parameterized by the principal moments of the elliptical shower images, allowing cosmic-ray background rejection through a set of selection criteria (cuts) which have been optimized *a priori* on a simulated, soft-spectrum (photon index 4.0) source with a VHE flux 6.6% of that observed from the Crab Nebula. The cuts discard images with fewer than ∼50 photoelectrons. Events with at least two telescope images remaining are then cosmic-ray discriminated based on the mean-scaled-width (MSW) and the mean-scaled-length (MSL) parameters. Events with MSW < 1.1, MSL < 1.4, a height of maximum Cherenkov emission > 8 km and an angular distance to the reconstructed source position in the camera (θ) of less than 0.14 degrees are kept as gamma-ray candidate events.

The results are reproduced in two independent analysis packages (Cogan, 2008; Daniel, 2008). After background rejection, 2711 events remain in the source region, with 16722 events remaining in the background regions (larger by a factor of 6.89). The 283 excess events result in a significance of 5.2σ, calculated using Equation 17 from Li & Ma (1983).

A differential power law $dN/dE = F_o(E/300\ \mathrm{GeV})^{-\Gamma}$ is fit to the VERITAS data from 200 to 650 GeV, shown in the top panel of Figure 1.1. The fit ($\chi^2 = 0.90$ with 3 degrees of freedom (DOF), probability of 0.83) results in a flux normalization of $F_o = (2.3 \pm 0.5_{stat} \pm 1.2_{syst}) \times 10^{-11}$ photons cm^{-2} s^{-1} TeV^{-1} and an index of $\Gamma = 4.4 \pm 0.8_{stat} \pm 0.3_{syst}$, corresponding to 3.3% of the Crab Nebula flux above 200 GeV.

The angular distribution of the excess events is consistent with a point source now designated VER J0648+152, located at $102.19^\circ \pm 0.11^\circ_{stat}$ RA and $15.27^\circ \pm 0.12^\circ_{stat}$ Dec (J2000). The systematic pointing uncertainty of VERITAS is less than 25" (7×10^{-3} degrees). This position is consistent with the radio position of RX J0648.7+1516 (Becker et al., 1991). A nightly-binned VHE light curve is fit with a constant and shows a χ^2 null hypothesis probability of 0.39, showing no significant variability during the observation.

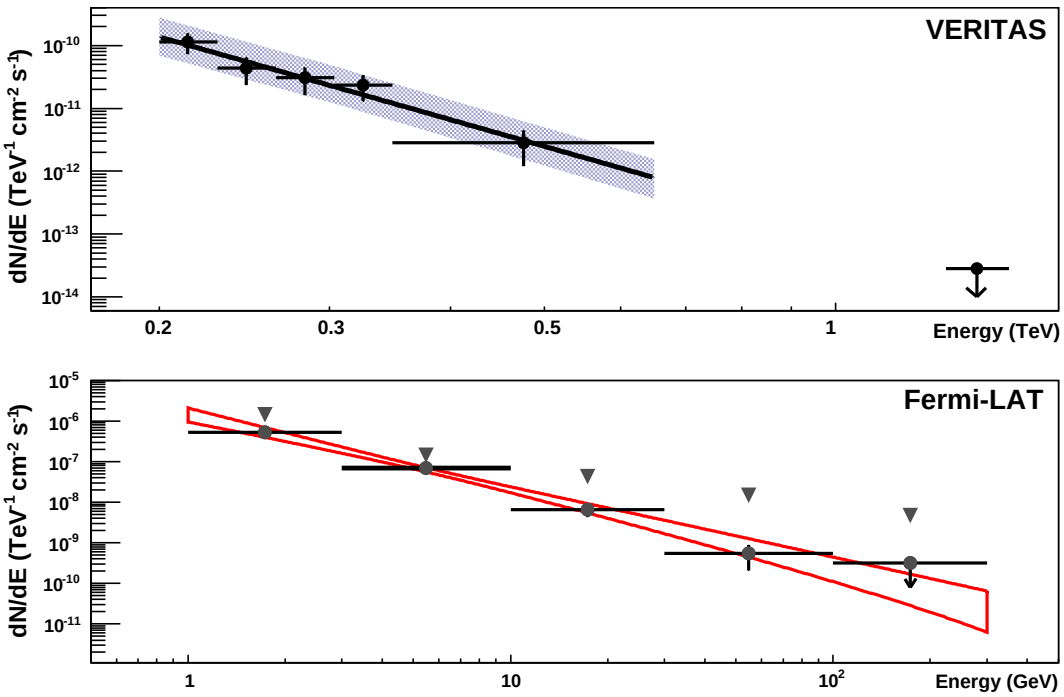

Figure 1.1: Top: The differential photon spectrum of RX J0648.7+1516 between 200 and 650 GeV measured by VERITAS between 2010 4 March and 15 April (MJD 55259–55301). The solid line shows a power-law fit to the measured flux derived with four equally log-spaced bins and a final bin boundary at 650 GeV, above which there are few on-source photons. A 99% confidence upper limit evaluated between 650 GeV and 5 TeV assuming a photon index of 4.4 is also shown. The shaded region shows the systematic uncertainty of the fit, which is dominated by 20% uncertainty on the energy scale. Bottom: The differential photon spectrum of RX J0648.7+1516 as measured by *Fermi*-LAT over 2.3 years between 2008 Aug 5 and 2010 Nov 17 (MJD 54683–55517, grey circles) with the highest energy bin containing a 95% confidence upper limit. *Fermi*-LAT upper limits from the VERITAS observation period are also shown (MJD 55259–55301, grey triangles).

1.2.2 *Fermi*-LAT

The *Fermi*-LAT is a pair-conversion telescope sensitive to photons between 20 MeV and several hundred GeV (Atwood et al., 2009; Abdo et al., 2009a). The data used in this paper encompass the time interval 2008 Aug 5 through 2010 Nov 17 (MJD 54683-55517), and were analyzed with the LAT `ScienceTools` software package version `v9r15p6`, which is available from the Fermi Science Support Center (FSSC). Only events from the "diffuse" class with energy above 1 GeV within a 5° radius of RX J0648.7+1516 and with a zenith angle $< 105°$ were used. The background was parameterized with the files gll_iem_v02.fit and isotropic_iem_v02.txt [1]. The normalizations of the components were allowed to vary freely during the spectral point fitting, which was performed with the unbinned likelihood method and using the instrument response function `P6_V3_DIFFUSE`.

The spectral fits using energies above 1 GeV are less sensitive to possible contamination from unaccounted (transient) neighboring sources, and hence have smaller systematic errors, at the expense of slightly reducing the number of source photons. Additionally, there is no significant signal from RX J0648.7+1516 below 1 GeV. The analysis of 2.3 years between 2008 Aug 5 and 2010 Nov 17 (MJD 54683–55517) of *Fermi*-LAT events with energy between 0.3–1 GeV (fixing the spectral index to 1.89) yields a test statistic (TS) of 9, corresponding to $\sim 3\sigma$ [2].

[1]The files are available at `http://fermi.gsfc.nasa.gov/ssc/data/access/lat/BackgroundModels.html`

[2]See Mattox et al. (1996) for TS definition.

In addition to the background, the emission model includes two nearby sources from the 1FGL catalog: the pulsars PSR J0659+1414 and PSR J0633+1746. The spectra from the pulsars are parameterized with power-law functions with exponential cutoffs, and the values are fixed to the values found from 18 months of data. The spectral fluxes are determined using an unbinned maximum likelihood method. The flux systematic uncertainty is estimated as 5% at 560 MeV and 20% at 10 GeV and above.[3]

The results from the *Fermi*-LAT spectral analysis are shown in the bottom panel of Figure 1.1. There is no variability detected in four time bins evenly spread over the 2.3 years of data. The dataset corresponding in time to the VERITAS observations between between 2010 March 4 and April 15 (i.e. MJD 55259−55301) does not show any significant signal and thus we report 2σ upper limits that were computed using the Bayesian method (Helene, 1983), where the likelihood is integrated from zero up to the flux that encompasses 95% of the posterior probability. When using the data accumulated over the expanded full 2.3 years of data, we find that 1FGL J0648.8+1516 is significantly detected above 1 GeV with a TS of 307. The spectrum is fit using a single power-law function with photon flux $F_{>1\,GeV} = (1.8 \pm 0.2_{stat}) \times 10^{-9}$ photons cm^{-2}s^{-1} and hard differential photon spectral index $\Gamma_{LAT} = 1.89 \pm 0.10_{stat}$. The analysis is also performed on five energy ranges equally spaced on a log scale with the photon index fixed to 1.89

[3]See `http://fermi.gsfc.nasa.gov/ssc/data/analysis/LAT_uscaveats.html`

and only fitting the normalization. The source is detected significantly (TS>25) in each energy bin except for the highest energy (100-300 GeV), for which a 95% confidence level upper limit is calculated.

1.2.3 *Swift*-XRT

The *Swift*-XRT (Gehrels et al., 2004; Burrows et al., 2005) data are analyzed with HEASOFT 6.9 and XSPEC version 12.6.0. Observations were taken in photon counting mode with an average count rate of ~ 0.3 counts per second and did not suffer from pile-up. Six target-of-opportunity observations summing to 10.5 ks were collected on six different days between 2010 March 18 and April 18 (MJD 55273 and 55304), inclusive. These observations were combined with a response file created from summing each observation's exposure file using *ximage*. The photons are grouped by energy to require a minimum of 30 counts per bin, and fit with an absorbed power law between 0.3 and 10 keV, allowing the neutral hydrogen (HI) column density to vary. A HI column density of $1.94 \pm 0.14 \times 10^{21}\mathrm{cm}^{-2}$ is found, only slightly higher than the $1.56 \times 10^{21}\mathrm{cm}^{-2}$ quoted in Kalberla et al. (2005). The combined X-ray energy spectrum is extracted with a fit ($\chi^2 = 114$ for 88 DOF, null hypothesis probability of 3.2×10^{-2}) with a photon index of 2.51 ± 0.06 and an integral flux between 0.3 and 10 keV of $(1.24 \pm 0.03_{\mathrm{stat}}) \times 10^{-11}$ ergs cm^{-2} s^{-1}. This corresponds to a 0.3 to 10 keV rest frame luminosity of 1.1×10^{45} ergs

s^{-1}. The deabsorbed spectrum is used to constrain modeling.

1.2.4 *Swift*-UVOT

The *Swift*-XRT observations were supplemented with UVOT exposures taken in the U, UVM2, and UVW2 bands (centered at 8.56×10^{14} Hz, 1.34×10^{15} Hz, and 1.48×10^{15} Hz, respectively; Poole et al. (2008)). The UVOT photometry is performed using the HEASOFT program *uvotsource*. The circular source region has a $5''$ radius and the background regions consist of several circles with radii between $10 - 15''$ of nearby empty sky. The results are reddening corrected using R(V)=3.32 and E(B-V)=0.14 (Schlegel et al., 1998). The Galactic extinction coefficients were applied according to Fitzpatrick (1999), with the largest source of error resulting from deredenning. A summary of the UVOT analysis results is given in Table 1.1.

1.2.5 Optical MDM

The region around RX J0648.7+1516 was observed in the optical B, V, and R bands with the 1.3-m McGraw-Hill Telescope of the MDM Observatory on four nights during 2010 April 1–5 (MJD 55287-55291). Exposure times ranged from 90 sec (R-band) to 120 sec (B-band). Each night, five sequences of exposures in B, V, and R were taken. The raw data were bias subtracted and flat-field corrected

Table 1.1: Analysis summary of the optical MDM (B, V, R) and *Swift*-UVOT (U, UVM2, UVW2) data.

Band	Date (MJD)	νF_ν (Jy Hz)	νF_ν Error (Jy Hz)
B	55287	7.47×10^{11}	3.4×10^{10}
B	55289	7.64×10^{11}	3.8×10^{10}
B	55290	5.75×10^{11}	2.7×10^{10}
B	55291	7.59×10^{11}	3.4×10^{10}
V	55287	5.77×10^{11}	3.5×10^{10}
V	55289	5.74×10^{11}	3.7×10^{10}
V	55290	2.92×10^{11}	1.6×10^{10}
V	55291	6.00×10^{11}	3.6×10^{10}
R	55287	5.99×10^{11}	4.2×10^{10}
R	55289	5.51×10^{11}	3.7×10^{10}
R	55290	2.03×10^{11}	1.5×10^{10}
R	55291	5.99×10^{11}	4.3×10^{10}
U	55288	4.542×10^{11}	6.8×10^{9}
U	55292	4.253×10^{11}	6.3×10^{9}
U	55300	3.856×10^{11}	6.1×10^{9}
U	55304	3.737×10^{11}	5.5×10^{9}
UVM2	55274	5.987×10^{11}	8.8×10^{9}
UVW2	55273	5.066×10^{11}	7.9×10^{9}

using standard routines in IRAF[4]. Aperture photometry is performed using the IRAF package DAOPHOT on the object as well as five comparison stars in the same field of view. Calibrated magnitudes of the comparison stars are taken from the NOMAD catalog[5], and the magnitudes of the object are determined using comparative photometry methods. For the construction of the SED points, the magnitudes are extinction corrected based on the Schlegel et al. (1998) dust map with values taken from NASA Extragalactic Database (NED)[6] : $A_B = 0.618$, $A_V = 0.475$, and $A_R = 0.383$. These data (summarized in Table 1.1) are used to constrain the modeling shown in this work, although the same conclusions result with the UVOT points as model constraint.

1.3 Spectroscopic Redshift Measurements

Two spectra were obtained during the nights of UT 2010 March 18 and 2010 November 6 (MJD 55245 and 55506, respectively) with the KAST double spectrograph on the Shane 3-m Telescope at UCO/Lick Observatory. During the first night, the instrument was configured with a 600/5000 grating and 1.5″ long slit, covering $4300 - 7100$ Å. A single 1800 second exposure was acquired. During the night of November 6, another 1800 second exposure was acquired with a 600/4310

[4] http://www.noao.edu/credit.html
[5] http://www.nofs.navy.mil/nomad.html
[6] http://nedwww.ipac.caltech.edu/

Table 1.2: Analysis summary of the VER J0648+152 Lick Observatory Kast spectrum from 2010 November 5 (MJD 55505). Table notes: [1] Blended with Mg I 5168.74 Mg I 5185.04 [2] Blended with Na I 5891.61 and Na I 5897.57.

Ions	Rest Wavelength (Å)	Centroid[8] (Å)	FWHM (Å)	Redshift[9] Absorbed	Observed E. W.[10] (Å)	Notes
Ca II (K)	3934.79	4639.07	20.7	0.1789	2.60 ±0.21	
Ca II (H)	3969.61	4678.26	16.4	0.1785	2.47±0.19	
G band	4305.61	5077.46	17.5	0.1792	1.70±0.18	
Mg I	5174.14	6102.32	22.1	0.1793	2.35±0.20	[1]
Na I	5894.13	6951.66	23.0	0.1794	2.48±0.15	[2]

grism, D55 dichroic, a 600/7500 grating and 2″ long slit, covering the interval $3500 - 8200$ Å. The data were reduced with the LowRedux pipeline[7] and flux calibrated using a spectro-photometric star. The flux calibration is uncertain due to non-photometric conditions. Inspection of the March spectrum reveals Ca H+K absorption lines at redshift $z = 0.179$. This redshift is confirmed in the second spectrum at higher signal-to-noise (S/N) (S/N ~ 20 in the blue and S/N ~ 50 in the red) where Ca H+K, G band, Mg I $\lambda\lambda\lambda$ $5168, 5174, 5184$ and Na I $\lambda\lambda\lambda$ $5891, 5894, 5897$ absorption lines with equivalent width < 5 Å are detected (see Figure 1.2 and Table 1.2 for details). No Ca H+K break is observed. These spectral features provide evidence for an early-type nature of the blazar host galaxy and allow for BL Lac classification, following Marcha et al. (1996) and Healey et al. (2007).

[7] `http://www.ucolick.org/~xavier/LowRedux/index.html`
[8] Based on Gaussian fit
[9] Measured from line centroid
[10] Error is only statistical

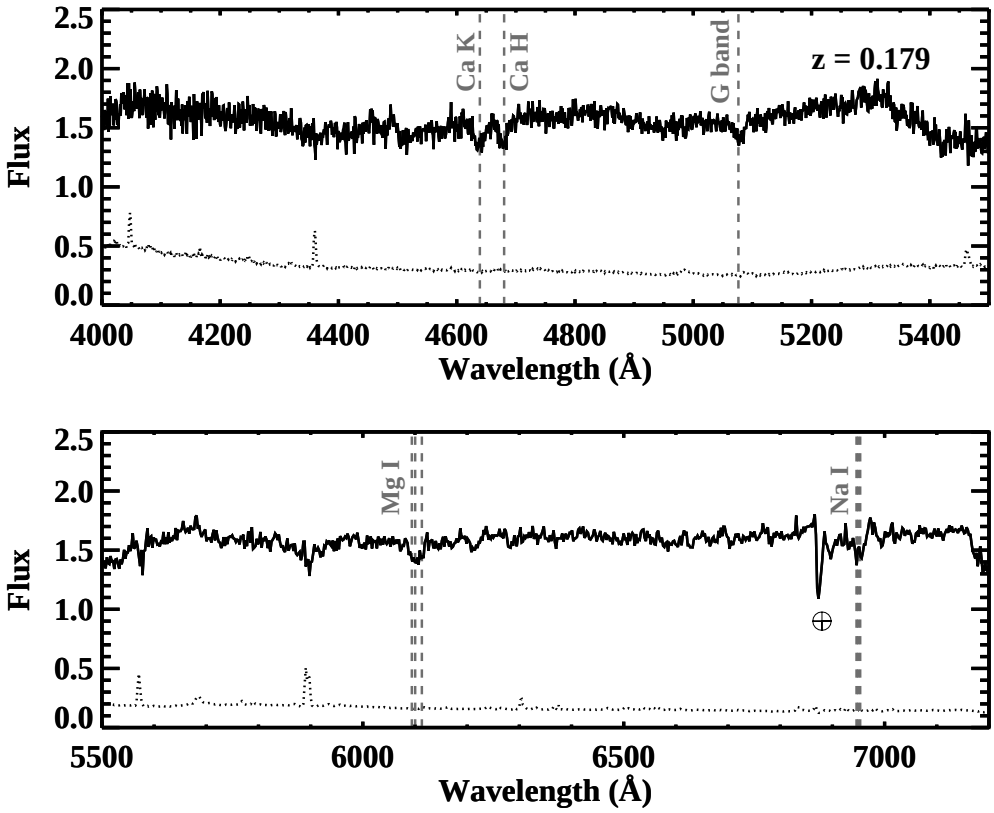

Figure 1.2: Spectrum of RX J0648.7+1516 showing the Ca H+K, G-band, Na I and Mg I spectral features indicating a redshift of $z = 0.179$. Since the G-band arises in stellar atmospheres, we interpret this as the redshift for the host galaxy and not an intervening absorber. The blazar was observed at Lick Observatory using the 3−m Shane Telescope on 6 November 2010.

1.4 Broadband SED Modeling

The contemporaneous multiwavelength data are matched with archival radio data from NED and are shown in Figure 1.3. Since the radio data are not contemporaneous they are shown only for reference. The synchrotron peak appears at a frequency greater than 10^{16} Hz, representing the first subclassification of RX J0648.7+1516, specifically as an HBL. These data are used to test steady-state leptonic and lepto-hadronic jet models for the broadband blazar emission. The absorption of VHE gamma rays by the extragalactic background light (EBL) is accounted for through application of the Gilmore et al. (2009) EBL model; the model of Finke et al. (2010) provides comparable results.

Leptonic models for blazar emission attribute the higher-energy peak in the SED to the inverse-Compton scattering of lower-energy photons off a population of non-thermal, relativistic electrons. These same electrons are responsible for the lower-energy synchrotron emission making up the first peak. The target photon field involved in the Compton upscattering can either be the synchrotron photons themselves, as in synchrotron self-Compton (SSC) models, or a photon field external to the jet in the case of external Compton (EC) models.

We use the equilibrium SSC model of Böttcher & Chiang (2002), as described in Acciari et al. (2009c). In this model, the emission originates from a spherical blob of relativistic electrons with radius R. This blob is moving down the jet with

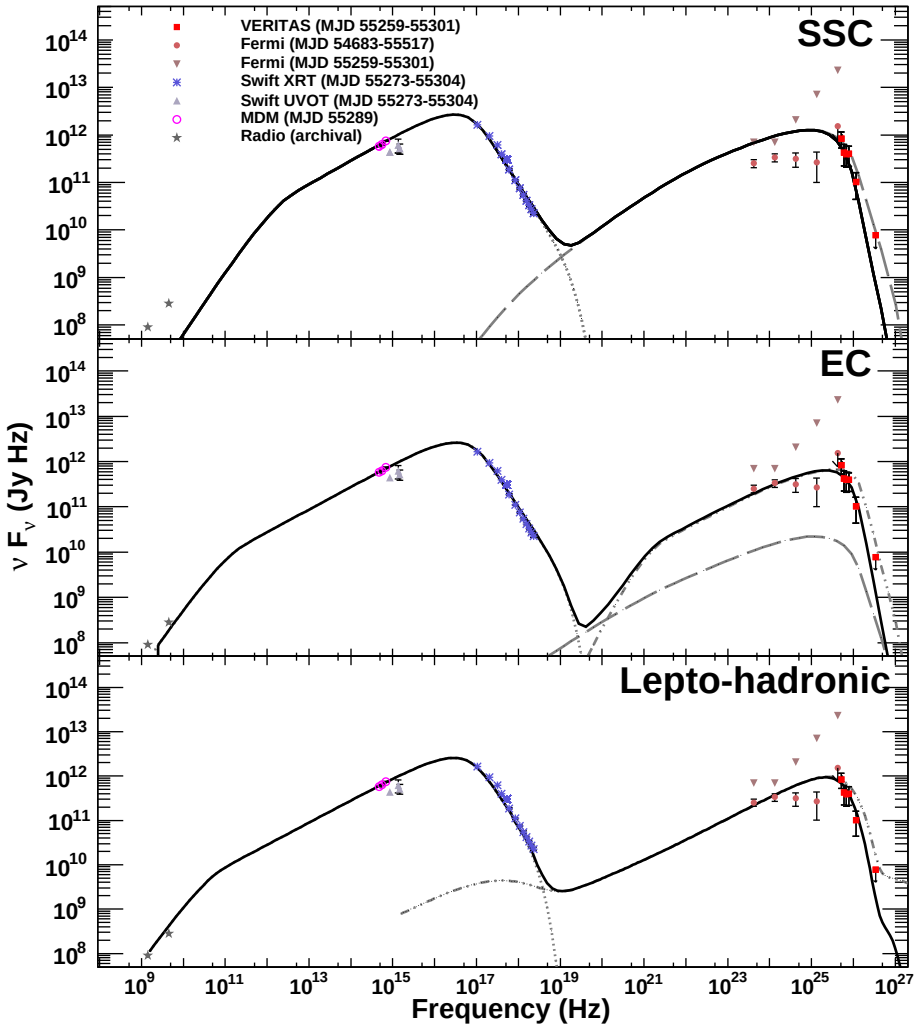

Figure 1.3: The SED models applied to the contemporaneous multiwavelength data of RX J0648.7+1516. *Fermi*-LAT data points are shown for 2.3 years of data along with upper limits extracted from data limited to the VERITAS observation period. The models shown here are constrained by the MDM points; modeling constrained by the UVOT data produces similar results. The top panel shows the synchrotron emission (dotted line), the self-Compton emission (dashed) and the EBL-corrected (Gilmore et al., 2009) total one-zone SSC model (solid). The middle panel shows the synchrotron emission (dotted line), the self-Compton emission (dashed line), the external-Compton (dash-dotted line) and the EBL-corrected total EC model (solid). The bottom panel shows the electron (and positron) synchrotron emission (dotted line), the proton synchrotron emission (dash-dotted) and the EBL-corrected total lepto-hadronic model (solid).

a Lorentz factor Γ, corresponding to a jet speed of $\beta_\Gamma c$. The jet is oriented such that the angle with respect to the line of sight is $\theta_{\rm obs}$, which results in a Doppler boosting with Doppler factor $D = (\Gamma[1 - \beta_\Gamma \cos\theta_{\rm obs}])^{-1}$. In order to minimize the number of free parameters, the modeling is completed with $\theta_{obs} = 1/\Gamma$, for which $\Gamma = D$.

Within the model, electrons are injected with a power-law distribution at a rate $Q(\gamma) = Q_0 \gamma^{-q}$ between the low- and high-energy cut-offs, $\gamma_{1,2}$. The electron spectral index of $q = 4.8$ required for the models applied in this work might be the result of acceleration in an oblique shock. While standard shock acceleration in relativistic, parallel shocks is known to produce a canonical spectral index of $\sim$2.2, oblique magnetic-field configurations reduce the acceleration efficiency and lead to much steeper spectral indices (Meli & Quenby, 2003; Sironi & Spitkovsky, 2011). The radiation mechanisms considered lead to equilibrium between the particle injection, radiative cooling and particle escape. The particle escape is characterized with an efficiency factor η, such that the escape timescale $t_{\rm esc} = \eta\, R/c$, with $\eta = 100$ for this work. This results in a particle distribution streaming along the jet with a power L_e. Synchrotron emission results from the presence of a tangled magnetic field B, with a Poynting flux luminosity of L_B. The parameters L_e and L_B allow the calculation of the equipartition parameter $\epsilon_{Be} \equiv L_B/L_e$.

The top panel in Figure 1.3 shows the SSC model for RX J0648.7+1516, with

parameters summarized in Table 1.3. The model is marginally in agreement with the data only through use of parameters well below equipartition. The *Fermi*-LAT contemporaneous 95% confidence level upper limits in the energy ranges 1-3 GeV and 3-10 GeV are just above and below the one-zone SSC model predictions. Additionally, these SSC model predictions are above the 2.3 year *Fermi*-LAT spectrum by more than a factor of 2, although this spectrum is not contemporaneous with the other data. Variation of the model parameters within physically reasonable values does not provide better agreement between model and data. Generally, HBLs are well characterized by one-zone SSC models and hence these observations might suggest the existence of one or more additional emission mechanisms that contribute to the higher-energy peak.

An external-Compton model is also used to describe the data. The EC model is a leptonic one-zone jet model with two additional parameters beyond the SSC parameters, the thermal blackbody temperature T_{EC} and radiation energy density u_{EC} of the external photon field, which is assumed to be isotropic and stationary in the blazar rest frame. The EC model provides a better representation of the SED, as can be seen in the middle panel of Figure 1.3, with the parameters listed in Table 1.3.

A lepto-hadronic model is also applied to the data. Within this model, ultrarelativistic protons are the main source of the high-energy emission through proton

synchrotron radiation and pion production. The resulting spectra of the pion decay products are evaluated with the templates of Kelner & Aharonian (2008). Additionally, a semi-analytical description is used to account for electromagnetic cascades initiated by the internal $\gamma\gamma$ absorption of multi-TeV photons by both the π^0 decay photons and the synchrotron emission of ultrarelativistic leptons, as explained in Böttcher (2010). Similar to the particle populations in the leptonic models described above, this lepto-hadronic model assumes a power-law distribution of relativistic protons, $n(\gamma) \propto \gamma^{-q}$ between a low- and high-energy cut-off, $E_{\rm p}^{\rm min,max}$. This population of relativistic protons is propagating along the blazar jet and has a total kinetic luminosity of L_p. The lepto-hadronic modeling results are above ϵ_{Bp} equipartition and are shown in the bottom panel of Figure 1.3 with parameters (including energy partition fractions $\epsilon_{Bp} \equiv L_B/L_p$ and $\epsilon_{ep} \equiv L_e/L_p$) summarized in Table 1.3.

In conclusion, multiwavelength followup of the VERITAS detection of 1FGL J0648.7+1516 has solidified its association with RX J0648.7+1516, which is identified as a BL Lac object of the HBL subclass. Other contemporaneous SEDs of VHE-detected HBLs can be well described by one-zone SSC models close to equipartition, while for RX J0648.7+1516 this model provides a poor representation with parameters below equipartition. The addition of an external photon field for Compton up-scattering in the leptonic paradigm provides a better

Table 1.3: SED Modeling Parameters: Summary of the parameters describing the emission-zone properties for the SSC, EC and lepto-hadronic models. See text for parameter descriptions.

Parameter	SSC	External Compton	Lepto-Hadronic
L_e [erg s^{-1}]	7.5×10^{43}	4.9×10^{41}	4.9×10^{41}
γ_1	6.7×10^4	8.2×10^4	9×10^3
γ_2	10^6	10^6	5×10^4
q	4.8	4.8	4.8
B [G]	0.14	0.1	10
$\Gamma = D$	20	20	15
T_{EC} [K]	—	10^3	—
u_{EC} [erg cm^{-3}]	—	7.0×10^{-8}	—
L_p [erg s^{-1}]	—	—	4.9×10^{41}
$E_{\rm p}^{\rm min}$ [GeV]	—	—	10^3
$E_{\rm p}^{\rm max}$ [GeV]	—	—	1.5×10^{10}
q_p	—	—	2.0
ϵ_{Be}	0.16	41	1.7×10^4
ϵ_{Bp}	—	—	4.2
ϵ_{ep}	—	—	2.5×10^{-4}
$t_{\rm var}^{\rm min}$ [hr]	1.1	10.9	7.2

representation of the gamma-ray (*Fermi* and VERITAS) data. Alternatively, a lepto-hadronic model is successful in characterizing the higher-energy peak of the SED with synchrotron emission from protons. Both of these latter models require super-equipartition conditions.

Chapter 2

VERITAS Observations of Six Bright, Hard-Spectrum *Fermi*-LAT Blazars

This work has been published in the Astrophysical Journal (*Aliu, E. et al. 2012, ApJ, 759, 102*). The corresponding author of the work is Amy Furniss. No content was modified aside from necessary formatting. The full author list of this work can be found in Appendix B.

Abstract

We report on VERITAS very-high-energy (VHE; E≥100 GeV) observations of six blazars selected from the Fermi Large Area Telescope First Source Catalog (1FGL). The gamma-ray emission from 1FGL sources was extrapolated up to the VHE band, taking gamma-ray absorption by the extragalactic background light into account. This allowed the selection of six bright, hard-spectrum blazars that were good candidate TeV emitters. Spectroscopic redshift measurements were attempted with the Keck Telescope for the targets without Sloan Digital Sky Survey (SDSS) spectroscopic data. No VHE emission is detected during the observations of the six sources described here. Corresponding TeV upper limits are presented, along with contemporaneous Fermi observations and non-concurrent Swift UVOT and XRT data. The blazar broadband spectral energy distributions (SEDs) are assembled and modeled with a single-zone synchrotron self-Compton model. The SED built for each of the six blazars show a synchrotron peak bordering between the intermediate- and high-spectrum-peak classifications, with four of the six resulting in particle-dominated emission regions.

2.1 Introduction

Blazars are active galactic nuclei (AGN) with a relativistic jet pointed close to the Earth line of sight. AGN are thought to be powered by accretion onto a supermassive black hole ($\sim 10^9 M_\odot$) at the center of the host galaxy and are characterized by a double-peaked spectral energy distribution (SED) in the νF_ν representation.

The lower energy peak of the broadband SED is attributed to synchrotron emission of highly relativistic electrons and positrons in the presence of a tangled magnetic field. In leptonic models, the higher energy peak is produced via the inverse-Compton (IC) up-scattering by the relativistic leptons of the synchrotron photons (synchrotron self-Compton, SSC) or a photon field external to the jet (external Compton, EC). More details regarding leptonic non-thermal emission of blazars can be found in Dermer et al. (1992); Maraschi et al. (1992); Sikora et al. (1994) and the references therein. Alternative models associate the higher-energy peak to interaction of relativistic protons with an ambient photon field (Aharonian et al., 2002; Bednarek, 1993; Dar et al., 1997; Mannheim, 2000; Mücke & Protheroe, 2000; Pohl & Schlickeiser, 2000), or a hybrid population comprised of both leptons and hadrons (Böttcher, 2007).

The blazar population is divided into two subclasses: flat spectrum radio quasars (FSRQs) and BL Lacs. FSRQs are, to first order, more distant, more lu-

minous, and have stronger emission lines than BL Lacs. Historically, BL Lacs have been sub-classified based on their radio and X-ray flux ratios as low-, intermediate- or high-frequency-peaked BL Lac objects (LBL, IBL and HBLs, respectively) as described in Padovani & Giommi (1995) and Bondi et al. (2001). More recently, a classification based on the location of the synchrotron peak in frequency space (ν_{synch}) has been proposed by Abdo et al. (2010c), with low-spectrum-peaked (LSP) BL Lac objects having ν_{synch} below 10^{14} Hz, intermediate-spectrum-peaked (ISP) BL Lac objects peaking between 10^{14} and 10^{15} Hz and high-spectrum-peaked (HSP) BL Lac objects showing a peak above 10^{15} Hz. HSP BL Lacs are the most common extragalactic object to be detected at very-high-energies (VHE; $E \geq 100$ GeV), comprising 33 of 41 VHE BL Lac objects detected as of June 2012. There have also been 4 ISPs (Acciari et al., 2009a,c, 2010; Ong, 2010a) and 4 LSPs (Mazin et al., 2009; Mariotti, 2011a; Hoffman, 2010; Albert et al., 2007) detected since the advent of VHE gamma-ray astronomy in the late 1960s. In addition, three FSRQs, three radio galaxies, and two starburst galaxies complete the catalog of associated extragalactic objects (Horan & Wakely, 2008)[1].

The potential scientific impact of increasing the catalog of VHE emitting extragalactic objects is substantial. A significant fraction of the power released from these objects is within the VHE band. This makes the measurement of VHE blazar spectra an important component of the overall understanding of these ob-

[1] `http://tevcat.uchicago.edu/`

jects. With a better sample of well-measured VHE blazar spectra available for study, a population-based investigation of gamma-ray production in these objects through broadband SED modeling will be possible, providing means to answer the long-standing question of whether VHE gamma-ray emission results from leptonic or hadronic processes in AGN jets. We can also apply the model-inferred properties of these new discoveries to understanding how the gamma-ray production may differ among blazar subclasses, exploring the apparent blazar sequence and evolution of the AGN (Fossati et al., 1998; Ghisellini & Tavecchio, 2008; Meyer et al., 2011).

VHE blazars can also be used to constrain the optical to near-infrared extragalactic background light (EBL) density and evolution, as well as the nature of cosmic rays. The EBL encodes the integrated history of structure formation and the evolution of stars and galaxies in the Universe. Understanding these characteristics requires detailed theoretical modeling of all the processes that contribute, e.g. structure formation and stellar evolution (Dominguez et al., 2011; Gilmore et al., 2009; Primack et al., 2005; Finke et al., 2010; Franceschini et al., 2008; Hauser & Dwek, 2001; Stecker et al., 2006). According to some cosmic ray models, e.g. Essey & Warren (2012), interactions of cosmic rays along the blazar line-of-sight can produce relatively hard VHE gamma-ray spectra as compared with the high-energy gamma-ray spectra, depending on the distance to the blazar.

The current catalog of extragalactic VHE objects largely contains relatively nearby AGN; only three have a confirmed redshift above $z = 0.3$. The highest redshift blazar detected at VHE thus far is the FSRQ 3C 279, at a redshift of 0.536 (Albert et al., 2008b). The proximity of these VHE blazars is partly a result of gamma-ray absorption by the EBL. VHE gamma rays that propagate through the intergalactic medium are absorbed by low energy EBL photons via pair production, $\gamma + \gamma \rightarrow e^+ + e^-$ (Nikishov, 1962; Gould & Shréder, 1967; Stecker et al., 1992). The absorption process deforms the VHE gamma-ray spectra emitted by extragalactic objects in a redshift-dependent manner and can be translated to upper limits on the local density of the far-infrared EBL (Stecker et al., 1993; Dwek & Krennrich, 2005; Aharonian et al., 2006; Primack et al., 2011; Orr et al., 2011).

The search for new VHE blazars is complicated by the fact that many of these objects do not yet have known redshifts. BL Lac objects, by definition, display very weak or no optical emission or absorption lines used for spectroscopic redshift measurements. Due to the interaction of VHE photons with the EBL, non-detection of blazars with no redshift information can be either attributed to the object being too distant or having an intrinsically low luminosity in the VHE band. This makes VHE discovery observations of blazars with no measured redshift a risky venture, although it has proven successful in the past, as in the

discoveries of VHE emission from 3C 66A, PKS 1424+240, and RX J0648.7+1516 (Acciari et al., 2009a, 2010; Aliu et al., 2011b).

The small field of view of imaging atmospheric Cherenkov telescopes (IACTs, $\leq 5.0°$) makes new source discovery from a large-scale sky survey difficult and therefore the hunt for VHE emitting objects has historically involved targeted observations of source candidates selected from surveys at lower frequencies, such as the selection of hard X-ray candidates presented in Costamante & Ghisellini (2002). In this way, VHE blazar candidate selection has relied on experiments such as EGRET onboard the Compton Gamma Ray Observatory (Thompson et al., 1993), *Swift* (Gehrels et al., 2004) and ROSAT (Turriziani et al., 2007). The launch of *Fermi* in June 2008 has enhanced VHE blazar discovery programs, leading to new blazar discoveries including RBS 0413, RX J0648.7+1516, 1ES 0033+595 and 1RXS J101015.9-311909 (Aliu et al., 2012a, 2011b; Mariotti, 2011b; Abramowski et al., 2012).

The *Fermi* Large Area Telescope (LAT) observes the entire sky in the energy range from 20 MeV to > 300 GeV every three hours and has better sensitivity than its predecessor EGRET. Within the first 11 months of operation, the 1FGL catalog reported the detection of 1451 sources at a significance greater than 5σ (Abdo et al., 2010a). A majority of these sources are, or are expected to be, associated with AGN (Abdo et al., 2010b). It is known that a large majority of

these blazars has not yet been detected by VHE instruments, as can be seen by the current TeV catalog, which only contains 51 associated extragalactic objects. However, the proximity of the *Fermi*-LAT energy band to that of the IACTs makes the 1FGL catalog a good place to search for candidate VHE blazars. We report on VERITAS observations above 100 GeV of six candidate blazars. For the first time, a multiwavelength description of their SED including radio, UV, X-ray and gamma-ray frequencies is assembled and modeled using a SSC model.

2.2 Target Selection

The energy coverage of IACTs overlaps with that of *Fermi*-LAT above 100 GeV and extends to tens of TeV. Sources that are most likely to be detected by both *Fermi*-LAT and IACTs have high fluxes and hard photon indices in the *Fermi*-LAT energy band. A selection process was established to identify the best VHE candidates within the first *Fermi*-LAT catalog. Sources at low Galactic latitude ($|b| < 10^{\circ}$) were excluded, with the intent of removing the majority of Galactic sources from the selection. Additionally, sources with low integrated flux above 100 MeV ($F_{100MeV} < 2 \times 10^{-9}$ph cm^{-2}s^{-1}), with soft photon indices ($\Gamma > 2.0$), or with a low number of associated photons ($N_{pred} < 20$), were excluded from the selection. Just over 200 sources passed this initial set of cuts.

The remaining sources were re-analyzed using the same data set as that used

for the 1FGL catalog to search for the presence of curvature in their spectra. A log-parabola parameterization for the spectra was chosen as the alternative to the power-law model (null hypothesis). In addition, the data were analyzed only using data above 1 GeV to confirm that the results from the power-law fit found for the entire *Fermi*-LAT energy band agreed well with the power-law fit above 1 GeV. Sources showing significant spectral curvature or softening of the spectrum above 1 GeV with an improvement in likelihood value corresponding to 3σ were excluded from the final selection as these sources are not expected to exhibit bright TeV flux levels. For sources with spectra best fit by a power law that also matched the power-law fit above 1 GeV, the *Fermi*-LAT spectrum was extrapolated up to the VHE regime (150 GeV - 1 TeV). When a reliable redshift measurement was available, the EBL model of Franceschini et al. (2008) was used to estimate the extrapolated VHE gamma-ray flux. Otherwise an assumed redshift of z = 0.2 was used, a conservative value considering that most known TeV sources have redshifts less than $z = 0.2$. Finally, the sources were ranked based on their extrapolated flux in the VHE regime. Six VHE candidates, all BL Lac objects, were selected for observations with the VERITAS telescope between September 2009 and June 2010 for 10 hours each, corresponding to the VERITAS 3% Crab flux sensitivity exposure timescale.

Table 2.1 shows the VHE extrapolated integral flux from the 1FGL catalog

power-law fits used for selection of the six candidate VHE emitting blazars. These relatively high integral flux values above 150 GeV, shown in percentages of the Crab Nebula flux[2], are shown in comparison to the updated power-law fits from 29 months of *Fermi*-LAT data for the steady sources, and data from the VERITAS coincidental window for variable sources. The analysis of the extended *Fermi*-LAT dataset (2008 August 4 to 2011 January 4) is detailed in section 4.2. These updated extrapolations show much lower expected integral flux values for each of the six candidates, reflecting the fact that as more LAT data were collected, better high-energy statistics showed the candidates to be softer and/or dimmer than found with the elevent month data set used in the 1FGL. Additionally, we compare these extrapolated values to the upper limits derived from the VERITAS observations, where the analysis leading to these upper limits is detailed in Section 4.1.

2.3 The Targets

RGB J0136+391 (1FGL J0136.5+3905) was discovered in the third Bologna sky survey of 408 MHz radio objects (Ficarra et al., 1985). It was later detected as

[2]Flux calculated according to the curved power law presented in Albert et al. (2008a)

[3]Taken from Abdo et al. (2010a). Index and flux extrapolated without error for target selection.

[4]Computed with power-law fit from 29 months of data for steady sources and VERITAS coincident time window for variable sources (RGB J0316+090 and RGB J1058+564).

Table 2.1: Summary of the high-energy *Fermi*-LAT power-law extrapolation beyond 150 GeV resulting from power-law fits from the 11 months of data used to select the candidates as well as the extrapolation based on the extended data set spanning 29 months. These extrapolated flux values factor in the gamma-ray absorption resulting from interaction with the EBL and are reported in % Crab Nebula flux units above the same energy threshold in order to allow direct comparison with the upper limits derived from the VERITAS observations.

Counterpart Name	Original z Used for Selection	1FGL Index	1FGL Integral Flux[3] $\geq$300 MeV [$\times 10^{-9}$ ph cm^{-2}s^{-1}]	1FGL Extrapolated Flux $\geq$ 150 GeV [% Crab]	Updated z Lower Limit	Updated Extrapolated Flux[4] [%Crab]	VERITAS UL [%Crab]
RGB J0136+391	0.2	1.73	9.5	4.1	0.2	3.5	1.7
RGB J0316+090	0.2	1.72	19.6	8.1	0.2	0.3	2.0
RGB J0909+231	0.2	1.46	6.6	12.1	≥ 0.4305	0.5	1.5
RGB J1058+564	0.143	1.97	15.7	1.5	0.143	1.1	1.1
RGB J1243+364	0.2	1.74	5.8	2.2	≥ 0.485	0.8	3.1
RX J1436.9+5639	0.15	1.45	3.6	11.7	0.15	0.7	2.4

a X-ray bright active galaxy in the Northern ROSAT all-sky survey (Brinkmann et al., 1997), and identified spectroscopically as a BL Lac object, with an IBL sub-classification from Laurent-Muehleisen et al. (1998) and Laurent-Muehleisen et al. (1999), respectively. Based on the optical and X-ray spectral properties, this blazar was proposed as a VHE candidate blazar by Costamante & Ghisellini (2002), under the assumption that the redshift was less than 0.2. Bright gamma-ray emission above 1 GeV was detected from this source by *Fermi* after three months of operation. Only an upper limit below 1 GeV was reported (Abdo et al., 2009b). This blazar also showed constant emission in the first eleven months of LAT operation (Abdo et al., 2010a). This blazar remains without a known redshift, with no previous spectroscopic redshift measurements found in the available literature. We attempted a spectroscopic redshift measurement on 2009 September 17 (MJD 55091) using the Keck Low Resolution Imaging Spectrometer (LRIS) instrument, but measured only a featureless power-law spectrum that is characteristic of BL Lac objects (see Figure 2.1 upper-left panel). Detailed spectroscopic analysis of this data can be found in Kaplan et al. (2012).

RGB J0316+090 (1FGL J0316.1+0904) was first detected by the NRAO Green Bank 91 meter radio telescope (Becker et al., 1991). It was later optically identified as a BL Lac object (Fischer et al., 1998) and sub-classified as an IBL by Laurent-Muehleisen et al. (1999). No spectroscopic redshift measurements

had been made prior to this work. We attempted a spectroscopic redshift measurement on 2011 March 5 using the Keck Echelette Spectrograph and Imager (ESI) instrument, resulting in a featureless power-law spectrum except for two unidentified absorption features (see Figure 2.1 upper-right panel). The detailed spectroscopic analysis of the Keck ESI data can be found in Kaplan et al. (2012).

RGB J0909+231 (1FGL J0909.2+2310) was first detected by the NRAO Green Bank radio telescope (Becker et al., 1991) and was later classified as a radio-loud active galaxy (Brinkmann et al., 1997). The BL Lac optical counterpart was identified nearly a decade later (Mickaelian et al., 2006). The redshift reported by the NASA Extragalactic Database (NED)[5] could not be found within the corresponding reference ($z = 0.231$, Brinkmann et al. (2000)) and was therefore taken as unknown. Inspection of publicly available Sloan Digital Sky Survey (SDSS) data revealed two Mg II absorption lines in the otherwise featureless optical spectrum. Assuming that these lines could be intrinsic, or due to the absorption by an intervening cloud, a lower limit on the redshift of $z \geq 0.43$ is derived (see Figure 2.1 middle-left panel). This is the only source out of the six selected which has a neighboring *Fermi*-LAT detected blazar within the VERITAS 3° field of view. 2FGL J0910.9+2246, associated with TXS 0907+230, is located 0.61° away from RGB J0909+231. The high redshift blazar TXS 0907+230 ($z = 2.66$ according to Healey et al. (2007)) shows no signal in the 10-100 GeV band, with an upper limit

[5] `http://nedwww.ipac.caltech.edu/`

of 9.6×10^{-11}photons cm^{-2}s^{-1} reported in the 2FGL catalog (Nolan et al., 2012). An exclusion region of radius 0.3° centered on the blazar was nevertheless used in the VERITAS analysis to avoid possible contamination.

RGB J1058+564 (1FGL J1058.6+5628) was first detected in the 6C radio survey (Hales et al., 1990). It was identified as a BL Lac object during the association of the ROSAT all-sky survey with the Hamburg Quasar Survey (Nass et al., 1996). Bondi et al. (2001) classified the object as an IBL based on the optical and X-ray characteristics. This blazar was detected within the first three months of *Fermi*-LAT operation (Abdo et al., 2009b) with a broadband SED shown in Abdo et al. (2010c) which does not include any VHE information. The blazar also shows a high level of flux variability (probability of variability: 79%) in the high-energy gamma-ray band, as shown in Abdo et al. (2010a) and is the only one out of the six targets in this paper that has a redshift measurement. The absorption lines corresponding to the redshift 0.143 can be seen in the SDSS spectrum shown in Figure 2.1 (middle-right panel).

RGB J1243+364 (1FGL J1243.1+3627) was first reported in the B2 catalog of radio sources (Colla et al., 1973). This target was also determined to be a radio-loud active galaxy by ROSAT (Brinkmann et al., 1997), and specifically classified as a BL Lac in Appenzeller et al. (1998). NED cited the SDSS data for a spectroscopic redshift of $z = 1.065$. Inspection of this publicly available

SDSS data revealed no lines suggesting this redshift but instead revealed Mg II absorption lines that translate to a lower limit of $z \geq 0.485$ (see Figure 2.1 lower-left panel). A recent photometric redshift of z= $0.5^{+0.14}_{-0.12}$ from Meisner & Romani (2010) is in agreement with the SDSS lower limit.

RX J1436.9+5639 (1FGL J1437.0+5640) was detected in the ROSAT all-sky survey and identified as a BL Lac object by Nass et al. (1996). This HBL, as classified by Nieppola et al. (2006) based on the frequency of the synchrotron peak, remains without a redshift, although the redshift of the galaxy cluster within the same region of the sky is known to be z= 0.15 (Bauer et al., 2000). Inspection of the publicly available SDSS data shows a featureless spectrum, shown in Figure 2.1.

2.4 Multiwavelength Observations and Analysis

2.4.1 VERITAS

The VERITAS observatory is an array of four 12-meter diameter IACTs, located in southern Arizona. VERITAS is sensitive to photons between 100 GeV and several tens of TeV with an energy resolution of better than 20%. The instrument has a 5σ point source sensitivity of 1% of the Crab Nebula flux in less

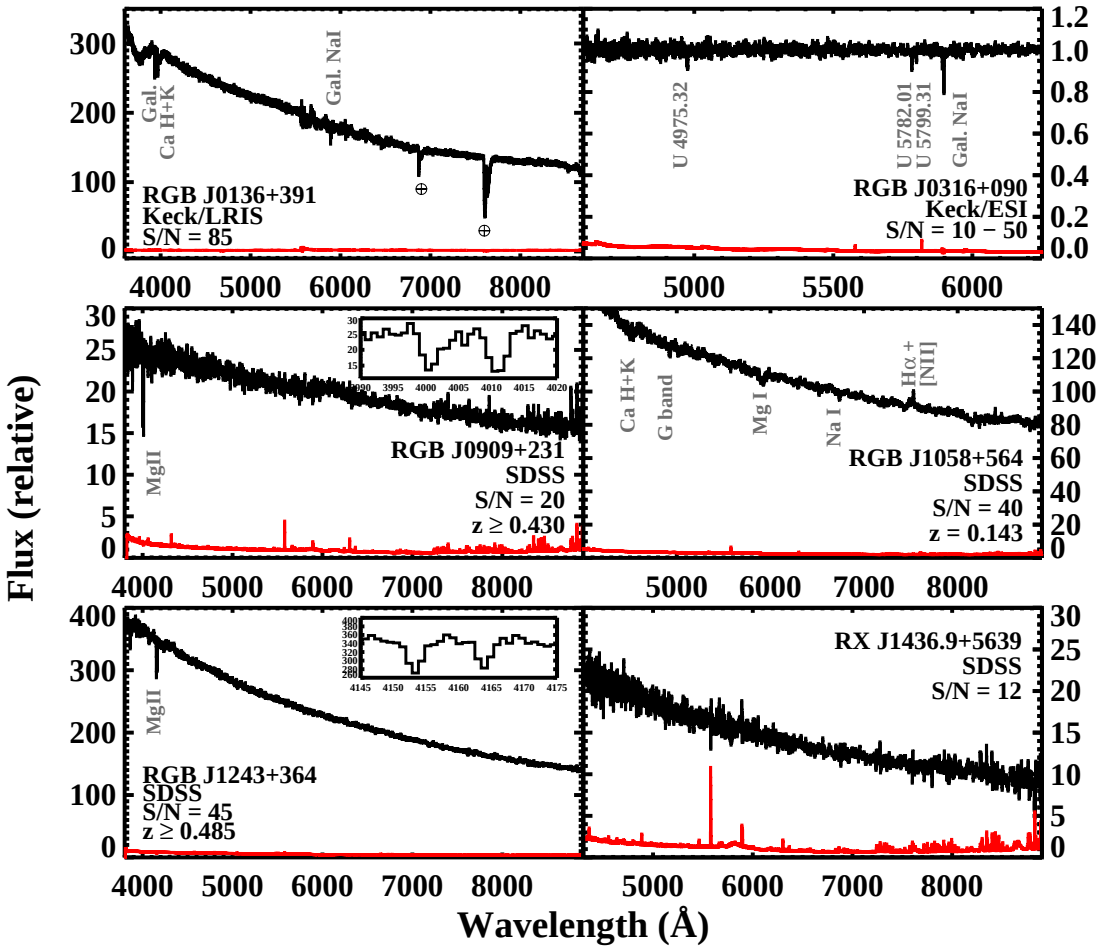

Figure 2.1: Optical spectra for the six BL Lacs selected from the 1FGL catalog and observed with VERITAS. The black shows the object spectrum, while the red shows the instrumental noise. Only one BL Lac had a confirmed redshift upon selection (RGB J1058+564, z=0.143), confirmed with the SDSS spectrum shown in the middle-right panel. Redshift lower limits for RGB J0909+231 ($z \geq 0.4305$; middle left) and RGB J1243+364 ($z \geq 0.485$; lower left) are found from Mg II absorption lines in the SDSS spectra. A featureless SDSS spectrum is found for RX J1436.9+5639. A redshift measurement attempt for RGB J0136+391 using the Keck LRIS instrument shows a featureless power-law spectrum (upper left). The normalized ESI spectrum of RGB J0316+090 exhibits three unidentified absorption features (upper right). The spectral analysis of the Keck LRIS and ESI spectra are detailed in Kaplan et al. (2012).

than 30 hours with an angular resolution of less than 0.1° for a Crab-like source with a spectral index of 2.5. See Weekes et al. (2002) and Holder et al. (2006) for a detailed overview of the instrument.

The VERITAS observations of the six VHE candidate blazars were completed between September 2009 and June 2010 (MJD 55122–55383). These observations were taken in *wobble* mode, with an offset of 0.5° from the source position in each of four cardinal directions to allow simultaneous background measurement, as explained in Fomin et al. (1994) and Berge et al. (2007). The radio location of the counterparts as specified by NED were used for source position.

Air shower events initiated by gamma and cosmic-rays are reconstructed following the procedure outlined in Acciari et al. (2008). The recorded shower images are parameterized by their principal moments, giving an efficient method for suppression of the far more abundant cosmic-ray background. Any events with a total charge less than 50 photoelectrons are removed from the analysis. A set of cuts is then applied to the parameters in order to reject background events (see details of this method in Krawczynski et al. (2006)). These parameters reject cosmic-ray like events having the *mean scaled width* and *length* of the event camera image smaller than 1.1 or 1.4, respectively. Additionally, the reconstructed altitude of the maximum Cherenkov emission is required to be higher than 8 km above ground level. Gamma-ray like events are extracted from a signal region

with a radius of 0.14°, centered at the coordinates of the candidate source.

The quality-selected livetime collected for each target ranges from 4.4 to 14.2 hours and results in no detections, with significances ranging from -1.1 to 0.9σ, calculated with Equation (17) of Li & Ma (1983). The VERITAS observations and analysis results are detailed in Table 2.2. Integral upper limits at 99% confidence level are calculated using the Rolke et al. (2005) method, assuming a photon index of $\Gamma = 3.0$ for the differential power-law spectrum $dN/dE = N(E/E_o)^{-\Gamma}$. This index was assumed as a moderately softened index as compared to the *Fermi*-LAT index range ($1.74-2.9$), expected due to absorption by the EBL and possible intrinsic turnover. Additionally, this index value is representative of a typical TeV blazar. Without detection, the real index in the VHE band remains unknown and any integral upper limit derived is dependent on the index assumed. The differential upper limit is quoted at the decorrelation energy, the energy where the calculated flux has minimal dependence on the index. Changing the spectral index by ± 0.5 changes the differential upper limits by less than 10%.

The results are independently reproduced with two different analysis packages, as described in Cogan (2008) and Daniel (2008). The upper limits range from 1 to 3% of the integral Crab Nebula flux above the threshold energy. The energy threshold for each observation is defined as the energy at which the differential rate of reconstructed gamma rays from the postulated source reaches its maximum

and is accurate to within the 20% energy resolution of the instrument, a value that is dependent on the observation zenith angle and sky brightness.

2.4.2 *Fermi* LAT

The *Fermi*-LAT is a pair-conversion telescope sensitive from 20 MeV to > 300 GeV, which operates in survey mode. Further details about the characteristics and performance of the LAT Instrument on the *Fermi* Gamma-ray Space Telescope can be found in Atwood et al. (2009). Presented here is the analysis of the *Fermi* LAT data for the six candidates described in Section 3. Although the targets were selected based on only 11 months of data, more data was available after the completion of VERITAS observations and this larger data set is used for the modeling. More specifically, the LAT data from the time period of 2008 August 4 to 2011 January 4 (MJD 54682.7-55565.0) were used for the modeling analysis. Light curves for each source are shown in Figure 2.2. Except for variable sources, the analysis procedure was identical for each of the sources and proceeded as follows.

[6]Normalization factor between size of the ON and OFF regions.

[7]Defined as the energy at which the differential rate of reconstructed gamma rays from the postulated source reaches its maximum, accurate to within the 20% energy resolution of VERITAS.

[8]The energy at which the upper limit is minimally dependent on the index assumed for the source.

[9]Redshift of spatially coincident galactic cluster, taken from Bauer et al. (2000).

Table 2.2: Summary of VERITAS observations and analysis results. The significances are computed from counts extracted from source and background regions (ON and OFF, respectively) according to Equation 17 of Li & Ma (1983). The VHE 99% confidence level integral upper limits (ULs) are used for the modeling and are derived with an assumed photon index of 3.0. The percentage Crab Nebula flux values are given above the corresponding energy thresholds for each observation.

Counterpart Name	z	VERITAS Livetime [hr]	Observation Window [MJD]	ON Events	OFF Events	α[6]	Significance σ	Threshold[7] Energy [GeV]	Integral UL Above Threshold [$\times 10^{-8}$ph m^{-2}s^{-1}] (% Crab)	Decorrelation[8] Energy [GeV]	Differential UL at Decorrelation Energy [$\times 10^{-7}$ m^{-2}s^{-1}TeV^{-1}]
RGB J0136+391	–	9.9	55122-55129	1422	11224	0.1277	-0.2	165	4.9 (1.7%)	260	1.6
RGB J0316+090	–	4.4	55126-55133	698	5560	0.1282	-0.5	165	5.7 (2.0%)	275	1.5
RGB J0909+231	$\geq$0.4305	14.2	55150-55204	2141	14310	0.1499	-0.1	165	4.3 (1.5%)	260	1.3
RGB J1058+564	0.143	9.8	55160-55185	1415	10405	0.1417	-1.1	220	2.1 (1.1%)	350	4.7
RGB J1243+364	$\geq$0.485	11.5	55189-55291	1617	11133	0.1389	0.9	150	9.9 (3.1%)	250	2.9
RX J1436.9+5639	0.15[9]	13.0	55275-55383	1563	12314	0.125	0.6	240	4.1 (2.4%)	375	8.9

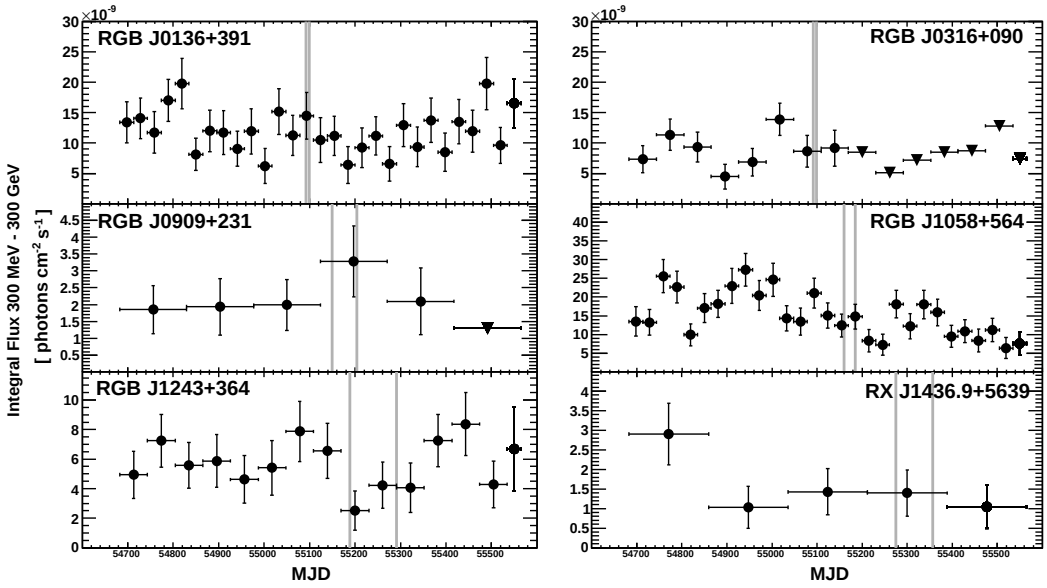

Figure 2.2: *Fermi*-LAT light curves, with units of 10^{-9} ph cm^{-2}s^{-1}, are shown for the six candidate VHE-emitting BL Lacs for 29 months of LAT data (MJD 54682-55565; 2008 August 4-2011 January 4). The beginning and end of the VERITAS observations are denoted by vertical grey lines in each panel. The short VERITAS observation periods for RGB J0136+364 and RGB J0316+090 can be seen, representing only 7 days each. Upper limits at 95% confidence level are shown for bins resulting in TS of less than 9, denoted by downward pointing black triangles. Only RGB J0316+090 and RGB J1058+564 show any significant variability. For these two sources, LAT data only for the time periods within the window of VERITAS observations are used to constrain the modeling.

For each candidate, events were extracted from a region of interest (ROI) of 10° radius centered on the target coordinates. Events from the "diffuse class" with zenith angle $< 100°$ and energy between 300 MeV and 300 GeV were selected. Only data taken during periods when the rocking angle of the satellite was $< 52°$ were used to reduce contamination from the Earth limb gamma rays, which are produced by cosmic rays interacting with the upper atmosphere. The significance and spectral parameters were calculated using an unbinned maximum-likelihood method implemented in the LAT Science Tool `gtlike`[10] (Cash, 1979; Mattox et al., 1996). A background model was constructed including nearby gamma-ray sources and diffuse emission. All sources within 12° of the central source in the second *Fermi*-LAT catalog (2FGL, Nolan et al. (2012)) were included in the model. The spectra of known pulsars were modeled by a power laws with exponential cutoffs. As in the 2FGL catalog, a log-parabola function was used for sources with significant spectral curvature. Otherwise, spectra were described as a power law. The spectral parameters of the sources in the ROI were left free during the fitting procedure. Sources outside the ROI, but within the 12° range had their spectral parameters fixed to the 2FGL catalog values. The Galactic diffuse emission and an isotropic component, which is the sum of the extragalactic diffuse

[10] `ScienceTools v9r20p0` with the post-launch instrument response function (IRF) `P6_V11_DIFFUSE`.

gamma-ray emission and the residual charged particle background, were modeled using the recommended files[11].

The LAT data were first analyzed to calculate the time-averaged gamma-ray flux and spectral parameters of each candidate. A second analysis was then performed to study the impact of the Sun, a bright gamma-ray source, on the flux of candidates located near the plane of the ecliptic (RGB J0316+090 and RGB J0909+231). Removing time intervals when the Sun was in the ROI of each candidate had a negligible effect on the analysis results.

Spectral points and a light curve were calculated for each candidate, and a temporal analysis was performed to search for flux variability. The timescale of this analysis was adjusted based on the specific candidate flux levels. The flux in each energy or time bin was determined with the spectral indices of all sources fixed to the best-fit values over the full energy and time interval. For an energy or time bin with a test statistic (TS; see Mattox et al. (1996)) less than 9 or fewer than 3 predicted photons (N_{pred}), a 95% confidence level upper limit was calculated.

The light curves were analyzed to search for flux variability with a likelihood method assuming a constant flux for the null hypothesis, following the same procedure as used in the 2FGL catalog. Only two sources showed significant evidence

[11]The files used were `gll_iem_v02_P6_V11_DIFFUSE.fit` for the Galactic diffuse and `isotropic_iem_v02_P6_V11_DIFFUSE.txt` for the isotropic diffuse component available at `http://fermi.gsfc.nasa.gov/ssc/data/p6v11/access/lat/BackgroundModels.html`

of flux variability: RGB J0316+090 and RGB J1058+564. For these two sources, a refined analysis was done, selecting time periods contemporaneous with the VERITAS observation windows. The duration of this contemporaneous period was chosen such that a significant detection ($> 5\sigma$) could be attained, resulting in slightly extended windows of MJD 55055-55145 for RGB J0316+090 and MJD 55160-55185 for RGB J1058+564 with respect to the VERITAS observation window. For these candidates, a butterfly corresponding to the 1σ confidence interval was used to represent the spectral information (Figure 2.3).

The derived spectral indices for the differential power laws obtained for the candidates are relatively hard, ranging from 1.74 to 2.09, as compared to the 2FGL average spectral index of 2.21 $\pm$ 0.01. The integral fluxes above 300 MeV range from 1.55 to 12.4$\times 10^{-9}$ph cm^{-2}s^{-1}, indicating that these six blazars are bright in the high-energy band. The detailed *Fermi*-LAT results for each of these hard-spectrum, bright BL Lacs are summarized in Table 2.3.

2.4.3 *Swift* XRT

The X-ray Telescope (XRT) onboard the *Swift* satellite (Gehrels et al., 2004) is a focusing X-ray telescope sensitive to photons with energy between 0.2 and 10

[12]Prob is the probability of steady emission as measured from ΔTS per degree of freedom.

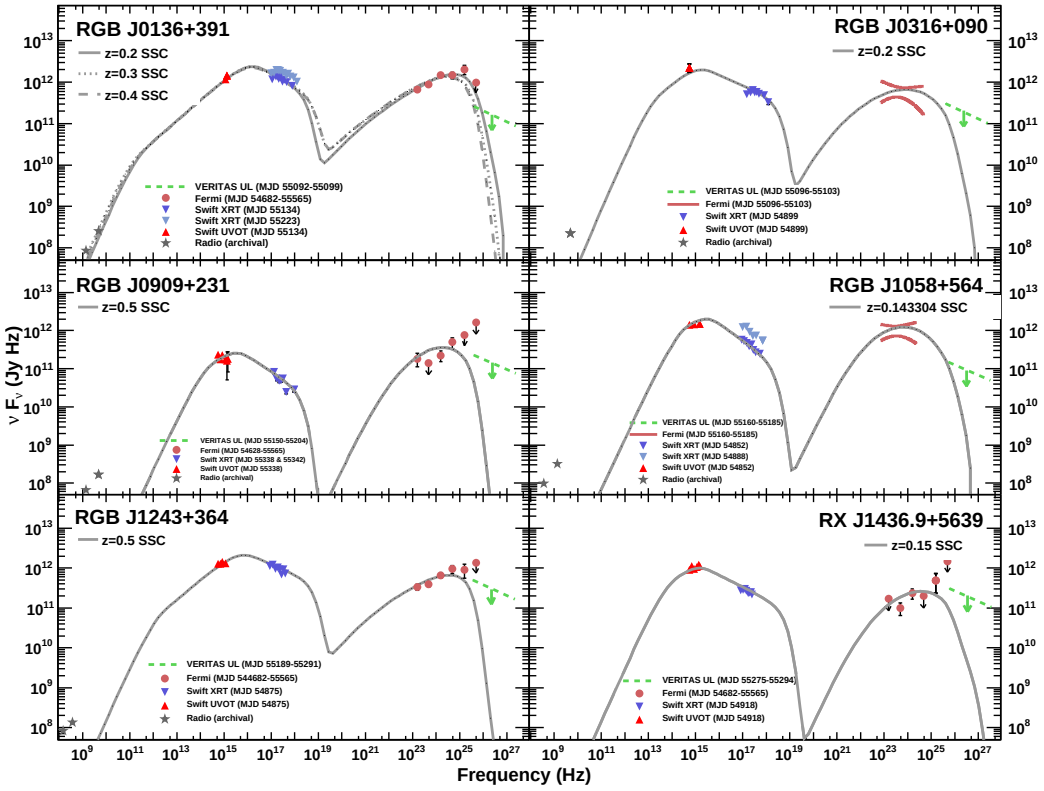

Figure 2.3: Non-contemporaneous broadband SED data for each BL Lac shown with corresponding SSC modeling using the model of Böttcher & Chiang (2002). The modeling results, corrected for the EBL absorption, are shown with grey lines. The archival radio data points are taken from NED and used only as upper limits, accounting for the fact that much of the radio emission may result from diffuse synchrotron emission in the radio lobes of the jet. See the text for a more detailed description of the model parameters, with values listed in Table 2.6.

Table 2.3: Summary of *Fermi*-LAT observations and analysis results. A variability study was completed using 29 months of data for all sources. For steady sources, the spectral analysis is completed for 29 months of data. The two variable sources RGB J0316+090 and RGB J1058+564 show spectral analysis results for LAT data coincident with a slightly expanded window as compared to the VERITAS observation window so as to allow a 5σ detection.

Counterpart Name	1FGL Name	Variability Detected?	Prob[12]	MJD Fit Window	TS	Index Γ	Integral Flux $\geq$ 300 MeV [$\times 10^{-9}$ ph cm^{-2}s^{-1}]
RGB J0136+391	J0136.5+3905	no	0.39	54682.7-55565.0	1430	1.78±0.04	12.0±0.7
RGB J0316+090	J0316.1+0904	yes	0.00	55055.0-55145.0	45.7	2.09±0.26	9.5±3.3
RGB J0909+231	J0909.2+2310	no	0.06	54682.7-55565.0	123	1.68±0.13	1.8±0.5
RGB J1058+564	J1058.6+5628	yes	0.00	55160.0-55185.0	37.2	1.98±0.24	12.4±3.8
RGB J1243+364	J1243.1+3627	no	0.60	54682.7-55565.0	627	1.76±0.06	5.6±0.5
RX J1436.9+5639	J1437.0+5640	no	0.24	54682.7-55565.0	132	1.74±0.13	1.6±0.4

keV. The data used for the broadband SED modeling were analyzed as described in Burrows et al. (2005) with the `HEASoft` package Version 6.9 and `XSPEC`[13] Version 12.6.0. All data were taken in photon counting mode and pile up effects are accounted for when count rates exceeded 0.5 counts per second through the use of an annular source region, with a 1-2 pixel inner radius and a 20 pixel outer radius. Each observation is binned and fit with an absorbed power law between 0.3 and 10 keV, with the neutral hydrogen density taken from the Leiden/Argentine/Bonn survey of Galactic HI (Kalberla et al., 2005).

X-ray variability is commonplace for both VHE detected and non-detected blazars. If more than one exposure exists for an object and no variability is detected, the de-absorbed power-law fit of the combined data set is used to constrain the SED modeling. If variability is observed between multiple exposures, results from these separate exposures are shown independently on the SED plot, as is the case for RGB J0136+391 and RGB J1058+564. These blazars show flux variability factors of $\sim$2 and 3 between exposures, respectively. The multiple exposures taken on RGB J0909+231 do not provide sufficient statistics for application of an absorbed power-law model and are therefore summed before fitting. Using Cash analysis (Cash, 1979) did not improve the fitting of the single low-statistics spectra. The summed exposure fit result is shown on the SED.

Each of the absorbed power-law fits applied to the XRT data resulted in pho-

[13] `http://heasarc.nasa.gov/docs/software/lheasoft/xanadu/xspec/XspecManual.pdf`

ton indices greater than 2, with 2-10 keV integral flux levels between 0.3 and 21×10^{-12}ergs cm^{-2}s^{-1}. The index values suggest that the synchrotron component peaks below keV energies, characteristic of ISP blazars. The analysis results for each observation are summarized in Table 2.4.

2.4.4 *Swift* UVOT

The *Swift*-XRT observations were supplemented with simultaneous UVOT exposures taken in the V, B, U, UVW1, UVM2, and UVW2 bands (Poole et al., 2008). The UVOT photometry is performed using the `HEASoft` program *uvotsource*. The circular source region has a 5“ radius and the background region consists of several 15″ radii circles of nearby empty sky. The results are reddening corrected using E(B-V) coefficients (Schlegel et al., 1998). The Galactic extinction coefficients are applied according to Fitzpatrick (1999). The uncertainty in the reddening E(B-V) is the largest source of error, especially in the UV bands for blazars that have a large value of E(B-V). If more than one exposure exists in a specific band for an object, the data from the observation closest to the VERITAS exposure are used, although no significant variability is seen across any band for any blazar. A summary of the UVOT analysis results is presented in Table 2.5.

[14]Statistics extracted from each single observation are too low to fit an absorbed power law. The combination of the three exposures is used.

Table 2.4: Summary of *Swift*-XRT observations and analysis results. Photon counting mode data were fit with absorbed power laws using HI column densities from Kalberla et al. (2005). Unabsorbed data were used for SED modeling. For multiple observations showing no significant variability, exposures were combined to improve statistics. If variability was detected between observations, both results are shown on the SED, although the model is only shown for the XRT observation falling closest to the window of VERITAS observations.

Counterpart Name	Observation ID	MJD	Exposure Time [ks]	HI [$\times 10^{20}$cm^{-2}]	Flux (2-10 keV) [$\times 10^{-12}$ ergs cm^{-2}s^{-1}]	Photon Index	χ^2 (DOF)	Used in SED
RGB J0136+391	00039107001	55134	1.6	6.17	12.1±1.0	2.24±0.05	38.0 (40)	yes
	00039107002	55223	2.9	6.17	21.4±1.0	2.16±0.03	107.2 (84)	yes
RGB J0316+090	00038370001	54899	2.6	12.6	7.0±0.6	2.13±0.06	34.7 (35)	yes
RGB J0909+231[14]	00040540001	55338	1.3	−−	−−	−−	−−	no
	00040540002	55338	1.9	−−	−−	−−	−−	no
	00040540003	55342	1.6	−−	−−	−−	−−	no
	combined	−−	−−	4.63	0.3±0.06	2.7±0.2	5.1 (5)	yes
RGB J1058+564	00038215001	54852	3.8	0.78	2.2±0.2	2.60±0.05	42.4 (39)	yes
	00038453001	54888	1.0	0.78	6.3±0.6	2.48±0.07	25.9 (27)	yes
RGB J1243+364	00038445001	54875	2.1	1.4	8.2±0.5	2.33±0.05	50.4 (46)	yes
RX J1436.9+5639	00038435001	54918	5.1	1.55	2.4±0.2	2.31±0.05	40.6 (31)	no
	00038289001	54918	4.9	1.55	2.4±0.2	2.27±0.05	43.3 (31)	no
	combined	−−	−−	1.55	2.4±0.2	2.29±0.04	72.5 (78)	yes

Table 2.5: Summary of *Swift*-UVOT observations and analysis results.

Target	Observation ID	Date [MJD]	Band	Frequency [Hz]	νF_ν [Jy Hz]	Used in SED?
RGB J0136+391	00039107001	55134	UVW1	1.14×10^{15}	$(1.16 \pm 0.15) \times 10^{12}$	y
	00039107001	55134	UVM2	1.34×10^{15}	$(1.44 \pm 0.30) \times 10^{12}$	y
RGB J0316+090[15]	00038370001	54899	V	5.55×10^{14}	$(2.24 \pm 1.04) \times 10^{12}$	y
	00038370001	54899	U	8.57×10^{14}	$(2.92 \pm 3.87) \times 10^{12}$	n
	00038370001	54899	UVW1	1.14×10^{15}	$(2.44 \pm 7.64) \times 10^{12}$	n
	00038370001	54899	UVW2	1.48×10^{15}	$(2.8 \pm 18.5) \times 10^{12}$	n
RGB J0909+231	00040540001	55338	V	5.55×10^{14}	$(2.35 \pm 0.11) \times 10^{11}$	y
	00040540001	55338	B	6.93×10^{14}	$(1.77 \pm 0.23) \times 10^{11}$	y
	00040540001	55338	U	8.57×10^{14}	$(2.26 \pm 0.21) \times 10^{11}$	y
	00040540001	55338	UVW1	1.14×10^{15}	$(1.78 \pm 0.18) \times 10^{11}$	y
	00040540001	55338	UVM2	1.34×10^{15}	$(1.63 \pm 0.22) \times 10^{11}$	y
	00040540001	55338	UVW2	1.48×10^{15}	$(1.80 \pm 0.19) \times 10^{11}$	y
	00040540002	55338	UVM2	1.34×10^{15}	$(1.90 \pm 0.22) \times 10^{11}$	n
	00040540003	55338	UVW2	1.48×10^{15}	$(1.74 \pm 0.20) \times 10^{11}$	n
RGB J1058+564	00038215001	54852	V	5.55×10^{14}	$(1.42 \pm 0.04) \times 10^{12}$	y
	00038215001	54852	U	8.57×10^{14}	$(1.45 \pm 0.04) \times 10^{12}$	y
	00038215001	54852	UVW2	1.48×10^{15}	$(1.49 \pm 0.05) \times 10^{12}$	y
	00038453001	54888	B	6.93×10^{14}	$(1.64 \pm 0.07) \times 10^{12}$	n
	00038453001	54888	U	8.57×10^{14}	$(1.70 \pm 0.06) \times 10^{12}$	n
	00038453001	54888	UVW1	1.14×10^{15}	$(1.66 \pm 0.06) \times 10^{12}$	n
RGB J1243+364	00038445001	54875	V	5.55×10^{14}	$(1.28 \pm 0.05) \times 10^{12}$	y
	00038445001	54875	B	6.93×10^{14}	$(1.30 \pm 0.04) \times 10^{12}$	y
	00038445001	54875	U	8.57×10^{14}	$(1.42 \pm 0.05) \times 10^{12}$	y
	00038445001	54875	UVW1	1.14×10^{15}	$(1.34 \pm 0.05) \times 10^{12}$	y
	00038445001	54875	UVM2	1.34×10^{15}	$(1.49 \pm 0.05) \times 10^{12}$	y
	00038445001	54875	UVW2	1.48×10^{15}	$(1.47 \pm 0.05) \times 10^{12}$	y
RX J1436.9+5639	00038435001	54918	V	5.55×10^{14}	$(9.03 \pm 0.09) \times 10^{11}$	y
	00038435001	54918	B	6.93×10^{14}	$(1.14 \pm 0.07) \times 10^{12}$	y
	00038435001	54918	U	8.57×10^{14}	$(9.71 \pm 0.05) \times 10^{11}$	y
	00038435001	54918	UVW1	1.14×10^{15}	$(1.06 \pm 0.06) \times 10^{12}$	y
	00038435001	54918	UVM2	1.34×10^{15}	$(1.21 \pm 0.07) \times 10^{12}$	y
	00038435001	54918	UVW2	1.48×10^{15}	$(1.12 \pm 0.06) \times 10^{12}$	y
	00038289001	54918	V	5.55×10^{14}	$(8.58 \pm 0.05) \times 10^{11}$	n
	00038289001	54918	U	8.57×10^{14}	$(1.06 \pm 0.04) \times 10^{12}$	n
	00038289001	54918	UVW2	1.48×10^{15}	$(1.26 \pm 0.06) \times 10^{12}$	n

2.5 Broadband SSC Modeling

Leptonic models for blazar jet emission attribute the higher energy peak in the SED to the inverse-Compton scattering of lower energy photons off a population of non-thermal, relativistic electrons. These same electrons are responsible for the lower-energy synchrotron emission that makes up the first peak. The target photon field involved in the Compton upscattering can either be the synchrotron photons themselves, as is the case in SSC models, or a photon field external to the jet in the case for EC models.

The previously described multiwavelength data are matched with archival radio data collected from NED. These data are used to test a steady-state leptonic jet model for the broad-band continuum emission from the blazars. Although it has been found that ISP BL Lacs are sometimes better represented by external-Compton models, e.g. Acciari et al. (2009c), taking into account the lack of redshift information and lack of constraints from the broadband data we prefer not to apply an EC model, which would introduce additional free parameters, compared to the SSC model applied here. The model-predicted flux reflects the absorption of VHE gamma rays by the EBL according to the redshift information summarized in Table 2.1 using the model from Gilmore et al. (2009). The level of

[15]Galactic reddening dominates the uncertainty with E(B-V) = 0.356; U, UVW1, UVW2 band flux measurements do not constrain the SED.

TeV absorption resulting from this model is consistent with the absorption derived from the Finke et al. (2010) and Franceschini et al. (2008) models.

The SSC model applied to the multiwavelength data is the equilibrium version of the Böttcher & Chiang (2002) model, as described in Acciari et al. (2009c). In this model, the emission originates from a spherical blob of relativistic electrons with radius R. This blob is moving down the jet with a Lorentz factor Γ, which corresponds to a speed of $\beta_\Gamma c$. The jet axis is aligned toward the line of sight with an angle $\theta_{\rm obs}$, which results in Doppler boosting with a Doppler factor $D = (\Gamma[1 - \beta_\Gamma \cos\theta_{\rm obs}])^{-1}$. In order to minimize the number of free parameters, we assume that $\theta_{obs} = 1/\Gamma$, often referred to as the critical angle, for which $\Gamma = D$.

Within the model, nonthermal electrons are injected and accelerated into a power-law distribution $Q(\gamma) = Q_0\gamma^{-q}$ between the low- and high-energy cut-offs, γ_{min} and γ_{max}. The radiation mechanisms considered lead to an equilibrium between particle injection, radiative cooling and particle escape. This particle escape is characterized with an escape efficiency factor η, such that the time scale of escape $t_{\rm esc} = \eta\, R/c$. This results in a particle distribution which streams along the jet with a power L_e. Synchrotron emission results from the presence of a tangled magnetic field B, with a Poynting flux luminosity of L_B.

The two parameters L_e and L_B allow the calculation of the equipartition parameter $\epsilon_{Be} \equiv L_B/L_e$. This equipartition parameter is used as an estimator of the

feasibility of the model, where models which result in $\epsilon_{Be} \sim 1$ are preferred. If the particle energy density greatly dominates over the magnetic field energy density, namely a particle dominated scenario, then the magnetic field cannot serve to collimate the jet. Following this design, acceptable parameters should result in at least partition conditions with $L_B \geq L_e$.

The broadband SED for each blazar can be seen in Figure 2.3, with the SSC model parameters for each representation summarized in 2.6. For each blazar, the archival radio data are taken as upper limits as these measurements are believed to contain a large amount of radiation produced in the radio lobes in addition to the synchrotron emission from the jet. The modeling for each of the six blazars shows synchrotron peak locations $\sim 10^{15}$ Hz, characteristic of borderline ISP/HSP blazars.

RGB J0136+391: This blazar is modeled using the lower of the two variable X-ray states for three different assumed redshifts ($z = 0.2, 0.3$ and 0.4). The variability timescale of three months suggested by the factor-of-two variability observed between XRT exposures is not short enough to provide a constraint on the size of the model emission region. Under the assumption that the gamma-ray emission remained steady during the *Fermi* and VERITAS observations, the hard LAT spectrum and low VERITAS upper limit derived for this blazar suggest a steepening of the gamma-ray spectrum at $E \geq 100$ GeV, which could be

Table 2.6: Summary of the broadband SED SSC modeling parameters. See text for parameter descriptions.

Counterpart Name	z	γ_{min}	γ_{max}	q	t_{esc} [hr]	B [Gauss]	Γ	Radius [cm]	L_e [ergs/sec]	L_B [ergs/sec]	L_B/L_e	t_{min}[hr]
RGB J0136+391	0.2	4.0×10^4	6.0×10^5	2.6	120	0.15	15	3.4×10^{16}	1.1×10^{44}	2.3×10^{43}	2.1×10^{-1}	25.9
RGB J0136+391	0.3	2.5×10^4	5.0×10^5	2.6	50	0.4	15	2.4×10^{16}	1.0×10^{44}	7.8×10^{43}	7.5×10^{-1}	19.2
RGB J0136+391	0.4	2.4×10^4	5.0×10^5	2.6	30	0.45	15	3.0×10^{16}	1.3×10^{44}	1.5×10^{44}	1.1	25.9
RGB J0316+090	0.2	1.5×10^4	7.0×10^5	2.5	15	0.11	15	8.0×10^{16}	9.8×10^{43}	6.5×10^{43}	6.6×10^{-1}	59.2
RGB J0909+231	0.5	2.3×10^4	5.0×10^5	2.8	10	0.1	20	2.5×10^{16}	1.5×10^{44}	9.4×10^{42}	6.4×10^{-2}	17.4
RGB J1058+564	0.1433	4.0×10^4	3.0×10^5	2.9	10	0.25	20	9.0×10^{15}	3.9×10^{43}	7.6×10^{42}	2.0×10^{-1}	4.8
RGB J1243+364	0.5	3.0×10^4	1.0×10^6	2.5	30	0.1	20	1.5×10^{17}	3.2×10^{44}	3.4×10^{44}	1.1	104.1
RX J1436.9+5639	0.15	4.0×10^4	2.5×10^6	2.6	100	0.01	20	2.7×10^{17}	1.5×10^{44}	1.1×10^{43}	7.5×10^{-2}	143.7

caused by the EBL absorption if a redshift $z \geq 0.4$ is assumed. Alternatively, this apparent break could originate from uncorrelated variability in the high and very-high energy bands. More specifically, a low flux state in the VHE band during VERITAS observations could provide a redshift-independent explanation of the apparent spectral softening. Figure 2.3 shows the model predictions, corrected by EBL absorption, for each of the redshift values. Only the model at $z = 0.4$ is compatible with the VERITAS upper limit, which also results in a framework with balanced radiation and particle energy.

RGB J0316+090: Due to the variability detected in the high-energy band, this blazar is modeled with *Fermi*-LAT data which spans the complete time period sampled by shorter VERITAS observations. The UVOT errors resulting from the E(B-V) reddening correction for this blazar are so large that all exposures except the V band are unconstraining to the SED modeling and therefore not shown. Application of the SSC model for an assumed redshift of $z = 0.2$ results in a particle dominated framework consistent with the VERITAS upper limit.

RGB J0909+231: The SSC model parameters used to describe the broad-band emission of this blazar are determined for a redshift of $z = 0.5$, based on the lower limit derived from Mg II absorption lines found in the SDSS data. The *Swift* X-ray data from three exposures have been summed in order to provide sufficient statistics for absorbed power-law fitting. The model results in a particle-

dominated scenario with a slight discrepancy between the model and the *Fermi* upper limit in the $1-3$ GeV energy bin. Moving the Compton peak accomodates this upper limit only results in an even less favored, particle-dominated emission state.

RGB J1058+564: Due to the variability observed in the LAT band, the SED modeling for this blazar is done with LAT data from the time period coincident with the VERITAS observation window and for the lower of two X-ray states observed. The variability timescale suggested by the variability factor of three observed between XRT exposures is not short enough to provide any constraint on the size of the emitting region. Both X-ray states are shown on the SED for reference. The SSC model shows agreement with the broadband data, although results in a disfavored particle dominated scenario.

RGB J1243+364: The modeling for this blazar is completed for a redshift of $z = 0.5$, based on the new lower limit found from Mg II absorption lines in the public SDSS data. The model agrees with the broadband data and permits parameters at equipartition.

RX J1436.9+5639: The modeling for the broadband data of this blazar allows marginal agreement with the *Fermi* data when completed for the redshift of the spatially coincident galactic supercluster, more specifically $z = 0.15$. The resulting model parameters are far below equipartition, suggesting a particle dom-

inated jet.

2.6 Discussion

Six promising TeV blazar candidates were selected from the 1FGL catalog for observations with VERITAS. These observations resulted in no VHE detections. Initial selection of these candidates from 1FGL power-law fit extrapolation suggested integral flux levels between 1 and 12% of the Crab Nebula flux above 150 GeV after accounting for absorption by the EBL. With additional *Fermi*-LAT data and more information about the blazar redshifts, the expected fluxes were updated to levels between 0.3% and 3.5% of the Crab Nebula flux above 150 GeV. The VERITAS exposure times were allocated based on the initial extrapolated values, resulting in only one upper limit below the updated VHE extrapolation, namely the upper limit for RGB J0136+391. The non-detection of this blazar suggests spectral steepening of the high-energy spectrum that can either be explained by intrinsic spectral curvature, redshift-dependent EBL absorption or uncorrelated variability.

Multiband observations are presented and allow for the construction and SSC modeling of the radio through TeV broadband SEDs. The model applied to these blazars is sufficient to represent the broadband data for each of the six, with model parameters roughly comparable to those found for other VHE-detected

ISPs using the same model (Abdo et al., 2011; Acciari et al., 2009c). The magnetic fields obtained in the modeling are generally low, resulting in disfavored, particle-dominated jets. This condition could be relaxed by including an external photon field for inverse-Compton scattering, allowing solutions closer to equipartition, as was done in Abdo et al. (2011) and Acciari et al. (2009c). However, this scenario has not been explicitly tested. The quality of the data sampling of the inverse-Compton peak and the fact that the redshifts are not well determined for the majority of the objects do not provide sufficient constraints for a model with the extra degrees of freedom associated with adding an external source of seed photons. Similar parameters were also found for the borderline ISP/HSP TeV detected blazar PKS 1424+240, with the exception of the spectral index for the injected electron distribution, which was found to be very soft ($q = 5.1$, Acciari et al. (2010)), while the typical values for this model fall between q =2.3 and 2.7.

Each of these blazars shows a synchrotron peak frequency characteristic of the ISP/HSP divide, namely $\nu_{synch} \sim 10^{15}$. Additionally, each of these BL Lacs exhibits a similar flux level within the high-energy gamma-ray band, showing comparable L_{synch} and L_{IC}. This commonality of sub-type and peak luminosities is likely a bias introduced to the selection process through the sensitivity of the *Fermi* LAT instrument being greater in the 300 MeV - 100 GeV band as compared to the $\geq$100 GeV band. Nearby blazars releasing a large fraction of power above

100 GeV are known to be good candidates for detection in the VHE regime. This type of power emission is characteristic of HSP BL Lacs, the most commonly VHE-detected type of blazar, but the least frequently detected BL Lac in the 1FGL and 2FGL catalogs.

Although the selection of these six blazars from high-energy *Fermi*-LAT data did not lead to any new TeV blazar discoveries, the exercise has been very illuminating. We are reminded that when selecting candidates for observation with TeV instruments, accurate redshift information is crucial. Without this information it is difficult to decipher if the lack of TeV emission is due to the intrinsic emission mechanism or the absorption of gamma rays by the EBL. The redshift lower limits that were found in the SDSS for RGB J0909+231 and RGB J1243+364 indicate distances where future TeV detection from a deeper exposure is unlikely. Continued TeV observations of RGB J0136+361, RGB J0316+090 and RX J1436.9+5639, the three sources that remain without solid redshift information, could provide insight into the distance to these sources, while further observations of RBG J1058+564 can be directly applied to further investigate the emission mechanism at work within the blazar jet.

Chapter 3

The Blazar Emission Environment: Insight from Soft X-ray Absorption

This work has been accepted for publication in the Astrophysical Journal (*Furniss, A. et al. 2013, ApJ, accepted*). The corresponding author of the work is Amy Furniss. No content was modified aside from formatting. The full author list of this work can be found in Appendix C.

Abstract

Collecting experimental insight into the relativistic particle populations and emission mechanisms at work within TeV-emitting blazar jets, which are spatially unresolvable in most bands and have strong beaming factors, is a daunting task. New observational information has the potential to lead to major strides in understanding the acceleration site parameters. Detection of molecular carbon monoxide (CO) in TeV emitting blazars, however, implies the existence of intrinsic gas, a connection often found in photo-dissociated region models and numerical simulations. The existence of intrinsic gas within a blazar could provide a target photon field for Compton up-scattering of photons to TeV energies by relativistic particles. We investigate the possible existence of intrinsic gas within the three TeV emitting blazars RGB J0710+591, W Comae and 1ES 1959+650 which have measurements or upper limits on molecular CO line luminosity using an independent technique which is based on the spectral analysis of soft X-rays. Evidence for X-ray absorption by additional gas beyond that measured within the Milky Way is searched for in Swift X-ray Telescope (XRT) data between 0.3 and 10 keV. Without complementary information from another measurement, additional absorption could be misinterpreted as an intrinsically curved X-ray spectrum since both models can frequently fit the soft X-ray data. After breaking this degeneracy, we do not find evidence for intrinsically curved spectra for any of the three blazars. Moreover,

no evidence for intrinsic gas is evident for RGB J0710+591 and W Comae, while the 1ES 1959+650 XRT data support the existence of intrinsic gas with a column density of $\sim 1 \times 10^{21}\, cm^{-2}$.

3.1 Introduction

Within the canonical classification of active galactic nuclei (AGN), blazars are a type of active galaxy with a relativistic jet pointed toward the observer. These galaxies harbor relativistic particle populations with intrinsic emission characteristics which largely remain difficult to characterize. Blazars produce a non-thermal spectral energy distribution (SED), characterized by two broad peaks in the νF_ν representation. The source of the lower-energy peak can be attributed to the synchrotron radiation of relativistic leptons in the presence of a magnetic field. The mechanism responsible for this relativistic population of leptons (e. g. diffusive parallel shock acceleration, oblique shock acceleration or magnetic reconnection driven flows) remains an open question.

The origin of the higher-energy SED peak has been attributed to inverse-Compton up-scattering by the relativistic jet leptons of either the synchrotron photons themselves, namely synchrotron self-Compton (SSC) emission, or a photon field external to the jet, namely external Compton (EC) emission (e. g. Dermer et al. (1992); Maraschi et al. (1992)). This external field of photons could arise from emission from a dusty torus, broad line region or some other source within the blazar. The key feature that distinguishes EC emission from SSC emission, therefore, is the presence of additional gas that can supply an external photon field. Alternative models attribute the higher energy peak to hadron acceleration

leading to proton synchrotron emission and/or pion production accompanied by resulting cascade emission (e. g. Aharonian et al. (2002); Bednarek (1993); Mücke & Protheroe (2000); Dermer et al. (2012)).

Blazars are sub-classified as flat-spectrum radio-loud quasars if broad emission lines are visible or, otherwise, as BL Lac objects. BL Lac objects are sub-categorized based on the frequency location of the lower-energy peak, with low-synchrotron-peaked (LSP) BL Lac objects having a peak below 10^{14} Hz, intermediate-synchrotron-peaked (ISP) BL Lac objects peaking between 10^{14} and 10^{15} Hz and high-synchrotron-peaked (HSP) BL Lac objects showing a peak above 10^{15} Hz (Abdo et al., 2010c). Across these different sub-classes, blazars exhibit a continuous variation in their SED. This has been interpreted as an evolutionary sequence associated with the variation of the diffuse radiation field in the surroundings of the relativistic jet (Fossati et al., 1998; Böttcher & Chiang, 2002; Ghisellini & Tavecchio, 2008). Under this paradigm, LSP blazars are expected to have an appreciable external radiation field which facilitates effective cooling and favors a EC broadband representation while HSPs lack a source of external radiation and would be described with an SSC emission scenario.

Measurements which can probe for the existence of intrinsic gas which might produce an external radiation field for Compton up-scattering, however, are challenging for BL Lac objects . The bright, non-thermal continuum emitted by the

blazar jet makes the discrimination between SSC and EC emission mechanisms difficult. Broadband modeling of BL Lacs is a common method for the investigation of the non-thermal emission mechanism at work within a blazar jet (e. g. Tramacere et al. (2011); Aleksić et al. (2012); Abramowski et al. (2012)). These models utilize various input parameters which describe the non-thermal emission, including the particle injection parameter, q, which also represents the index of the relativistic electron energy distribution in the absence of significant cooling processes which can deform the power-law emission. The relativistic particles are directly responsible for the synchrotron emission which makes up the lower energy SED peak. Since the spectrum of synchrotron radiation follows from the energy distribution of the emitting particles, the highest energy particles can be directly probed through X-ray observations. More specifically, the observed radiation spectrum can be translated into the spectrum of relativistic particles emitting that synchrotron radiation.

Two functional forms are commonly adopted to describe the observed synchrotron spectrum: a power-law model and a log-parabolic model. A power-law synchrotron spectrum with photon index α originates from a particle power-law energy spectrum with index $q = 2\alpha + 1$ (Rybicki & Lightman, 1979), where q is equal to the index of the input particle distribution in the absence of a cooled high energy tail. Similarly, a log-parabolic radiation spectrum can be produced

by a log-parabolic distribution of relativistic particles (Paggi et al., 2009) and can be interpreted as evidence for a statistical acceleration process (e.g. Tramacere et al. (2007); Massaro et al. (2006, 2004); Costamante (2001); Tagliaferri et al. (2003)). This log-parabolic emission can also be interpreted as representing a power-law particle distribution with a cooled high energy tail, producing an intrinsically curved X-ray spectrum. An accurate determination of the spectral shape of the underlying population is key in the elucidation of the relativistic acceleration mechanism at work within a blazar jet. Fundamentally different acceleration methods produce varying particle spectra, and intrinsic spectral curvature is a possible signature of statistical acceleration.

Regardless of the intrinsic spectral shape of the synchrotron emission, the non-thermal X-ray radiation from any extragalactic X-ray emitter undergoes absorption by the interstellar medium of our own Galaxy. The effective energy-dependent cross section results from the absorption of photons by intervening elements such as (but not limited to) C, N and O, an effect extending up to 10 keV. These absorption cross sections have been calculated per neutral hydrogen column density (N_{HI}) as a function of energy in the 0.03-10 keV range (Morrison & McCammon, 1983) and can be used to estimate the amount of absorption extragalactic X-ray emission undergoes because of the intervening gas within the Milky Way.

Both an absorbed power law and an absorbed log parabola have been shown

to produce acceptable fits to blazar spectral data between 0.3 and 10 keV. The hydrogen column density that is used to scale the abundance of the additional absorbing elements is typically fixed to the Galactic value as measured by the LAB survey (Kalberla et al., 2005). In practice, these fits do not allow for the presence of additional gas in the blazar host galaxy. There have, however, been a limited number of blazars which, when fit with an absorbed power-law model with a free column density, show a fitted value in excess to that measured in the Milky Way (e. g. Aliu et al. (2011a, 2012b)). However, some ambiguity in the interpretation of the data remain. For these instances, the use of an absorbed log-parabolic model with a fixed Galactic N_{HI} column density allows for an intrinsically curved spectrum and can provide an improved fit to the X-ray data without requiring additional absorption within the blazar emission region.

We argue that an apparently curved spectrum observed in TeV BL Lacertae objects may, in some cases, be partially or entirely due to intrinsic blazar column density beyond that measured within our own Galaxy, similarly to what was found in Tavecchio et al. (2002) for a flat-spectrum radio quasar. Detection of additional X-ray absorption exceeding that expected from the Milky Way, therefore, might provide an experimental probe of the emission mechanism at work within TeV blazars (e. g. SSC or EC emission). To investigate the degeneracy between intrinsic curvature in the X-ray spectrum and additional absorption from gas in

the blazar host galaxy, we utilize independent observations of the gas content in the surroundings of the blazars.

Recent millimetric observations of CO have probed the molecular gas content in three TeV-emitting blazars (Fumagalli et al., 2012). A common result of photo-dissociation region (PDR) models and numerical simulations is that CO molecules form in regions where the UV radiation has been shielded by gas and dust, (e. g. Tielenn & Hollenbach (1985); Krumholz et al. (2009); Glover & Clark (2012)). The detection of molecular gas in a galaxy is therefore a signpost of additional intervening material in the surroundings of the blazar, similar to the interstellar gas that absorbs soft X-rays within our own Galaxy. While the exact conversion between the observed CO column density and the hydrogen column density (both in atomic and molecular phase) would require a detailed knowledge of the chemical and physical state of the gas as well as of the impinging radiation field, it is reasonable to expect that the presence of CO is associated with a hydrogen column density >10 $M_{\odot}pc^{-2}$ ($\sim 1 \times 10^{21} cm^{-2}$). Similarly, in normal conditions it would be surprising to find regions in which the N_{HI} column density greatly exceeds 10 $M_{\odot}pc^{-2}$ without a molecular phase.

Millimetric observations that are sufficiently deep to map CO in blazars have thus far only been completed for three sources, namely RGB J0710+591, W Comae and 1ES 1959+650. With the understanding that a sample of three blazars is far

too limited to draw general conclusions, we investigate the relation between the presence of molecular gas and evidence for intrinsic column density in blazars as well as intrinsic X-ray spectral curvature, as inferred from spectral fitting.

In this work we show that the possibility of combining independent diagnostics at different frequencies has immediate implications for the physical interpretation of emission processes at work within TeV-emitting blazar jets. In Section 2 we discuss the *Swift* XRT observations and data reduction which allow for the investigation of additional absorption by intrinsic gas. In Section 3 we summarize the results of the spectral analysis for each source, addressing the possibility for both intrinsic absorption and spectral curvature. Finally, we discuss our results in a broader context with regard to blazar non-thermal emission and the implications for the blazar evolutionary theory.

3.2 Observations and Data Reduction

The data set includes all *Swift* X-ray Telescope (XRT) exposures of RGB J0710+591, W Comae, and 1ES 1959+650 since the launch of the instrument in November 2004 (Gehrels et al., 2004). The summary of each exposure used can be found in Tables 3.1-3.4. The XRT is a grazing incidence Wolter-I telescope which focuses X-rays between 0.2 and 10 keV onto a 100 cm^2 CCD (Burrows et al., 2005). The data were analyzed using the `HEASoft` package v6.12. Event files were

cleaned and calibrated with standard criteria with the *xrtpipeline* task, using only events between 0.3 and 10 keV having a grade 0-12 for windowed timing (wt) mode and 0-2 for photon counting (pc) mode. Additionally, events having energy between 0.4 and 0.7 keV were removed from the analysis due to the effects of the oxygen edge at 0.54 keV[1]. More details on the *Swift* XRT effective area can be found in Evans et al. (2009).

For windowed timing mode, rectangular source regions with length and width of 45 and 8 pixels were used for spectral analysis. Background regions were extracted from similarly sized rectangular regions of nearby source-free sky, aligned along the windowed timing one dimensional stream in sky coordinates.

For photon counting mode, circular source regions of radius 20 pixels and centered on the source were used along with similarly sized background regions of nearby source-free sky. If a source showed a count rate greater than 0.5 counts per sec, pileup was accounted for by using an annular source region with inner radius of 2 pixels and outer radius 20 pixels to remove the pile-up contamination in the inner part of the point spread function. For 1ES 1959+650, a source showing consistently high count rates between 3 and 12 counts per second, we only include windowed timing exposures lasting more than 0.5 ks.

The response matrices[2] available from CALDB were used to create ancillary

[1] `heasarc.nasa.gove/docs/swift/proposals/swift_responses.html`

[2] Windowed timing analysis used `swxwt0to2s6_20070901v012.rmf` and photon counting analysis used `swpc0to12s6_20070901v011.rmf`.

response files with *xrtmkarf*. For single observations with sufficient statistics to allow spectral fitting, source spectra were binned to require 30 counts per bin. Single exposures providing count levels too low to allow for the bin minimum required for accurate χ^2 minimization fitting were first summed with *xselect*, with the exposure files summed with *ximage*, before being binned to require 30 counts per bin. This summation was only necessary for the low count levels found for W Comae. Summing all photon counting mode exposures of W Comae provided 176 bins with more than 30 counts. It is noted that the summation of these exposures introduced a possibility for summing different spectral states.

3.3 Spectral Analysis and Results

The spectral analysis was performed with `XSPEC`[3] Version 12.7.1 and a suite of in-house IDL routines. We fit the data with two spectral models. The first is an absorbed power-law model *(wabs(powerlaw)* in XSPEC), with an additional exponent to represent additional neutral hydrogen column density beyond the Milky Way

$$F(E)_{PL} = Ke^{-(N_{\rm HI}^{\rm MW}+N_{\rm HI}^{\rm INT})\sigma(E)}(E)^{-\alpha}, \tag{3.1}$$

referred to as the PL model for the remainder of this work, where α is the spectral

[3] `http://heasarc.nasa.gov/docs/software/lheasoft/xanadu/xspec/XspecManual.pdf`

slope, K is the normalization parameter and $\sigma(E)$ is the non-Thompson energy dependent photoelectric cross section from Morrison & McCammon (1983). N_{HI}^{MW} is the neutral hydrogen column density within the Milky Way, as measured by the LAB survey[4]. The LAB-measured neutral hydrogen densities for each blazar are $4.16\times10^{20}\mathrm{cm}^{-2}$, $1.97\times10^{20}\mathrm{cm}^{-2}$ and $1.00\times10^{21}\mathrm{cm}^{-2}$ for RGB J0710+591, W Comae and 1ES 1959+650, respectively. N_{HI}^{INT} is the blazar neutral hydrogen column density, both in units of cm^{-2}. We note that this analysis does not allow differentiation between blazar-intrinsic and intervening gas residing along the line of sight to the blazar. With the possibility for galaxy clustering, the local environment around the blazars may contain an overdensity of galaxies that can contribute to the observed absorption. Any additional column density found through this analysis is assumed to be in the vicinity of the blazar.

The LAB survey consists of observations of 21-cm emission from Galactic neutral hydrogen over the entire sky. The LAB Survey is a sensitive Milky Way neutral hydrogen survey, with extensive coverage both spatially and kinematically. The survey merges the Leiden/Dwingeloo Survey (LDS: Hartmann & Burton (1997)) of the sky north of -30 degrees declination with the Instituto Argentino de Radioastronoma Survey (IAR: Arnal et al. (2000); Bajaja et al. (2005)) of the sky south of -25 degrees declination. Uncertainties in N_{HI}^{MW} column densities, as reported by the LAB survey, are between 2 and 3%, with $\sim$1% from scale

[4]Kalberla et al. (2005), `www.astro.unibonn.de/hisurvey/profile/`

uncertainty and $\sim 1\%$ from uncertainties in the correction for stray radiation.

The second spectral model applied to the data is an absorbed log-parabola *(wabs(logpar)* in XSPEC) with an additional exponent to represent additional neutral hydrogen column density beyond the Milky Way, referred to as the LP model for the remainder of this work. This model has been suggested to better represent TeV-detected blazar X-ray spectra (e. g. Massaro et al. (2008); Tramacere et al. (2007)). This model allows the spectral index to vary as a function of energy, according to the equation

$$F(E)_{LP} = Ke^{-(N_{\rm HI}^{\rm MW}+N_{\rm HI}^{\rm INT})\sigma(E)}(E)^{-(\alpha+\beta\log(E))}, \tag{3.2}$$

with a normalization factor K, photoelectric cross section and hydrogen column densities similar to those described for the PL model above.

These models were fit to the XRT data of the three blazars with both $\rm N_{HI}^{INT}$ set to zero and with $\rm N_{HI}^{INT}$ allowed to vary, while requiring it to remain equal to or greater than zero. The best fits for each of the models are shown in Figure 3.1 for each of the blazars. These fits are completed for the Observation ID 0003156006 for RGB J0710+591, the summed exposure of W Comae and Observation ID 00035025004 for 1ES 1959+650. For RGB J 0710+591 and 1ES 1959+650, the fits are shown for the exposure with the highest statistics and are meant to be representative of the fitting results. The fitted parameters from Figure 3.1 are

shown in bold in Tables 3.1, 3.3 and 3.4.

The parameter spaces for the spectral models as applied to the data are illustrated by reduced χ^2 contours in Figures 3.2-3.4. The N_{HI}^{INT} column density is allowed to vary when producing these contours, except for left hand column of Figure 3.3, when illustrating the fitted α and β parameters resulting for the LP model with and without a N_{HI}^{INT} column density. These contours show parameter constraints (or lack thereof) during the spectral χ^2 fitting procedures. The white dotted, dashed and dash-dotted lines represent the one, two and three sigma confidence contours on the joint distribution of parameters.

3.3.1 RGB J0710+591

The spectral models were applied to each of the 13 *Swift* XRT observations of RGB J0710+591 and are summarized in Table 3.1. When fit with both PL and LP models which allow for N_{HI}^{INT} column density, there is no significant evidence for the existence of additional gas, e. g. N_{HI}^{INT} parameters are consistent with zero. These fits provide parameter values equivalent to the N_{HI}^{INT}-lacking fits. Due to this redundancy, the resulting parameters are only quoted for fits where N_{HI}^{INT} is not included. The exposures provide comparable fit qualities for the N_{HI}^{MW} only and N_{HI}^{INT} inclusive models.

As shown in Figure 3.3 for the LP model, the fitted α and β parameters

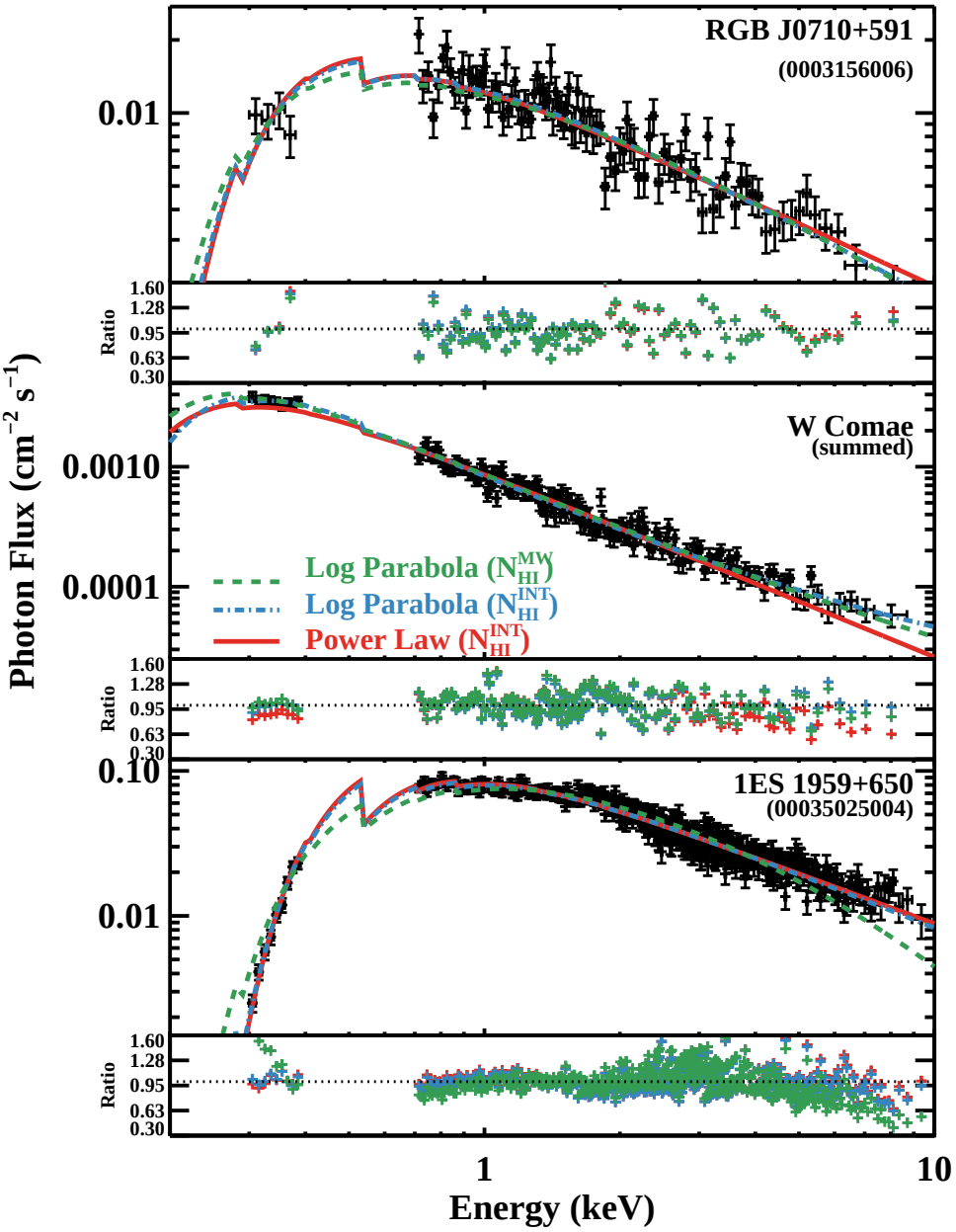

Figure 3.1: The best fit PL and LP models for the RGB J0710+591 Observation 0003156006, the W Comae summed exposure and the 1ES 1959+650 Observation 00035025004. The PL model is shown with fitted N_{HI}^{INT} column density (red solid line), while the LP models are shown for both N_{HI}^{INT} lacking (green dashed line) and N_{HI}^{INT} contributing (blue dash-dotted line) column densities. The feature around ∼0.5 keV arises from the onset of the oxygen interaction cross-section. The fitted parameters are summarized in Tables 3.1, 3.3 and 3.4 in bold.

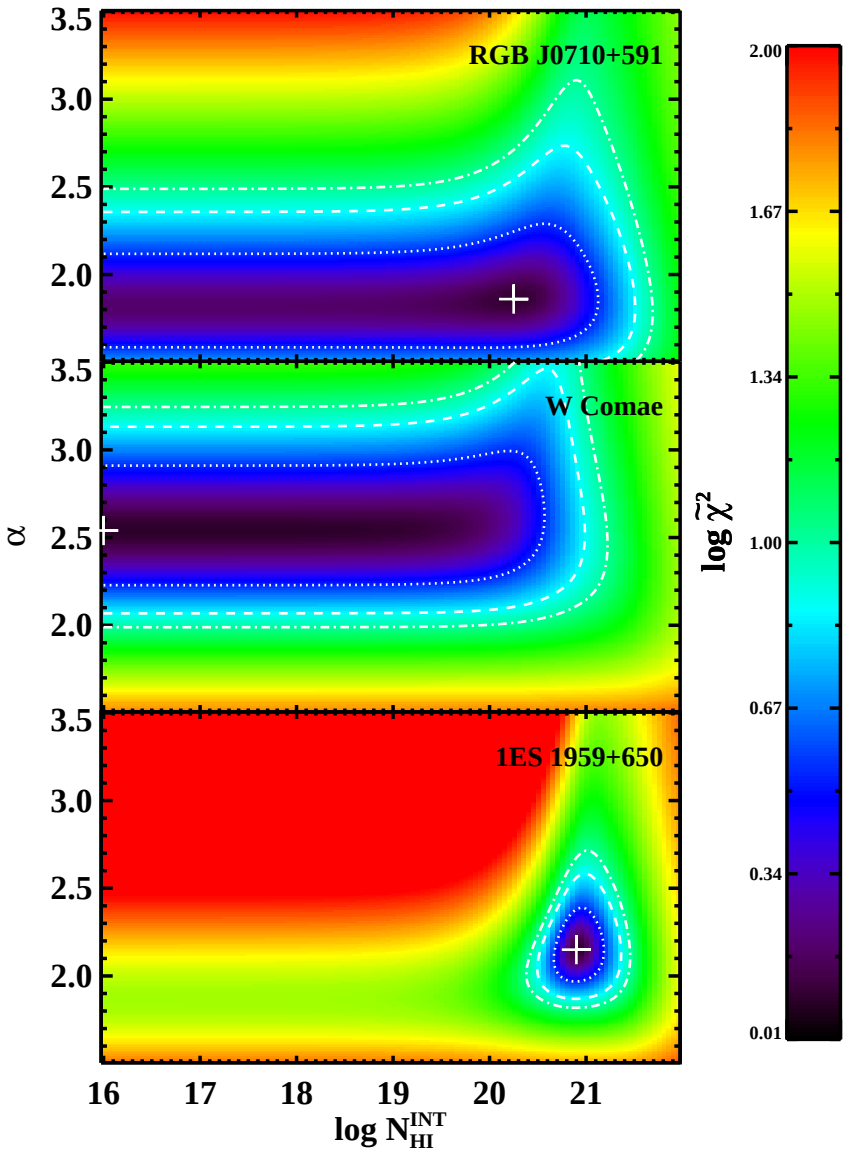

Figure 3.2: The reduced χ^2 contours for the PL model for the RGB J0710+591 Observation 0003156006, the W Comae summed exposure, and the 1ES 1959+650 Observation 00035025004. The white dotted, dashed and dash-dotted lines represent the one, two and three sigma confidence contours on the joint distribution of parameters. The N_{HI}^{INT} parameter for RGB J0710+591 and W Comae (top and middle panels) are shown to be unconstrained, showing that the data do not favor any additional absorption from intrinsic gas within the blazar and beyond that of the Milky Way. The minimum of the fit for RGB J0710+591, however, lies within the defined parameter space, while it does not for the summed W Comae data.

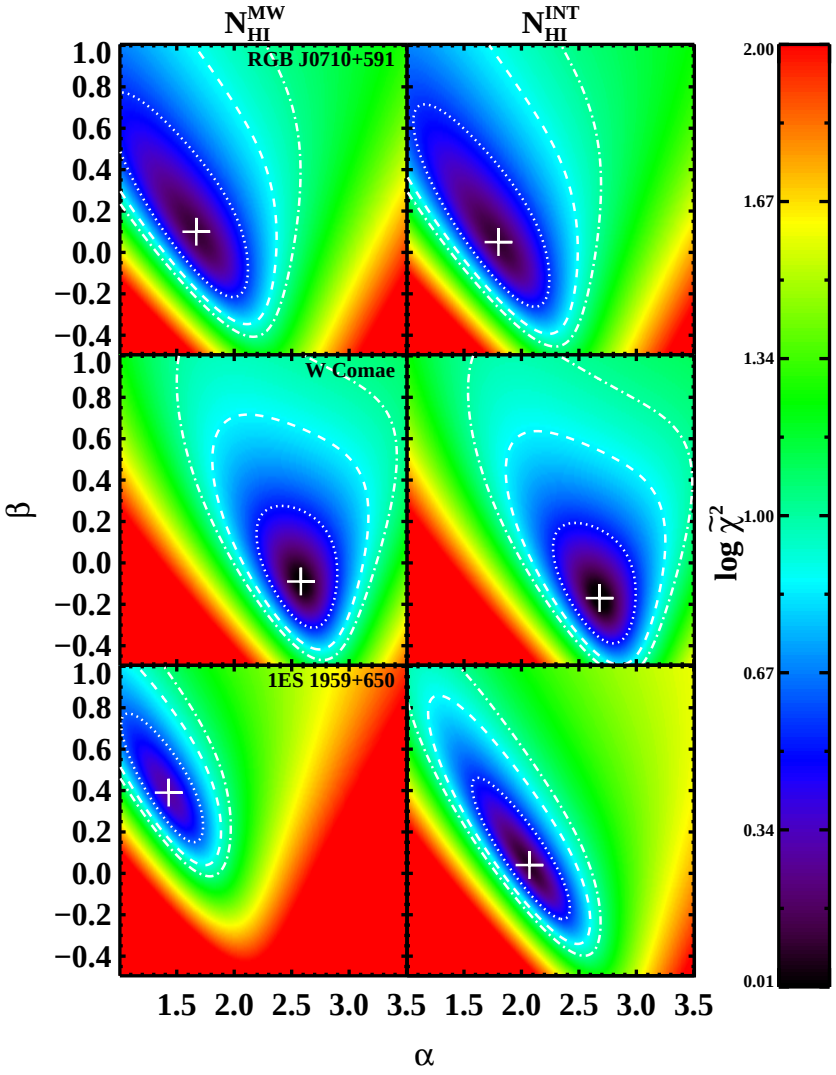

Figure 3.3: Reduced χ^2 contours for the LP model for the RGB J0710+591 Observation 0003156006, the W Comae summed exposure and the 1ES 1959+650 Observation 00035025004 for N_{HI}^{INT} lacking (left) and inclusive (right) column density fits. The contours are similarly represented, as described in Figure 3.2. The index α and curvature β parameters are not seen to significantly change for free and fixed N_{HI} fits for RGB J0710+591 and W Comae. For 1ES 1959+650, the α and β parameters change from 1.5 and 0.4 to 2.1 and 0, respectively, when N_{HI}^{INT} is included in the fit. This change suggests that if N_{HI}^{INT} column density is included, no intrinsic curvature in the spectrum of 1ES 1959+650 is necessary to match the observed spectrum. Note that the x- and y-axes are interchanged in these plots compared to Figure 3.2.

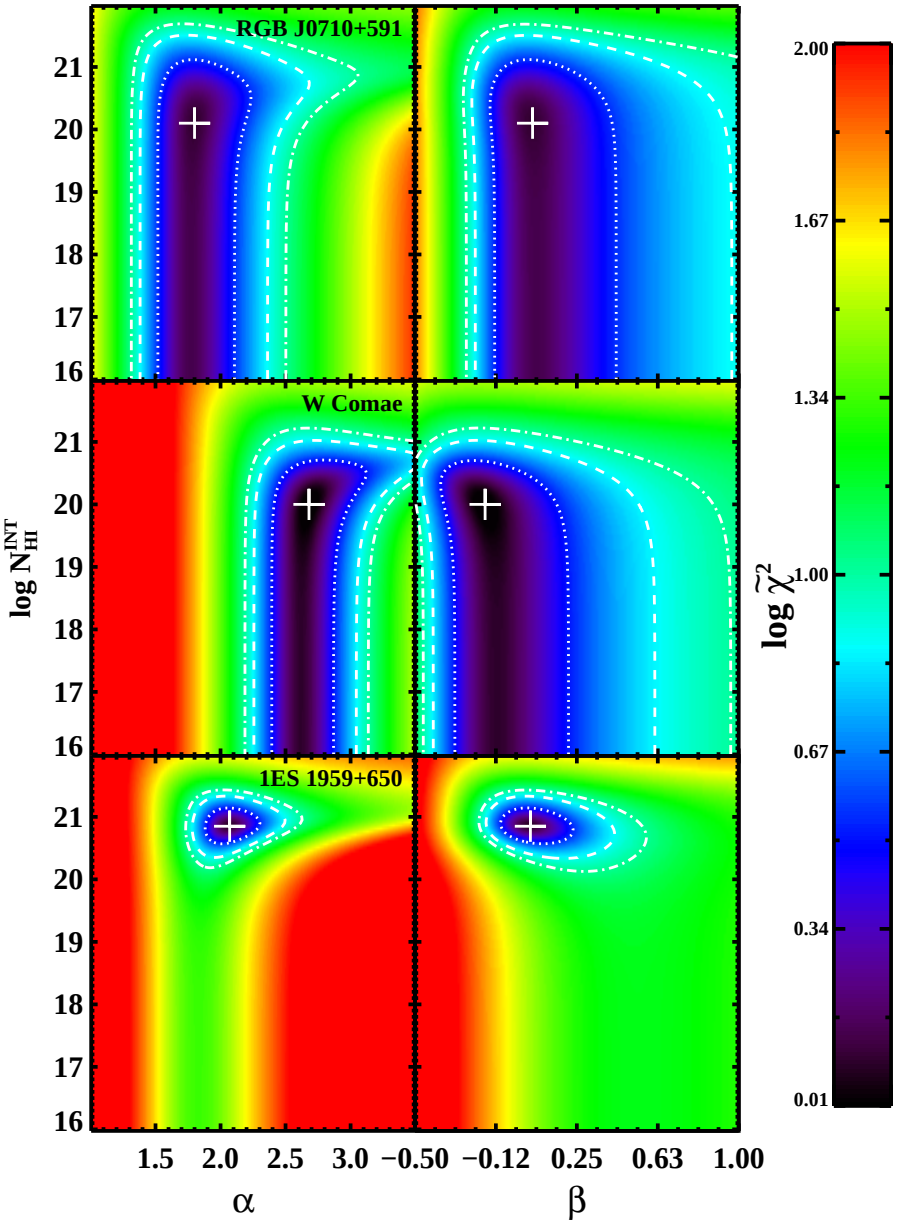

Figure 3.4: Reduced χ^2 contours for the LP model for the RGB J0710+591 Observation 0003156006, the W Comae summed exposure and the 1ES 1959+650 Observation 00035025004 for fitted N_{HI}^{INT} column density. The contours are similarly represented, as described in Figure 3.2. The column densities of RGB J0710+591 and W Comae are seen to be unconstrained, while they are well defined for 1ES 1959+650, showing an intrinsic column density of order $1\times10^{21}\mathrm{cm}^{-2}$, in addition to the $1\times10^{21}\mathrm{cm}^{-2}$ as measured by the LAB Galactic N_{HI} survey.

do not change significantly when allowing for a non-zero N_{HI}^{INT} column density. Additionally, the lack of constraint on the N_{HI}^{INT} column density with respect to these parameters is evident in the top panel of 3.4. When fitting the data with a LP model, negligible curvature (β) is found for a majority of the observations. This $\beta \sim 0$ result indicates that the PL model is sufficient to describe the X-ray emission from this blazar.

There are a few instances where significant negative curvature is found from the LP fitting. This unexpected result is likely due to covariance between the α and β parameters (i. e. moving diagonally in the Figure 3.3 parameter spaces). One can see that in each instance where a negative curvature parameter is found, the fitted index α softens to values of $\sim$2 or less. Due to the unlikely possibility to produce a concave distribution of relativistic particles by traditional acceleration mechanisms, a more physical result might be found by fitting a log-parabolic model with $\beta > 0$ limitations.

3.3.2 W Comae

The PL and LP spectral models were applied to the summed photon counting mode exposures of W Comae. The 73 observations summed to 1.3×10^5 seconds and are summarized in Table 3.2, with the fitting results in Table 3.3. As illustrated by the confidence contours in the middle panels of Figures 3.2 and 3.4,

Table 3.1: Summary of spectral analysis RGB J0710+591 for absorbed PL and absorbed LP. When the possibility of N_{HI}^{INT} was included in the fits, the results were consistent with zero, providing similar fit parameters as found when N_{HI}^{INT} was set to zero. For the fits here, N_{HI}^{MW} was fixed to 4.16×10^{20}cm^{-2} as measured by Kalberla et al. (2005) and N_{HI}^{INT} is set to zero. Observation ID 0003156006 is shown in bold and represents the best fit values for the models shown in the top panel of Figure 3.1.

Observation ID	**Date** [MJD]	**Mode**	**Exposure** [ks]	**Spectral Data Counts**	**PL** α	**2-10 keV Flux** [$\times10^{-11}$ **ergs cm^{-2}s^{-1}**]	**LP** α	**LP** β	**PL** χ^2**/dof**	**LP** χ^2**/dof**
0003156001	54882	pc	3.19	3348	1.76±0.03	3.5±0.1	1.68±0.06	0.1±0.1	81.82/82	80.14/81
0003156002	54887	pc	1.97	1491	1.83±0.05	3.3±0.2	1.6±0.1	0.3±0.2	31.13/37	29.3/36
0003156003	54888	pc	1.84	1978	1.81±0.04	3.6±0.1	1.71±0.08	0.2±0.1	62.55/48	61.01/47
0003156004	54889	wt	1.97	4231	1.77±0.03	5.1±0.2	1.78±0.05	-0.02±0.07	97.05/93	97/92
0003156005	54890	wt	1.91	2824	1.79±0.03	4.6±0.2	1.69±0.07	0.2±0.1	69.16/66	65.97/65
0003156006	**54891**	**wt**	**2.19**	**4735**	**1.81±0.03**	4.6±0.2	**1.73±0.05**	**0.10±0.08**	**128.09/100**	**122.37/99**
0003156007	54892	wt	1.97	4278	1.78±0.03	4.9±0.2	1.76±0.05	0.05±0.08	104.55/95	104.09/94
0003156008	55975	wt	1.25	1685	1.97±0.05	3.2±0.2	2.09±0.07	-0.3±0.1	37.64/39	33.42/38
0003156009	55978	wt	1.09	1375	2.07±0.06	1.9±0.2	2.18±0.09	-0.2±0.2	21.16/31	19.53/30
0003156010	55985	wt	0.97	1286	1.93±0.06	2.5±0.2	2.2±0.1	-0.6±0.1	41.59/29	28.09/28
0003156011	55998	wt	1.15	1477	1.84±0.06	2.6±0.2	1.97±0.09	-0.3±0.1	31.44/34	28.68/33
0003156012	56002	wt	0.86	1154	1.91±0.06	2.6±0.2	2.1±0.1	-0.3±0.2	31.78/26	29.08/25
0003156013	56007	wt	1.03	1304	2.15±0.06	1.7±0.2	2.44±0.06	-0.8±0.1	72.35/28	43.7/27

application of the PL and LP models which allow for non-zero N_{HI}^{INT} column density result in N_{HI}^{INT} parameters consistent with zero, showing no significant evidence for an intervening gas within the blazar and providing parameter values equivalent to the fixed N_{HI}^{MW} fits.

Similarly to the LP model result for RGB J0710+591, the fitted α and β parameters do not change significantly when including N_{HI}^{INT}. The negative curvature parameter β found when applying the LP model to the summed W Comae spectra may indicate a correlation in the α and β parameters, similarly as the trend presented in the RGB J0710+591 data. This specific case of negative curvature might also be a result of summing multiple exposures. Investigation of effects due to summing were completed by fitting the summed exposure while ignoring bins between 1.5 and 2.2 keV in order to remove possible pollution from the Si Kα edge. Removing these bins, however, did not change the spectral results.

Spectral effects introduced through the summation of different spectral states and/or flux levels may also introduce distorted spectral features such as concavity (i.e. the summation of a bright soft state with a low hard state). The previously observed broadband variability of blazars at all wavebands and timescales probed supports this possibility. X-ray spectral variability of W Comae during a flare, however, shows the source to harden during periods of elevated flux (Acciari et al., 2009c). We take this behavior as evidence that the concavity of the summed

spectrum is not likely due to the summation of bright soft and low hard states. The 73 observations show the count rate of W Comae to vary between 0.05 and 3.8 counts per second. Details of X-ray variability of BL Lac objects are described in Böttcher & Chiang (2002).

If the resulting χ^2 values are used at face value to determine which model best represents W Comae, one would conclude that the curved LP model is the most appropriate. However, the convex curvature of the radiation spectrum is not easily described by standard acceleration mechanisms and so we favor a PL model over a LP model for W Comae.

Table 3.2: Summary of *Swift* XRT exposures of W Comae, summed for spectral analysis.

Observation ID	**Date [MJD]**	**Exposure [ks]**	**Source Counts**
0003092001	54223	2.45	194
0003092002	54225	4.56	503
0003092003	54226	3.70	403
00031160001	54539	4.38	458
00031160003	54541	2.15	173
00031160004	54553	1.68	436
00031160005	54554	1.63	168
00031219001	54624	8.98	4390
00031219002	54626	5.09	525
00035018001	53672	1.40	40
00031219002	53627	9.89	706
00031219003	53720	8.58	1050

Continued on next page

Table 3.2 – *Continued from previous page*

Observation ID	**Date [MJD]**	**Exposure [ks]**	**Source Counts**
00031219004	54495	2.26	94
00031219005	54499	4.56	122
00031219006	54528	2.06	327
00031219007	54536	1.86	80
00031219009	54589	1.72	264
00031219010	54828	1.52	74
00031219011	54835	1.03	110
00031219012	54842	0.98	60
00031219013	54844	0.94	92
00031219014	54856	0.66	209
00031219015	54863	1.12	189
00031219016	54870	1.31	167
00031219017	54877	0.96	112
00031219018	54884	1.35	372
00031219019	54891	1.54	138
00031219020	54898	1.19	64
00031219021	54912	1.59	96
00031219022	54919	0.87	39
00031219024	54933	0.98	48
00031219025	55175	4.81	182
00031219026	55230	1.02	60
00031219027	55237	1.04	21
00031219028	55245	1.18	45
00031219029	55251	1.23	14
00031219031	55265	0.88	25
00031219032	55272	0.94	174
00031219033	55279	1.09	34
00031219034	55286	0.73	270

Continued on next page

Table 3.2 – *Continued from previous page*

Observation ID	**Date [MJD]**	**Exposure [ks]**	**Source Counts**
00031219035	55293	0.93	549
00031219036	55300	1.16	893
00031219038	55314	1.35	367
00031219039	55335	0.95	297
00031219040	55356	1.97	668
00031219041	55599	0.97	267
00031219042	55605	0.89	370
00031219043	55612	1.12	475
00031219044	55626	1.09	579
00031219045	55636	0.96	235
00031219046	55641	1.19	290
00031219047	55648	1.14	353
00031219048	55661	0.95	374
00031219049	55669	1.20	1725
00031219050	55675	1.14	539
00031219051	55691	1.09	328
00031219053	55710	0.94	418
00031219054	55727	2.33	622
00031219055	55728	2.10	572
00031219056	55960	1.04	3143
00031219057	55967	1.16	358
00031219058	55974	1.33	414
00031219059	55981	1.03	289
00031219060	55988	1.47	454
00031219061	56002	0.92	338
00031219062	56010	1.37	661
00031219063	56023	1.01	334
00031219064	56037	0.88	294

Continued on next page

Table 3.2 – *Continued from previous page*

Observation ID	**Date [MJD]**	**Exposure [ks]**	**Source Counts**
00031219065	56042	0.92	289
00031219066	56053	0.99	283
00031219067	56058	1.05	449
00031219068	56065	1.02	766
00031219069	56072	1.05	364

3.3.3 1ES 1959+650

When fitting both the PL and LP models to 1ES 1959+650, a significant N_{HI}^{INT} column density is derived (see Tables 3.3 and 3.4 for a summary of all results). The α and β parameter for the LP model can be seen to change significantly when N_{HI}^{INT} is included in the fit (Figure 3.3). The β parameter becomes consistent with zero when N_{HI}^{INT} is included in the fit, indicating that if the possibility for intrinsic gas in the blazar emission environment is allowed, the particle population can be represented with an uncurved power-law spectrum. Evidence for additional absorption exceeding that by the Milky Way was also found for power-law fits of XMM X-ray observations of 1ES 1959+650 in Perlman (2000), although the additional column density was interpreted as evidence for a curved log-parabolic spectrum.

The variation of the PL-fitted blazar column density between observations is

Table 3.3: Summary of summed exposure spectral analysis for W Comae for an absorbed PL and LP model. The count rate for W Comae was low enough to require the summation of all photon counting mode exposures before grouping to 30 counts per bin. When N_{HI}^{INT} was included in the fits, the results were consistent with zero and provided redundant fit parameters as found when N_{HI}^{INT} was set to zero. For the fits quoted here, the N_{HI}^{MW} column density is fixed to 1.97×10^{20}cm^{-2}, as found in the LAB survey (Kalberla et al., 2005) and N_{HI}^{INT} is set to zero. The best fit models are shown for the summed exposure in the middle panel of Figure 3.1.

Exposure	**Spectral**	**PL**	**2-10 keV Flux**	**LP**	**LP**	**PL**	**LP**
[ks]	**Counts**	α	[$\times10^{-12}$ ergs cm^{-2}s^{-1}]	α	β	χ^2**/dof**	χ^2**/dof**
132	**9806**	**2.51±0.02**	**1.10±0.02**	**2.56±0.02**	**-0.13±0.04**	**191.94/174**	**163.52/173**

illustrated in the light curve in Figure 3.5, showing the PL N_{HI}^{INT} column densities in comparison to the large flux variations exhibited by the blazar ($\chi^2 = 35089$ for 61 degrees of freedom). The N_{HI}^{INT} values are less variable ($\chi^2 = 320$ for 61 degrees of freedom) with an average of $8{\times}10^{20}\mathrm{cm}^{-2}$, nearly equal to the Galactic contribution of $1.0{\times}10^{21}\mathrm{cm}^{-2}$, as measured by the LAB survey. If the variability of the column density is real, it would suggest that the gas is local to the non-thermal emission region. X-ray variability of AGN is commonly observed (e.g. Mushotzky et al. (1993); Vagnetti et al. (2011)) and has been attributed to the variation of intrinsic absorption and covering fraction of the galaxy (Abrassart & Czerny, 2000; Wachter et al., 1988). As a geometrically selected subtype of jetted AGN, variability of column density within a blazar is possible. However, the variability of column density for 1ES 1959+650 shown in Figure 3.5 might result from the underestimation of the N_{HI}^{INT} errors as they do not account for correlations between fitting parameters.

Table 3.4: Summary of PL spectral analysis for 1ES 1959+650. Only windowed timing exposures of more than 500 seconds are included in this analysis. The Galactic N_{HI} column density was fixed to $1\times10^{21}\mathrm{cm}^{-2}$, as measured by Kalberla et al. (2005) with a ∼3% error. Observation ID 00035025004 is shown in bold and represents the best fit values for the models shown in the bottom panel of Figure 3.1.

Observation ID	**Date** [MJD]	**Exposure** [ks]	**Fixed PL** α	**PL** $N_{HI}^{MW}+N_{HI}^{INT}$ $[\times10^{21}\mathbf{cm}^{-2}]$	**Free PL** α	**2-10 keV Flux** $\times10^{-11}$ [ergs $\mathbf{cm}^{-2}\mathbf{s}^{-1}$]	**Spectral Counts**	**Fixed PL** χ^2/dof	**Free PL** χ^2/dof
00035025001	53479	4.43	2.102±0.008	1.852±0.004	2.40±0.02	13.7±0.1	32782	1019.0/330	380.3/329
00035025002	53874	1.43	2.01±0.02	1.943±0.009	2.32±0.03	13.3±0.3	9270	426.3/192	223.1/191
00035025003	53876	1.99	1.97±0.01	1.846±0.007	2.22±0.02	18.1±0.3	14911	510.3/251	289.5/250
00035025004	**53878**	**5.35**	**1.91±0.01**	**1.753±0.004**	**2.13±0.01**	**25.3±0.2**	**44642**	**1019.0/417**	**500.8/416**
00035025005	53879	2.30	1.90±0.01	1.960±0.006	2.19±0.02	28.2±0.4	26758	804.9/328	384.1/327
00035025006	53880	4.38	1.95±0.008	1.957±0.005	2.22±0.01	23.1±0.3	44306	1211.8/401	483.8/400
00035025007	53881	4.37	1.975±0.008	1.865±0.004	2.23±0.01	22.3±0.3	43562	1119.9/396	480.4/397
00035025008	53882	4.28	2.078±0.008	2.147±0.005	2.43±0.02	17.0±0.2	36841	1430.8/343	458.0/342
00035025009	53883	4.41	2.067±0.008	2.117±0.005	2.41±0.02	17.3±0.2	35858	1265.9/344	429.3/343
00035025010	53884	3.28	2.12±0.01	2.001±0.006	2.44±0.02	15.4±0.2	26439	914.7/244	383.6/243
00035025016	54434	1.28	2.07±0.06	3.192±0.058	2.5±0.1	17.8±1.6	1268	56.0/37	40.2/36

Continued on next page

Table 3.4 – *Continued from previous page*

Observation ID	**Date** [MJD]	**Exposure** [ks]	**Fixed PL** α	**PL** $N_{HI}^{MW}+N_{HI}^{INT}$ $[\times 10^{21}\mathbf{cm}^{-2}]$	**Free PL** α	**2-10 keV Flux** $\times 10^{-11}$ [ergs $\mathbf{cm}^{-2}\mathbf{s}^{-1}$]	**Spectral Counts**	**Fixed PL** χ^2/dof	**Free PL** χ^2/dof
00035025027	54989	0.99	2.26±0.02	1.899±0.011	2.56±0.04	10.5±0.3	6399	267.0/150	165.9/149
00035025028	54996	1.0	2.33±0.03	1.542±0.011	2.52±0.05	8.18±0.4	4749	147.1/120	116.3/119
00035025032	55010	1.55	2.17±0.02	1.587±0.008	2.36±0.03	12.8±0.2	9745	239.2/195	166.1/194
00035025034	55016	1.64	2.11±0.02	1.693±0.008	2.32±0.03	16.8±6.1	12162	329.9/219	210.1/218
00035025037	55038	0.60	2.28±0.03	1.762±0.015	2.56±0.06	8.91±0.3	3331	126.2/84	87.6/83
00035025038	55045	0.65	2.19±0.03	1.927±0.014	2.46±0.05	12.3±0.5	4687	179.2/120	116.6/119
00035025041	55066	1.20	2.17±0.02	1.439±0.011	2.31±0.04	9.88±0.4	5488	144.4/139	124.3/138
00035025042	55070	1.23	2.15±0.02	1.989±0.011	2.48±0.04	11.6±0.4	7914	330.5/175	177.0/174
00035025043	55087	0.96	2.27±0.03	1.575±0.011	2.47±0.05	78.1±0.3	4693	140.4/120	106.1/119
00035025044	55100	6.12	2.256±0.009	1.646±0.004	2.47±0.02	80.6±0.1	30252	619.9/303	320.2/302
00035025045	55318	1.29	2.07±0.02	1.606±0.012	2.24±0.04	80.6±0.1	4836	180.6/122	151.3/121
00035025046	55323	1.09	2.03±0.02	1.584±0.012	2.18±0.04	13.2±2.4	6433	163.0/159	129.2/158
00035025047	55332	1.02	2.07±0.02	1.333±0.011	2.17±0.04	11.2±0.3	5188	124.0/132	113.9/131
00035025048	55346	1.12	2.07±0.03	1.622±0.014	2.24±0.04	9.94±0.4	5081	122.1/130	94.3/129
00035025049	55353	1.08	2.05±0.03	2.152±0.020	2.32±0.05	7.83±0.3	4252	154.0/107	95.8/106
00035025050	55360	1.07	2.13±0.03	2.548±0.023	2.52±0.06	7.37±0.3	4026	206.2/100	98.5/99
00035025051	55367	1.01	2.16±0.03	1.967±0.020	2.43±0.06	5.68±0.2	3326	103.1/82	62.8/81

Continued on next page

Table 3.4 – *Continued from previous page*

Observation ID	**Date** [MJD]	**Exposure** [ks]	**Fixed PL** α	**PL** $N_{HI}^{MW}+N_{HI}^{INT}$ [$\times 10^{21}$ cm^{-2}]	**Free PL** α	**2-10 keV Flux** $\times 10^{-11}$ [ergs cm^{-2}s^{-1}]	**Spectral Counts**	**Fixed PL** χ^2/dof	**Free PL** χ^2/dof
00035025052	55375	1.16	2.16±0.03	1.536±0.014	2.32±0.05	7.77±0.3	4708	182.2/121	161.2/120
00035025053	55381	1.16	2.03±0.02	2.046±0.017	2.29±0.05	9.76±0.3	5703	227.1/145	165.2/144
00035025054	55396	1.11	2.14±0.03	2.019±0.016	2.41±0.05	7.64±0.3	4644	167.6/118	104.7/117
00035025056	55404	0.77	2.23±0.03	1.710±0.017	2.44±0.06	8.48±0.4	3273	129.5/83	104.9/82
00035025057	55409	1.02	2.34±0.03	1.961±0.016	2.68±0.06	4.94±0.2	3628	137.1/93	73.6/92
00035025058	55458	1.26	2.17±0.02	1.921±0.012	2.46±0.04	8.69±0.4	6132	242.4/147	143.1/146
00035025059	55463	1.24	2.01±0.02	1.798±0.010	2.24±0.03	15.7±0.4	9237	313.8/193	205.7/192
00035025062	55686	1.19	2.50±0.03	1.483±0.012	2.69±0.05	3.36±0.2	3247	115.0/81	92.8/80
00035025063	55693	1.25	2.48±0.04	1.630±0.018	2.70±0.07	2.43±0.1	2438	91.4/66	72.9/65
00035025064	55700	0.94	2.31±0.03	1.689±0.018	2.50±0.06	5.59±0.2	3361	109.9/83	90.6/82
00035025066	55714	0.95	2.09±0.03	2.111±0.022	2.35±0.06	7.68±0.3	3804	127.1/94	88.2/93
00035025067	55721	0.98	2.22±0.03	2.060±0.018	2.53±0.06	7.58±0.3	3625	151.6/93	94.7/92
00035025068	55728	1.0	2.28±0.04	1.632±0.027	2.46±0.09	3.35±0.2	2001	63.2/53	54.9/52
00035025069	55735	1.17	2.29±0.04	1.968±0.032	2.54±0.09	2.74±0.2	2073	71.3/56	54.6/55
00035025071	55749	1.00	2.36±0.06	1.255±0.026	2.4±0.1	2.12±0.2	1442	39.5/40	38.5/39
00035025072	55763	1.05	2.32±0.04	2.696±0.034	2.77±0.09	3.01±0.2	2364	127.8/63	74.1/62
00035025074	55814	1.41	2.10±0.02	2.276±0.012	2.42±0.03	33.9±0.9	11257	442.4/216	233.1/215

Continued on next page

Table 3.4 – *Continued from previous page*

Observation ID	**Date** [MJD]	**Exposure** [ks]	**Fixed PL** α	**PL** $N_{HI}^{MW}+N_{HI}^{INT}$ [$\times10^{21}$cm^{-2}]	**Free PL** α	**2-10 keV Flux** $\times10^{-11}$ [ergs cm^{-2}s^{-1}]	**Spectral Counts**	**Fixed PL** χ^2/dof	**Free PL** χ^2/dof
00035025075	56036	0.98	2.44±0.03	1.652±0.012	2.67±0.05	9.97±0.3	5504	156.7/130	112.4/129
00035025076	56037	1.52	2.36±0.02	1.678±0.007	2.60±0.03	10.8±0.2	11140	337.4/195	220.7/194
00035025077	56051	0.99	2.34±0.02	1.592±0.012	2.52±0.04	9.23±0.2	6044	154.6/142	117.5/141
00035025078	56064	1.06	2.24±0.02	1.525±0.011	2.41±0.04	10.8±0.3	5500	161.6/135	130.2/134
00035025079	56067	0.69	2.23±0.03	1.574±0.018	2.38±0.06	9.79±0.3	3841	116.6/94	103.4/93
00035025080	56074	1.27	2.10±0.02	2.150±0.013	2.40±0.05	13.1±0.3	9006	370.5/187	232.1/186
00035025081	56075	1.10	2.28±0.02	1.631±0.012	2.48±0.04	7.59±0.3	5230	145.3/127	108.2/126
00035025082	56076	0.92	2.40±0.03	1.643±0.018	2.60±0.06	4.77±0.3	3207	105.4/82	85.2/81
00035025083	56078	1.04	2.15±0.02	1.966±0.014	2.42±0.04	10.9±0.4	6148	214.9/147	138.3/146
00035025084	56079	1.52	2.37±0.02	1.759±0.014	2.44±0.04	9.75±0.3	7082	210.1/161	167.7/160
00035025085	56094	0.99	2.40±0.03	1.488±0.012	2.57±0.05	7.32±0.3	4448	155.1/113	135.8/112
00035025086	56107	1.01	2.09±0.02	1.722±0.012	2.28±0.04	16.7±0.5	6083	212.7/155	159.3/154
00035025087	56128	1.01	2.16±0.03	1.590±0.016	2.32±0.05	13.2±0.5	3916	84.0/97	66.3/96
00035025088	56135	1.18	2.27±0.03	1.927±0.017	2.54±0.05	8.65±0.3	4892	153.7/126	103.1/125
00035025089	56179	0.93	2.48±0.03	1.167±0.011	2.53±0.05	4.74±0.3	3142	98.2/77	96.1/76
00035025091	56196	1.52	2.38±0.03	1.721±0.017	2.59±0.06	4.01±0.2	3934	119.7/99	91.8/98

Table 3.5: Summary of LP spectral analysis for 1ES 1959+650. Observation ID details given in Table 3.3. The Galactic N_{HI} column density was fixed to $1\times10^{21}cm^{-2}$, as measured by Kalberla et al. (2005) with a ∼3% error. Observation ID 00035025004 is shown in bold and represents the best fit values for the models shown in the bottom panel of Figure 3.1.

Observation ID	**Fixed LP** α	**Fixed LP** β	**Free LP** N_{HI} $[\times10^{22}cm^{-2}]$	**Free LP** α	**Free LP** β	**Spectral Counts**	**Fixed LP** χ^2**/dof**	**Free LP** χ^2**/dof**
00035025001	1.83±0.02	0.68±0.03	0.15±0.01	2.16±0.07	0.29±0.086	32782	390.1/329	363.8/328
00035025002	1.73±0.03	0.69±0.06	0.18±0.03	2.2±0.1	0.1±0.2	9270	239.7/191	222.1/190
00035025003	1.69±0.03	0.62±0.05	0.14±0.02	1.9±0.1	0.4±0.1	14911	274.6/250	264.1/249
00035025004	**1.51±0.03**	**0.42±0.03**	**0.17±0.01**	**2.09±0.06**	**0.06±0.07**	**44642**	**537.6/416**	**481.1/415**
00035025005	1.59±0.02	0.63±0.04	0.17±0.01	1.98±0.08	0.21±0.09	26758	403.5/327	378.9/326
00035025006	1.67±0.02	0.62±0.03	0.19±0.01	2.16±0.06	0.07±0.07	44306	553.6/400	482.8/399
00035025007	1.72±0.03	0.57±0.03	0.18±0.01	2.19±0.06	0.04±0.07	43562	549.0/395	480.1/394
00035025008	1.74±0.02	0.79±0.03	0.19±0.01	2.29±0.07	0.17±0.08	36841	519.9/342	453.9/341
00035025009	1.75±0.02	0.75±0.03	0.20±0.01	2.36±0.07	0.06±0.08	35858	503.1/343	428.8/342
00035025010	1.83±0.02	0.71±0.04	0.19±0.01	2.36±0.08	0.1±0.1	26439	422.8/243	382.7/242
00035025016	1.5±0.2	1.2±0.3	0.1±0.2	1.48±0.9	1.15±1.0	1268	38.8/36	38.8/35
00035025027	2.00±0.04	0.67±0.08	0.16±0.03	2.4±0.2	0.2±0.2	6399	169.2/149	164.7/148

Continued on next page

Table 3.5 – *Continued from previous page*

Observation ID	**Fixed LP** α	**Fixed LP** β	**Free LP N$_{\rm HI}$** [$\times 10^{22}$**cm**$^{-2}$]	**Free LP** α	**Free LP** β	**Spectral Counts**	**Fixed LP** χ^2**/dof**	**Free LP** χ^2**/dof**
00035025028	2.18±0.04	0.39±0.08	0.17±0.03	2.6±0.2	-0.1±0.2	4749	121.6/119	116.0/118
00035025032	1.99±0.03	0.42±0.06	0.15±0.02	2.3±0.1	0.1±0.2	9745	172.0/194	165.9/193
00035025034	1.89±0.03	0.48±0.05	0.15±0.02	2.2±0.1	0.1±0.1	12162	217.0/218	208.9/217
00035025037	2.09±0.05	0.57±0.1	0.20±0.04	2.7±0.3	-0.2±0.3	3331	92.6/83	87.3/82
00035025038	1.91±0.05	0.63±0.09	0.15±0.04	2.2±0.2	0.3±0.2	4687	117.2/119	115.1/118
00035025041	2.05±0.04	0.27±0.08	0.17±0.03	2.5±0.2	-0.2±0.2	5488	129.6/138	123.3/137
00035025042	1.88±0.04	0.67±0.07	0.20±0.03	2.5±0.2	-0.01±0.2	7914	194.2/174	177.0/173
00035025043	2.10±0.04	0.45±0.09	0.13±0.03	2.3±0.2	0.2±0.2	4693	106.2/119	105.2/118
00035025044	2.05±0.02	0.51±0.03	0.11±0.01	2.12±0.07	0.43±0.08	30252	296.1/302	295.1/301
00035025045	1.85±0.05	0.47±0.08	0.07±0.03	1.7±0.2	0.64±0.2	4836	143.3/121	142.5/120
00035025046	1.84±0.04	0.38±0.07	0.14±0.03	2.1±0.2	0.1±0.2	6433	130.7/158	128.6/157
00035025047	1.91±0.05	0.323±0.08	0.05±0.02	1.6±0.2	0.7±0.2	5188	105.8/131	101.6/130
00035025048	1.87±0.05	0.42±0.09	0.14±0.03	2.1±0.2	0.2±0.2	5081	95.0/129	93.7/128
00035025049	1.68±0.06	0.69±0.1	0.13±0.04	1.9±0.2	0.5±0.2	4252	92.5/106	91.7/105
00035025050	1.67±0.07	0.93±0.1	0.19±0.05	2.2±0.3	0.4±0.3	4026	101.5/99	96.3/98
00035025051	1.88±0.07	0.63±0.1	0.17±0.05	2.3±0.3	0.2±0.3	3326	65.3/81	62.5/80
00035025052	2.00±0.05	0.34±0.09	0.16±0.03	2.4±0.2	0.0±0.2	4708	165.1/120	161.1/119

Continued on next page

Table 3.5 – *Continued from previous page*

Observation ID	**Fixed LP** α	**Fixed LP** β	**Free LP N$_{\rm HI}$** [$\times 10^{22}$**cm**$^{-2}$]	**Free LP** α	**Free LP** β	**Spectral Counts**	**Fixed LP** χ^2**/dof**	**Free LP** χ^2**/dof**
00035025053	1.68±0.06	0.68±0.09	0.11±0.03	1.8±0.2	0.6±0.2	5703	158.3/143	158.1/142
00035025054	1.81±0.06	0.7±0.1	0.13±0.04	2.0±0.2	0.5±0.2	4644	101.0/117	100.2/116
00035025056	2.00±0.06	0.5±0.1	0.14±0.04	2.2±0.3	0.2±0.3	3273	105.4/82	104.5/81
00035025057	2.09±0.06	0.7±0.1	0.18±0.04	2.6±0.3	0.1±0.3	3628	78.1/92	73.6/91
00035025058	1.90±0.04	0.66±0.08	0.16±0.03	2.3±0.2	0.2±0.2	6132	146.8/146	141.7/145
00035025059	1.76±0.04	0.55±0.06	0.15±0.02	2.1±0.1	0.2±0.2	9237	210.1/192	204.2/191
00035025062	2.34±0.05	0.5±0.1	0.07±0.03	2.1±0.2	0.7±0.3	3247	87.5/80	86.7/79
00035025063	2.30±0.07	0.5±0.1	0.16±0.05	2.7±0.3	0.1±0.4	2438	74.4/65	72.8/64
00035025064	2.06±0.07	0.5±0.1	0.07±0.03	1.9±0.2	0.7±0.3	3361	84.7/82	84.1/81
00035025066	1.75±0.07	0.7±0.1	0.14±0.05	2.0±0.2	0.4±0.3	3804	86.8/93	86.0/92
00035025067	1.88±0.06	0.8±0.1	0.10±0.04	1.9±0.2	0.8±0.3	3625	88.3/92	88.3/91
00035025068	2.09±0.09	0.4±0.2	0.16±0.07	2.4±0.4	0±0.5	2001	55.8/52	54.9/51
00035025069	2.0±0.1	0.6±0.2	0.23±0.09	2.7±0.4	-0.2±0.5	2073	58.0/55	54.4/54
00035025071	2.3±0.1	0.2±0.2	0.12±0.07	2.4±0.4	0.1±0.6	1442	38.5/39	38.5/38
00035025072	1.9±0.1	1.0±0.2	0.24±0.09	2.6±0.4	0.2±0.5	2364	78.2/62	74.0/61
00035025074	1.68±0.04	0.83±0.07	0.11±0.02	1.8±0.1	0.7±0.1	11257	209.2/215	208.9/214
00035025075	2.25±0.04	0.53±0.09	0.13±0.03	2.4±0.2	0.3±0.3	5504	111.8/129	110.9/128

Continued on next page

Table 3.5 – *Continued from previous page*

Observation ID	**Fixed LP** α	**Fixed LP** β	**Free LP N$_{\rm HI}$** [$\times 10^{22}$**cm**$^{-2}$]	**Free LP** α	**Free LP** β	**Spectral Counts**	**Fixed LP** χ^2**/dof**	**Free LP** χ^2**/dof**
00035025076	2.16±0.03	0.54±0.05	0.11±0.02	2.2±0.1	0.5±0.1	11140	211.7/194	211.4/193
00035025077	2.16±0.04	0.41±0.08	0.15±0.03	2.4±0.2	0.1±0.2	6044	120.4/141	117.3/140
00035025078	2.1±0.2	0.4±0.2	0.11±0.03	2.1±0.2	0.4±0.2	5500	127.1/134	127.1/133
00035025079	2.02±0.07	0.4±0.1	0.09±0.04	1.9±0.2	0.5±0.3	3841	100.2/93	100.1/92
00035025080	1.75±0.04	0.76±0.07	0.13±0.03	1.9±0.2	0.6±0.2	9006	223.6/186	222.4/185
00035025081	2.07±0.05	0.51±0.08	0.08±0.03	1.9±0.2	0.7±0.2	5230	100.1/126	97.6/125
00035025082	2.20±0.07	0.5±0.1	0.13±0.04	2.4±0.3	0.2±0.3	3207	85.4/80	84.6/79
00035025083	1.85±0.05	0.65±0.09	0.15±0.03	2.1±0.2	0.3±0.2	6148	138.5/146	135.9/145
00035025084	1.98±0.05	0.53±0.08	0.10±0.03	2.0±0.2	0.5±0.2	7082	161.6/160	161.6/159
00035025085	2.24±0.05	0.4±0.1	0.10±0.03	2.2±0.2	0.4±0.3	4448	133.4/112	133.4/111
00035025086	1.81±0.04	0.55±0.08	0.08±0.02	1.7±0.2	0.7±0.2	6083	146.2/154	145.6/153
00035025087	1.96±0.06	0.4±0.1	0.11±0.03	2.1±0.2	0.3±0.2	3916	65.3/96	65.0/95
00035025088	2.00±0.06	0.6±0.1	0.16±0.04	2.4±0.2	0.2±0.3	4892	105.2/125	102.4/124
00035025089	2.39±0.05	0.2±0.1	0.03±0.03	1.9±0.2	0.8±0.3	3142	92.9/76	88.4/75
00035025091	2.13±0.06	0.6±0.1	0.10±0.04	2.2±0.2	0.5±0.3	3934	89.5/98	89.5/97

3.4 Discussion and Conclusion

The 0.3-10 keV spectral analysis of the three blazars which have molecular CO line luminosity measurements and upper limits support a possible connection between blazar CO line luminosity and hydrogen column density, providing a possible method to directly probe the relativistic particle energy distribution. The two sources RGB J0710+591 and W Comae, both of which are shown to exhibit no CO line luminosity to the limits probed in Fumagalli et al. (2012), also lack evidence for X-ray absorption by intrinsic gas and could be sufficiently described with an uncurved power-law.

The blazar 1ES 1959+650 shows significant curvature when fit with a LP model. The LP fit qualities are comparable to those found when an intrinsic column density is included for the PL model. The blazar has been shown to contain a significant level of molecular CO. Relying on the connection between molecular CO and hydrogen column density form PDR, the corresponding column density is $\sim 1 \times 10^{21}\mathrm{cm}^{-2}$, or more, is in agreement with the typical value of $0.8 \times 10^{21}\mathrm{cm}^{-2}$ we obtain in the fits to the X-ray spectra. We have therefore broken the degeneracy between the LP and the $\mathrm{N_{HI}^{INT}}$-inclusive PL models, concluding that this source is likely to be exhibiting an intrinsically uncurved X-ray spectrum with intrinsic gas leading to the observed spectra.

We note that in the LP spectral analysis of RGB J0710+591 and W Comae,

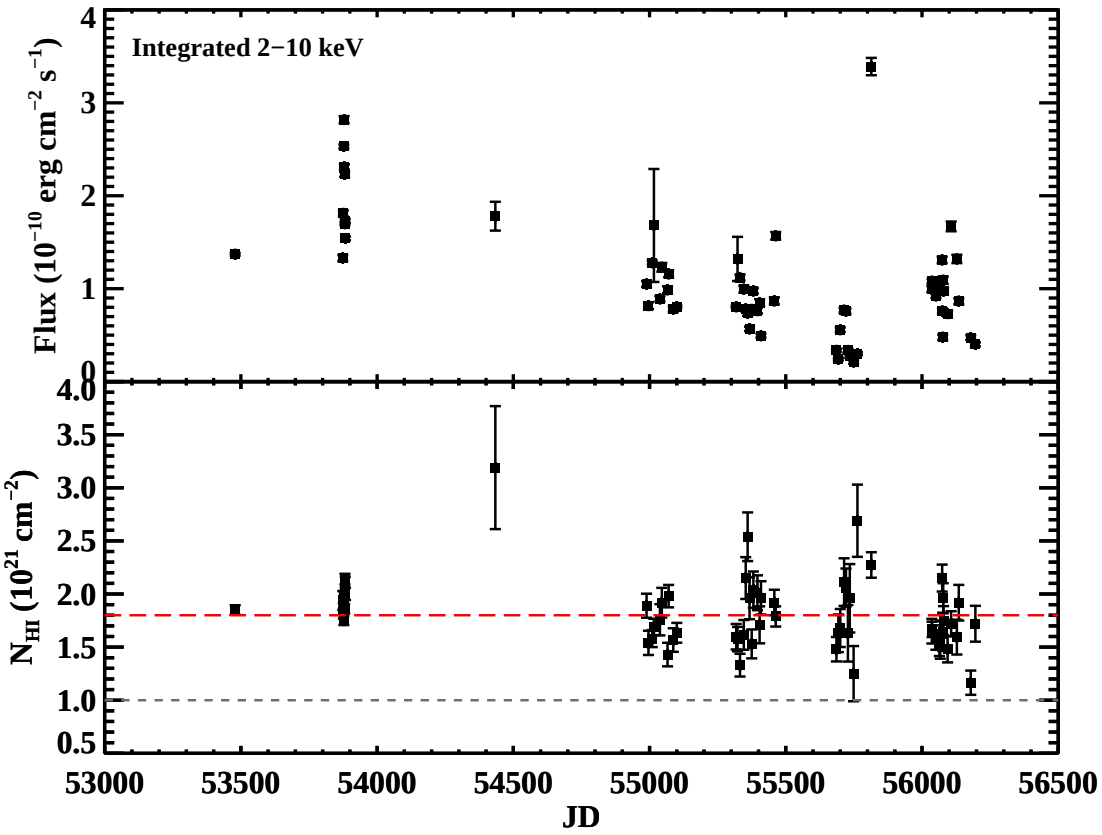

Figure 3.5: A light curve of the 2−10 keV flux and fitted N_{HI}^{INT} column density for the 61 windowed timing observations of 1ES 1959+650. The flux is seen to vary widely, with a fit to a constant resulting in a χ^2 of 35089 for 61 degrees of freedom. The N_{HI}^{INT} column density is also variable, but shows a smaller χ^2 value of 320 when fit with a constant, with an average of 0.8×10^{21}cm^{-2} (denoted by the red dashed line), nearly equal to the value N_{HI}^{MW} of 1.0×10^{21}cm^{-2} as reported by the LAB survey (denoted by the grey dotted line). This additional 0.8×10^{21}cm^{-2} column density beyond that of the LAB value is in significant excess of the 1-2% error reported for the LAB survey measurements. The slight variability of the N_{HI}^{INT} column density is not immediately expected and, if real, suggests that the column density is very close to the non-thermal emission region. However, the errors shown here do not account for slight correlations between other fitted PL parameters.

instances of significantly negative spectral curvature result from a covariance relation between the α and β parameters. Additional investigation to this relation is beyond the scope of this paper. However, future application of the LP model to similar X-ray spectra might result in more physical models if completed with a limit to positive curvature ($\beta > 0$) within the LP model framework, as convex spectra are difficult to produce under traditional non-thermal emission scenarios, although not impossible.

The uncurved X-ray spectra found for these sources suggest that the particle population responsible for the synchrotron emission is similarly uncurved, supporting a non-statistical (energy-independent) acceleration process at work within the blazar. The information about the shape of the particle energy distribution can be put to use in broadband models of non-thermal emission from TeV-blazars, which require the input of the population distribution shape and slope. If the relation between CO line luminosity and the evidence for intrinsic X-ray absorption holds for other blazars, similar observations can be used to place previously unavailable model constraints on other X-ray bright blazars. By extension, the use of X-ray spectral analysis in search of evidence for additional intrinsic absorption can provide a hint as to how bright the CO line luminosity for certain blazars might be.

The apparent lack of intrinsic gas in the blazar RGB J0710+591 also supports

past broadband modeling of the non-thermal emission, which shows acceptable representation from a SSC emission scenario, indicating a clean emission environment (Acciari, et al. , 2010) Similar modeling for W Comae, however, shows a preference for an EC emission scenario, relying on an external photon field which might arise from intrinsic gas (Acciari et al., 2009c). The lack of intrinsic gas and acceptable SSC modeling is in agreement with the blazar evolutionary theory for the HSP RGB J0710+591, but the lack of evidence for intrinsic gas within W Comae is in contradiction to what the blazar evolution would imply for the emission environment of the ISP.

The evidence for intrinsic gas within the HSP 1ES 1959+650 is also contrary to the blazar evolutionary theory, which predicts a clean emission environment for the blazar. This result does, however, agree with the previously detected variability patterns displayed by this blazar which are not easily supported by clean SSC emission scenarios (e. g. an "orphan" flare event, reported in Krawczynski et al. (2006)). Moreover, this variability pattern has been described by the presence of intrinsic dilute gas (Böttcher, 2005), as suggested by the independent molecular CO measurements and the N_{HI}^{INT} inferred from soft X-ray absorption. Other observations (e. g. Meyer et al. (2011); Krawczynski et al. (2006)) have also found evidence contradictory to the current blazar evolutionary theory.

In addition, we note that the presence of an intrinsic column density com-

parable to the Galactic column density ($\sim 1 \times 10^{21} \mathrm{cm}^{-2}$) for 1ES 1959+650 would introduce more than one magnitude of extinction for $\lambda < 3000$ Å (assuming standard gas-to-dust ratio and Milky Way extinction law). Non-thermal UV emission (e. g. as seen in Tramacere et al. (2007)) is suppressed by additional column density, deforming the observed SED from that which is emitted. Evidence for intrinsic column density within the blazar environment would support the use of an additional extinction-correction to the observed UV flux values beyond that required by the Milky Way to more accurately represent the intrinsically emitted SED.

In summary, the evidence for intrinsic gas in the HSP 1ES 1959+650 and the lack of it in the ISP W Comae do not directly align with the blazar evolutionary paradigm. However, the millimetric and X-ray observations for these sources do support a possible connection between the existence of molecular CO and intrinsic gas, maintaining the possibility for a rare opportunity to collect experimental insight into the emission environment and mechanism at work within blazar jets.

Chapter 4

Investigating a Mirrored Emission Scenario for Broadband Observations of the TeV Blazar 1ES 1959+650

This work is in preparation for submission to the Astrophysical Journalf. The corresponding author of the work is Amy Furniss.

Abstract

We summarize broadband observations of the TeV-emitting blazar 1ES 1959+650, including optical R-band observations by the robotic telescopes Super-LOTIS and iTelescope, UV observations by Swift UVOT, X-ray observations by the Swift X-ray Telescope (XRT), high-energy gamma rays with the Fermi Large Area Telescope and very-high-energy (VHE) observations by VERITAS above 315 GeV between 16 April 2012 and 1 June 2012 (MJD 56033 and 56080). The contemporaneous variability is explored in the context of a reflected emission scenario, motivated by recent evidence for gas within the blazar. The emission model applied here is not required to describe the observed variability pattern, but represents one possible scenario which can describe the observations. As applied to two elevated VHE states observed during the monitoring period, the mirrored emission scenario does not support a purely leptonic non-thermal emission mechanism. The reflected emission model does, however, predict a reflected photon field with sufficient energy to enable pion production with protons of energies between 10 and 100 TeV.

4.1 Introduction

1ES 1959+650, a blazar at z=0.047 (Scatcher et al., 1993) is one of the first detected extragalactic very-high-energy (VHE; E≥100 GeV) emitters (Holder et al., 2003). A blazar is a type of active galactic nucleus (AGN) having a relativistic jet which is pointed close to the line of sight of the observer. The non-thermal radiation from blazars, thought to originate from within the jet, produces a double-humped spectral energy distribution (SED).

The lower-energy peak of the SED, referred to as the synchrotron peak, results from the synchrotron radiation of relativistic leptons in the presence of a tangled magnetic field. The higher-energy peak, referred to here as the gamma-ray peak, can be attributed to inverse-Compton up-scattering by the relativistic particles within the jet of either the synchrotron photons themselves (namely synchrotron self-Compton emission; SSC) or a photon field external to the jet (namely external Compton emission; EC) as described in Dermer et al. (1992), Maraschi et al. (1992), Marscher & Protheroe (2000) and Sikora et al. (1994). Hadronic processes initiated by relativistic protons such as pion production and the resulting cascade emission can similarly produce the higher energy peak (Aharonian et al., 2002; Bednarek, 1993; Dar et al., 1997; Mannheim, 2000; Mücke & Protheroe, 2000; Pohl & Schlickeiser, 2000).

The non-thermal emission resulting from these different processes can produce

nearly indistinguishable time-averaged SEDs, as discussed in Tagliaferri et al. (2008), making emission-model discrimination based on non-simultaneous data uncertain. An effective means to investigate a blazar emission mechanism is through the observation and subsequent modeling of broadband spectral variability (Böttcher, 2007). Correlated variability between the lower and higher-energy SED peaks, for example, can be well described by a simple SSC model, whereas less common, non-correlated variability patterns, similar to the "orphan" flaring events observed from 1ES 1959+650 (Krawczynski et al., 2006), require more complex emission scenarios. This type of non-correlated variability has been described using multiple zone SSC (Graff et al., 2008), EC (Kusunose & Takahara, 2006) and mirrored emission scenarios (Böttcher, 2005).

A mirrored emission scenario requires the non-thermal emission region to have a dilute gas in close proximity. This gas could reflect synchrotron emission from an elevated state back to the non-thermal emission region, providing an external photon field to be up-scattered. If the elevated state was short-lived with respect to the light crossing timescale between the emission region and the reflector, the broadband variability pattern resulting from such an emission geometry would be displayed as a primary elevated state, observed in both the synchrotron and gamma-ray peaks of the SED, followed some time later by a secondary flare of the gamma-ray peak alone. The time delay between these two elevated states would

depend on the distance between the emission region and the dilute reflector.

The collection of definite observational evidence of a primary and secondary flare to which the mirrored emission model applies is challenging because of the unavoidably sparse sampling of multiwavelength campaigns. This is especially true due to the unknown separation between the two flaring episodes. Recently, however, evidence from millimeter (Fumagalli et al., 2012) and X-ray observations (Furniss et al., 2013c) of 1ES 1959+650 support the existence of intervening gas within the blazar and, therefore, the application of a mirrored emission scenario to the broadband variability. More specifically, 1ES 1959+650 shows evidence for absorption of X-rays by gas in the host and contains a significant level of molecular CO.

In this work we summarize broadband variability of 1ES 1959+650 detected during multiwavelength observations between 17 April 2012 and 1 June 2012 (MJD 56034 and 56080). These observations include 0.7 ks of strictly simultaneous VERITAS and *Swift* observations on MJD 56067, occurring at the beginning of a VHE flare lasting approximately two hours. Motivated by the recent evidence for intervening gas within 1ES 1959+650, we investigate a possible explanation of the broadband variability through the application of a mirrored emission scenario. We summarize the observations and results of the multiwavelength observations in Sections 2 and 3, respectively. The model is applied to the data in Section 4,

with the implications discussed in Section 5.

4.2 Broadband Observations

4.2.1 VERITAS

VERITAS is an array of four imaging atmospheric Cherenkov telescopes in southern Arizona, each with a 3.5° field of view. The array is sensitive to photons with energies between ∼100 GeV and more than 10 TeV and can significantly detect a 1% Crab Nebula-type source[1] in less than 28 hours. The telescope array uses the 12-meter reflectors to focus dim, blue Cherenkov light resulting from gamma and cosmic ray interactions in the atmosphere onto cameras composed of 499 photomultiplier tubes (PMTs). More details on the VERITAS instrument specifications can be found in Holder et al. (2006) and Weekes et al. (2002).

A historically high optical state of 1ES 1959+650, as measured by the Super-LOTIS robotic telescope, prompted near nightly VERITAS exposures over two dark runs[2] between 17 April and 1 June 2012 (MJD 56034-56080). These observations were taken in *wobble* mode, with exposures taken at 0.5° offset in each of four cardinal directions from 1ES 1959+650 in order to facilitate simultaneous background measurements (Fomin et al., 1994; Berge et al., 2007). The total

[1]The Crab Nebula is a bright VHE source, roughly characterized with a power-law index of Γ=2.5 in the VHE band, where $dN/dE = (E/E_0)^{-\Gamma}$.

[2]A dark run is the period between two full moons.

exposure over two dark runs resulted in 8.7 hours of quality-selected live-time, collected at an average zenith angle of 37°.

Elliptical moments of the recorded events are calculated and used to discriminate background cosmic-ray events from gamma-ray events. The data are first cleaned with "quality cuts": any telescope event involving less than five PMTs or having a center at greater than 1.43 degrees from the camera center is discarded. Additionally, the events are required to have a total "size" of more than 80 photoelectrons. The size parameter is a measure of how much Cherenkov light is collected by the camera.

Single telescope event widths and lengths are combined into mean-scaled-width (MSW) and mean-scaled-length (MSL) parameters for each array event, as described in Cogan (2008) and Daniel (2008). Only array events with $0.5 <$ MSW <1.25, $0.5 <$ MSL <1.1, a reconstructed height of shower maximum greater than 7 km above the array and having a reconstruction direction within 0.1 degrees of 1ES 1959+650 are kept as ON candidate signal events. The background OFF events are those events passing all aforementioned cuts and falling within 0.1°-radius circular regions at the same radial distance as the source from the center of the camera. The source significance is calculated from the number of events falling in these ON and OFF regions according to Equation 17 of Li & Ma (1983). The spectral analysis of the VHE source signal is confirmed with two independent

analysis packages.

The total VERITAS exposure between 17 April and 1 June 2012 (MJD 56034 to 56080) resulted in 752 ON events and 1820 OFF events with an overall detection significance of 31 standard deviations (σ), as calculated by Equation [17] from Li & Ma (1983). Variability was observed during these observations, as can be seen in the top panel of the broadband light curve presented in Figure 4.1. Additionally, Table 4.1 contains a summary of the VHE analysis and spectral state of 1ES 1959+650 during the two dark runs (MJD 56034-56040 and 56064-56079) and the two separate days (MJD 56062 and 56067) where an elevated VHE state is detected. These two flaring periods are excluded from the dark run analysis results.

The hour-scale exposures during the first dark run show the blazar to be at an average flux of 8.6±3.6 $\times 10^{-7}$ photons $\mathrm{cm}^{-2}\mathrm{s}^{-1}$ (approximately 10% of the Crab Nebula flux). These first dark run observations are paired with two contemporaneous *Swift* exposures. VERITAS observations during the following dark run begin with the detection of an elevated state on 15 May 2012 (MJD 56062). The 28 minute VERITAS exposure show a flux of 3.8±2.1 $\times 10^{-6}$ photons $\mathrm{cm}^{-2}\mathrm{s}^{-1}$ (corresponding to approximately 30% of the Crab Nebula flux). No *Swift* observations are available for this day.

Five days after the observation of the 30% Crab state, on MJD 56067, VER-

ITAS detected a VHE flare from 1ES 1959+650.The VERITAS observations on MJD 56067 show the blazar rise from ∼50% to 120% of the Crab Nebula in less than 30 minutes (see top panel of Figure 4.2). This rise in flux was followed by a steady decay, dropping back to ∼ 40% of the Crab approximately 90 minutes after the start of the event. The blazar has less than 0.2% probability of exhibiting a constant flux on MJD 56067 ($\chi^2 = 29.5$ with 11 degrees of freedom). The first 0.7 ks of the VERITAS observations of the flaring event were matched with simultaneous *Swift* observations, described in Section 3.3. VERITAS continued to observe 1ES 1959+650 through 1 June 2012, detecting the source at an average of 10% Crab flux ($1.2\pm3.6 \times 10^{-7}$ photons cm^{-2}s^{-1} above 315 GeV).

4.2.2 *Fermi* Large Area Telescope

The *Fermi* Large Area Telescope (LAT) is a space-based telescope that typically monitors the entire high-energy gamma-ray sky from below 30 MeV to ∼300 GeV every three hours (Atwood et al., 2009). The instrument has better than 10% energy resolution with an angular resolution of better than 0.15° for energies greater than 10 GeV. The public *Fermi* data contemporaneous with the second dark run of VERITAS observations (MJD 56062 to 56068) were downloaded and analyzed with the `FermiTools v9r27p1` in order to search for evidence of an elevated gamma-ray flux..

Table 4.1: Summary of VERITAS observations

	Exposure Date MJD	**Exposure Livetime [minutes]**	**Detection Significance** σ	**Number ON Events**	**Number OFF Events**	**Power law Index** Γ	**Average Integral Flux** $\geq$ **315 GeV** $\times 10^{-6}$ [**ph cm**$^{-2}$**s**$^{-1}$]	**Integral Flux Percent Crab** [%]
April Dark Run	56034-56040	186	6.6	90	425	2.5±0.4	0.9±0.4	10
Primary Flare	56062	28	6.1	27	60	2.1±0.7	3.8±2.1	30
Secondary Flare	56067	106	26	276	249	2.48±0.09	8.0±0.8	70
May Dark Run	56064-56079	203	9.7	121	441	2.0±0.6	1.1±0.2	10
Both Dark Runs	56034-56079	389	11.8	214	866	2.9±0.2	1.2±0.3	10

Events were extracted from a 30° radius region centered on the 1ES 1959+650 coordinates for the period which contains two elevated states as observed by VERITAS. "Diffuse class" events with a zenith angle of $< 100°$ and energy between 300 MeV to 300 GeV were selected. In order to reduce contamination from Earth limb gamma rays, only data taken during time when the rocking angle of the satellite was less than 52° were used. The significance and spectral parameters were calculated using the unbinned maximum-likelihood method *gtlike* with the `P7SOURCE_V6` instrument response function. The background model was constructed to include nearby ($< 35°$ away) gamma-ray sources from the second *Fermi* LAT catalog (2FGL, Nolan et al. (2012)) as well as diffuse emission.

As in the 2FGL catalog, a log-parabolic function was used for nearby sources with significant spectral curvature and a power law for those sources without spectral curvature. The spectral parameters of sources within 7° of 1ES 1959+650 were left free during fitting, while those outside of this range were held fixed to the 2FGL catalog values. The Galactic diffuse emission was modeled with the file `gal_2yearp7v6_v0.fits` and the isotropic emission component was modeled with the file `iso_p7v6source.txt`.[3]

The detection resulting from a full dark run of contemporaneous data results in a test statistic (TS; Mattox et al. (1996)) of 97 above 100 MeV. The spectral fitting results show the source to be in a slightly elevated state as compared to the

[3]Available at `http://fermi.gsfc.nasa.gov/ssc/data/analysis/software/aux.`

2FGL value, with an integral flux of $4.5\pm1.0 \times 10^{-8}$ph cm^{-2}s^{-1} above 100 MeV and a spectral index of 1.9±0.1. No evidence for variability on weekly timescales is found, showing a 99.75% probability of being consistent with having a steady flux (χ^2=0.648 for 3 degrees of freedom). The sensitivity of LAT does not provide sufficient statistics for a more detailed investigation of variability, i. e. on daily timescales which result in TS values of less than 9.

4.2.3 Swift XRT

The *Swift* X-ray Telescope (XRT) is a space-based grazing incidence Wolter-I telescope which focuses X-rays between 0.2 and 10 keV onto a 110 cm^2 CCD (Gehrels et al., 2004). The *Swift* telescope took 16 windowed timing (WT) exposures of 1ES 1959+650 between 19 April 2012 and 1 June 2012 (MJD 56036 - 56079), each between 0.5 and 1.5 ksec long. An exposure of 0.7 ks on MJD 56067 was strictly simultaneous with VERITAS observations. The data were analyzed using the `HeaSoft` package Version 6.12. Rectangular source regions of length and width 45 and 8 pixels, respectively, were used. Similarly sized regions of nearby source-free sky were used for background. The exposures were grouped to require a minimum of 20 counts per bin and fit with an absorbed power-law model of the form $F(E)_{PL} = Ke^{-N_{\rm HI}\sigma(E)}(E/1{\rm keV})^{-\alpha}$, with a free neutral hydrogen column density parameter $N_{\rm HI}$, as in Furniss et al. (2013c), to allow for additional absorp-

tion of soft X-rays by gas intrinsic to the blazar. The model also contains a fitted normalization parameter K and the non-Thompson energy-dependent photoelectric cross-section $\sigma(E)$, as taken from Morrison & McCammon (1983).

The flux and index light curves for the *Swift* XRT observations are shown in the second and third panels from the top in Figure 4.1 and summarized in Table 4.2. The integral 2-10 keV flux recorded by the XRT ranged between 4.2 $\times 10^{-11}$ ergs cm^{-2}s^{-1} and 12.8 $\times 10^{-11}$ ergs cm^{-2}s^{-1} with an average flux of 7.5×10^{-11} ergs cm^{-2}s^{-1}, with photon indices ranging from 2.5 to 3. The X-ray emission appears to be relatively steady in the first five exposures.

The exposure on 20 May 2012 (MJD 56067) is the only strictly simultaneous observation with VERITAS, overlapping the first 0.7 ks of VERITAS observations which show a VHE flare from 1ES 1959+650. The steady 0.3 - 10 keV count rate observed by XRT (as shown in the bottom panel of Figure 4.2), shows that at least the first 0.7 ks (11.6 minutes) of the VHE flaring episode is not matched with a correlated elevated X-ray state.

The XRT observations on MJD 56074 show the blazar to be in an elevated state with a flux level of $12.9 \pm 0.1 \times 10^{-11}$ ergs cm^{-2}s^{-1}, nearly twice the average of 7.5×10^{-11} ergs cm^{-2}s^{-1}. This high state is observed to drop to approximately half the average (4.0 $\times 10^{-11}$ ergs cm^{-2}s^{-1}) in under two days. No contemporaneous high state is observed in the VERITAS data, but no firm conclusions can be drawn

due to the non-simultaneous nature of the exposures.

4.2.4 UV and Optical

Swift UVOT The *Swift*-XRT observations were supplemented with simultaneous UVOT exposures taken in the UVW1, UVM2, and UVW2 bands (Poole et al., 2008). The UVOT photometry is performed using the `HEASoft` program *uvotsource*. The source region consist of a single circular region with 5" radius, while the background region consists of several 15" radii circles of the nearby sky lacking visible sources. The results are corrected for reddening using E(B-V) coefficients from Schlegel et al. (1998) and the Galactic extinction coefficients are applied according to Fitzpatrick (1999). The largest source of error derived for the intrinsic flux points is due to the uncertainty in the reddening coefficients E(B-V). The UVOT W1, W2 and M2 flux values derived from the observations are shown in Figure 4.1, and summarized in detail in Table 4.3. These exposures show relatively steady flux values, with a small decrease up to MJD 56074.

Supe-LOTIS The Super-LOTIS robotic 0.6-meter telescope located on Kitt Peak in Arizona took R-band exposures of 1ES 1959+650 between MJD 56034 and 56080. During each night, we acquired three individual frames with the standard Johnson-Cousins R-band filter. Each image was reduced using an anal-

[4]For observations consisting of two time separated exposures, we denote the first with (a) and the second with (b). The MJD is given for the start of each exposure, respectively.

Table 4.2: *Swift* XRT summary of observations and spectral results.

***Swift* XRT Observation ID**[4]	**Observation Date** [MJD]	**Exposure Time** [ks]	**Power-law Index** α	**N_{HI} Density** [$\times 10^{21}$ **cm**$^{-2}$]	**Integral Flux 2-10 keV** [$\times 10^{-11}$ **ergs cm**$^{-2}$**s**$^{-1}$]	χ^2	**Degrees of Freedom**
00035025075	56036.51	1.0	2.95±0.06	2.2±0.1	7.4±0.3	191.1	180
00035025076	56037.72	1.5	2.82±0.04	2.16±0.08	8.9±0.3	299.5	245
00035025077	56051.41	1.0	2.71±0.05	1.89±0.09	7.8±0.3	206.9	195
00035025078	56064.38	1.1	2.57±0.05	2.0±0.1	9.3±0.3	225.5	207
00035025079	56067.39	0.7	2.53±0.06	1.9±0.1	8.4±0.3	124.2	156
00035025080 (a)	56074.69	0.6	2.53±0.02	2.3±0.1	12.0±0.1	150.0	170
00035025080 (b)	56074.75	0.6	2.52±0.05	2.2±0.1	12.9±0.1	154.3	178
00035025081 (a)	56075.23	0.9	2.64±0.06	2.1±0.1	7.0±0.3	140.9	153
00035025081 (b)	56075.57	0.3	3.1±0.1	2.7±0.3	4.3±0.3	46.4	46
00035025082	56076.69	0.9	2.78±0.07	2.0±0.1	4.2±0.3	131.1	124
00035025083	56078.43	1.0	2.59±0.04	2.1±0.1	9.4±0.3	187.8	204
00035025084 (a)	56079.57	1.5	2.52±0.05	1.9±0.1	9.3±0.3	188.4	171
00035025084 (b)	56079.70	0.5	0.78±0.08	2.5±0.2	10.4±0.2	101.2	98

Table 4.3: Summary of optical observations from the *Swift* UVOT

Date	**UVW1**	**UVW2**	**UVM2**
[MJD]	[$\times 10^{-11}$ **ergs cm^{-2}s^{-1}**]	[$\times 10^{-11}$ **ergs cm^{-2}s^{-1}**]	[$\times 10^{-11}$ **ergs cm^{-2}s^{-1}**]
56037	8.6±0.2	9.6±0.2	11.6± 0.3
56051	8.2±0.2	8.9±0.2	11.1± 0.3
56064	6.9±0.2	7.6±0.2	9.4± 0.3
56067	7.1±0.2	7.4±0.2	8.9±0.3
56075	5.9±0.1	–	7.5±0.2
56078	6.3±0.2	6.7±0.2	8.3±0.2
56079	6.4±0.2	6.8±0.2	8.3±0.2

ysis pipeline that, after subtracting the bias and the dark current, combines the flat-fielded frames in a single image for each night. Aperture photometry was performed for both the blazar and each of the seven reference stars detailed in the Landessternwarte Heidelberg-Königstuhl catalogue[5] with a circular aperture of 15". This aperture is large enough to encompass all the light enclosed in the irregular PSF. The local sky level is computed in a circular annulus of inner/outer radius of 18/25". The statistical error on each photometric point is ~ 0.1 mag. The final flux values of 1ES 1959+650 are calculated by applying the photometric zero-point derived for each night, comparing the instrumental magnitude of the reference stars to the known magnitudes in R band.

The R-band monitoring data from Super-LOTIS is shown in the bottom panel of Figure 4.1 and is summarized in Table 4.4. The observations show a relatively steady magnitude of approximately 13.8-14.0, with a conservative photometry error estimate of ±0.1 optical magnitude.

[5] `http://www.lsw.uni-heidelberg.de/projects/extragalactic/charts/1215+303.html`

iTelescope V and R-band exposures were taken by iTelescope between MJD 56028 and 56080. iTelescope is a robotic telescope system located in Nerpio, Spain. The telescopes used (T07 and T17) are twins, and are each of 431 mm (17-inch) aperture at f/6.8. They employ an SBIG STL-1100M CCD camera. The V filter is a standard Johnson-Cousins set. The R filter is not standard and requires a color correction, where the addition of approximately 0.040 magnitude transfers the non-standard filter magnitudes to the standard Johnson-Cousins R. The data were reduced with `MIRA Pro Version 7.0`. The reduction is with standard aperture (radius of 5") photometry, using the same standard stars as were used for the Super-LOTIS data reduction.

The V and R-band data are shown in the bottom panel of Figure 4.1 and summarized in Table 4.4. These observations show elevated luminosity in both the V and R bands (by approximately 0.2 magnitude) on two of the days where Super-LOTIS also provides R-band measurements approximately 2 hours before the iTelescope exposures were taken (shown in bold in Table 4.4). Comparison with the contemporaneous Super-LOTIS R-band measurements suggests that the blazar exhibits a small level of intra-night variability. This fast variability occurs on the same night as the X-ray flux is observed to be high, followed by a drop in flux which is displayed by the following XRT exposure less than a day later.

Table 4.4: Summary of optical observations from Super-LOTIS and iTelescope. The two pairs of exposures in bold are taken on the same night, less than three hours apart, and show a ∼0.2 magnitude difference suggesting a small level of intra-night variability in the R-band. The standard stars used to calibrate these measurements do not show any evidence of possible instrumental effects which might cause the discrepancy.

Exposure Date [MJD]	**Super-LOTIS R-band Magnitude**	**iTelescope R-band Magnitude**	**iTelescope V-band Magnitude**
56034.0	13.8±0.1		
56045.0	13.8±0.1		
56046.0	13.8±0.1		
56047.0	13.7±0.1		
56048.0	13.8±0.1		
56050.3	13.7±0.1		
56060.3	13.8±0.1		
56064.3	13.9±0.1		
56068.3	13.9±0.1		
56069.3	13.9±0.1		
56070.5	–	13.920±0.007	14.340±0.006
56071.5	–	13.926±0.003	14.349±0.005
56073.5	–	14.009±0.006	14.378±0.007
56074.3	**14.0±0.1**		
56074.5	–	**13.814±0.014**	**14.164±0.015**
56075.3	13.9±0.1		
56075.5	–	13.971±0.014	14.375±0.016
56076.3	**14.0±0.1**		
56076.5	–	**13.810±0.015**	**14.131±0.021**
56077.4	–	13.944±0.019	14.320±0.010
56078.3	14.0±0.1		
56078.5	–	13.928±0.007	14.270±0.005
56079.3	14.0±0.1		
56079.4	–	13.948±0.024	14.358±0.019
56081.7	13.814±0.020	14.239±0.027	
56082.3	14.0±0.1		
56083.3	14.1±0.1		
56084.3	14.0±0.1		
56085.3	14.0±0.1		

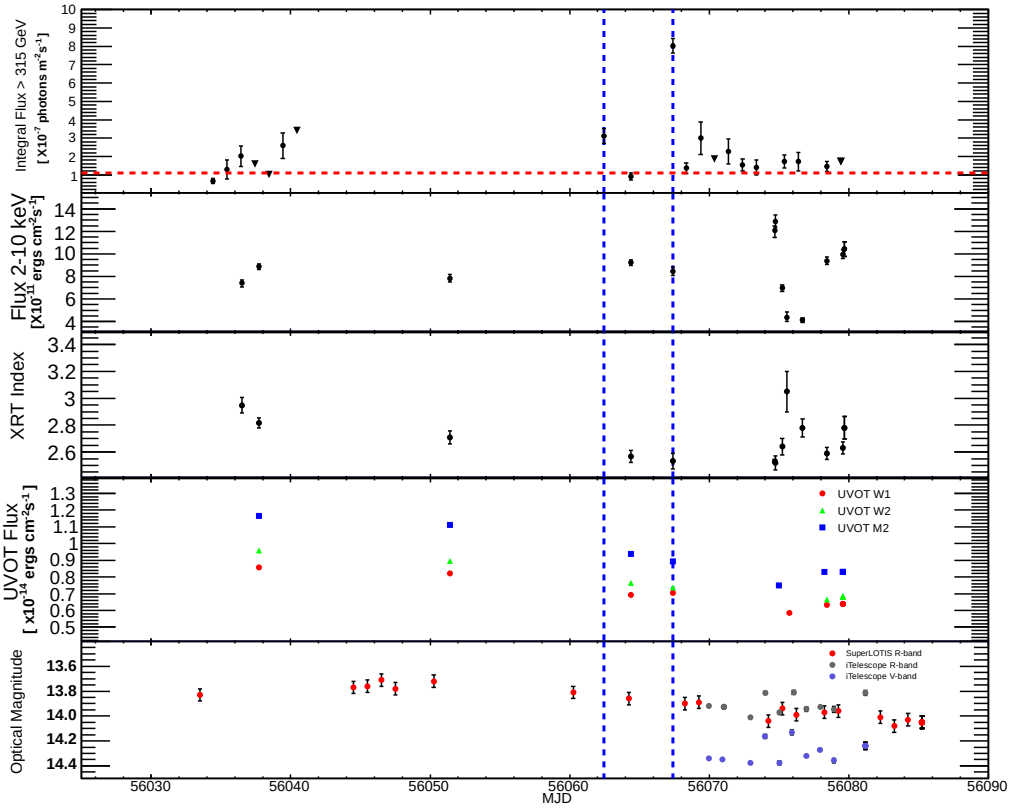

Figure 4.1: Broadband observations of 1ES 1959+650 in April and May of 2012. The top panel shows VERITAS integral flux values above 315 GeV, denoting upper limits with downward pointing arrows. The low-state VHE flux of this blazar (5% Crab from Aliu et al. (2013a)) is denoted by the red dotted line. MJD 56062 and 56067, denoted by blue dotted lines, are taken as the primary and secondary flares in the reflection model paradigm investigated here. In the two panels below this, the *Swift* XRT flux and spectral indices are shown. During the second flare day, VERITAS observed a maximum flux of order 10 times the low-state, lasting less than two hours, with no change observed in the X-ray flux as observed by the *Swift* XRT. The W1, W2 and M2 bands from UVOT exposures similarly show no evidence of increased UV flux during this VHE flare. The bottom panel observations in the R and V bands are shown from the Super-LOTIS and iTelescope.

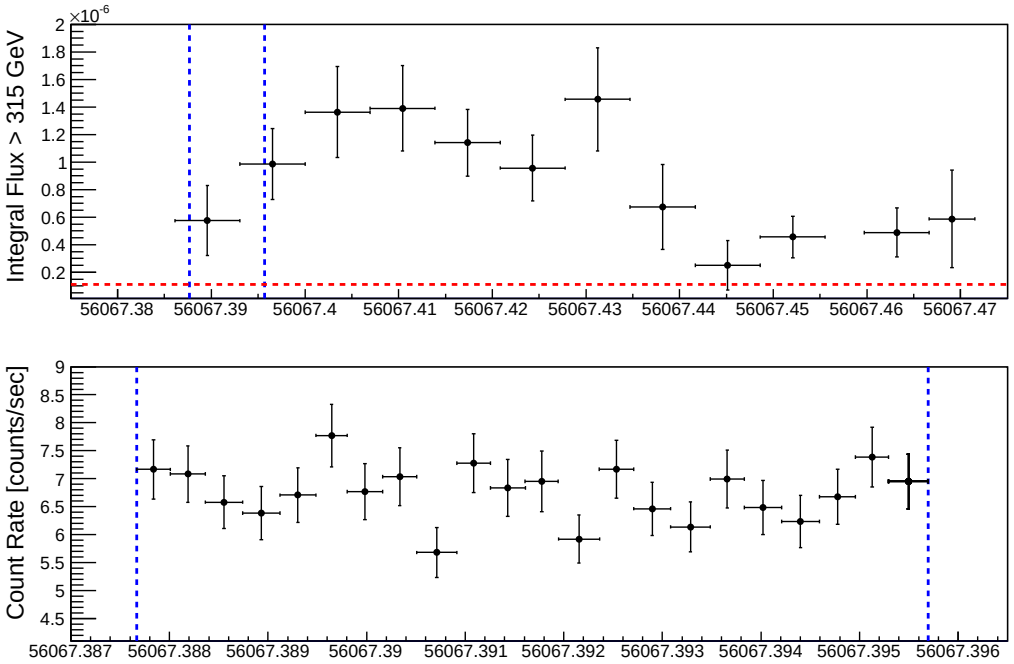

Figure 4.2: In the top panel, the VHE flux of 1ES 1959+650 as observed by VERITAS above 315 GeV on MJD 56067 in ten minute time bins. The start and end of the simultaneous XRT observations are denoted with dotted blue lines. In the bottom panel, the 0.3-10 keV count rate as observed by *Swift* XRT is shown over the simultaneous observation.

4.2.5 Summary of Observations

The broadband observations summarized above show an initial VHE flare to ∼3 times the average flux over the two dark runs, followed by a VHE flare five days later on MJD 56067 where no elevated X-ray state is observed. Additional variability is observed over the full window of observation, including an X-ray flux increase and intra-night variability on MJD 56075. The X-ray flux was observed to drop over the next two days, with no change in VHE flux observed during this time. We concentrate our modeling on the elevated VHE flux levels observed on MJD 56062 and 56067.

4.3 Modeling

In this section we investigate a possible scenario to describe VHE variability detected during the contemporaneous observations of 1ES 1959+650. We stress that our scenario is a choice, and that the variability can likely be accommodated within simpler models, or explained by the limitations of the dataset. Our choice is motivated, in part, by the evidence for an intervening gas within the blazar. We apply the same mirrored emission model which was used to describe the "orphan" flaring activity of 1ES 1959+650 previously (Böttcher, 2005). This model follows X-ray emission from a newly ejected component (blob) in the jet as it is reflected off dilute gas and/or dust in the vicinity of the jet. This reflected emission then

re-enters the jet shortly before the blob reaches the location of the reflector.

In order to apply this model to the data, we make a few necessary assumptions. First, we make the simplistic assumption that the blazar exhibited no additional flaring activity which was not captured by the monitoring of the broadband instruments. Secondly, we assume that the elevated VHE state observed on MJD 56062 by VERITAS is correlated with an (undetected) elevated X-ray state of the same factor (~ 3 times the average flux). Additionally, we assume that the VHE flare observed on MJD 56067 is the secondary, orphan gamma-ray flare resulting from the reflected photon field. Under these assumptions, there is a roughly five day delay between when the primary emission leaves the blob and when it re-enters the blob post-reflection.

More specifically, we assume that at a distance R_m from the central engine, moderately dense clouds of gas and dust intercept the primary-flare synchrotron emission, and re-process part of this flux back into the jet trajectory. Following Böttcher (2005), we can estimate the distance R_m from the time delay between the primary synchrotron flare (MJD 56062) and the orphan gamma-ray flare (MJD 56067) of $\Delta t \sim 5 \times 10^5$ s:

$$R_m \sim 2\,\Gamma^2\,c\,\Delta t \sim 1\,\Gamma_1^2\ \mathrm{pc}, \tag{4.1}$$

where $\Gamma = 10\,\Gamma_1$ is the bulk Lorentz factor of the blob, moving in the direction

of the reflector. Using an X-ray flux of order three times the average 2-10 keV flux measured by the XRT ($F_x^{\rm flare} \sim 3 \times 10^{-10}$ erg cm^{-2} s^{-1}), we can estimate the corresponding flux at the location of the reflecting cloud, as

$$F_m \sim \frac{d_L^2}{R_m^2} F_x^{\rm flare} \sim 1.1 \times 10^7 \, \Gamma_1^{-4} \, {\rm erg \, cm^{-2} \, s^{-1}}, \tag{4.2}$$

where d_L^2 is the distance between the blob and the reflecting cloud.

The accumulated flux will be intercepted by the blob within the time interval between emitting the first photons from the flare and intercepting the location of the cloud. This time is also characteristic of the time during which the cloud receives this flux, and can be estimated as is done in Böttcher (2005)

$$\Delta t_{\rm fl} \sim \frac{R_m}{8 \, \Gamma^4 \, c} \sim 1.3 \times 10^3 \, \Gamma_1^{-2} \, {\rm s}. \tag{4.3}$$

We can therefore calculate an average flux received by the cloud as

$$F_m^{\rm ave} \approx \frac{F_x^{\rm qu} \, d_L^2}{c \, \Delta t_{\rm fl}} \int\limits_{R_b}^{R_m} \frac{dx}{x^2} \approx \frac{F_x^{\rm qu} \, d_L^2}{c \, \Delta t_{\rm fl} \, R_b} \sim 5.3 \times 10^{13} \, \Gamma_1^2 \, R_{16}^{-1} \, {\rm erg \, cm^{-2} \, s^{-1}}, \tag{4.4}$$

where we have used an estimate of the quiescent synchrotron X-ray flux from 1ES 1959+650 of $F_x^{\rm qu} = 1.0 \times 10^{-10}$ erg cm^{-2} s^{-1} (similar to the average found from the *Swift* XRT observations), and $R_b = 10^{16} \, R_{16}$ cm is the radius of the blob. We can see that this accumulated quiescent flux strongly dominates the illumination of the dust clouds and therefore does not largely depend on the

assumed primary X-ray flare flux level. For a characteristic density of the clouds of $n_d \sim 10^6$ cm^{-3}, this leads to an ionization parameter

$$\xi_{\rm ion} \equiv \frac{F_m^{\rm ave}}{n_c} \sim 5 \times 10^7 \text{ erg cm s}^{-1}. \tag{4.5}$$

This implies that any dust is expected to be destroyed, and all gas to be highly ionized by the impinging X-ray emission. If the cloud is thermally re-processing this flux, this would require an equilibrium temperature $T_{\rm equi} \sim 36,000$ K, which also requires the gas to be highly ionized. We therefore conclude that the most likely mode of re-processing the accumulated jet synchrotron emission is Compton reflection off free electrons in the highly ionized cloud. This ionized gas might also act as a shield to molecular gas such as CO, as predicted in photo-dissociation region models (e. g. Tielenn & Hollenbach (1985); Krumholz et al. (2009); Glover & Clark (2012)).

The characteristic photon frequency of jet synchrotron photons is $\nu_{\rm sy} \sim 10^{18}$ Hz (Aliu et al., 2013a), corresponding to a normalized photon energy of $\epsilon_{\rm sy} \equiv h\nu_{\rm sy}/(m_e c^2)$ $\sim 10^{-2}$. Upon Compton reflection by the cloud, this will be boosted in the jet rest frame to $\epsilon'_{\rm sy} \sim 0.1\,\Gamma_1$. Therefore, any relativistic electrons (with $\gamma_e \geq 10$) will interact with these reflected photons in the Klein-Nishina regime, resulting in strongly suppressed Compton scattering, making the production of a secondary, gamma-ray flare five days after the primary flare unlikely in a solely leptonic

scenario.

It can be seen that the bulk Lorentz factor of the blob is a critical unknown parameter in this model, with key derived parameters depending on the magnitude of the parameter Γ. The observed synchrotron peak frequency of 1ES 1959+650 is $\sim 1 \times 10^{18}$ Hz, corresponding to $\epsilon_{\rm sy} \sim 0.01$. Therefore, even without any blue-shifting from bulk motion, Compton scattering in the Thomson regime happens up to $\epsilon_{\rm C} \sim 1/\epsilon_{\rm sy} \sim 100$, corresponding to $\sim$50 MeV. Therefore, even for $\Gamma = 1$, a synchrotron mirror scenario would not efficiently produce gamma rays via Compton scattering.

Relativistic protons with Lorentz factors of $\gamma_p \geq 6 \times 10^3$, on the other hand, can interact with the reflected photons through $p\gamma$ pion production processes. Following the analysis in Böttcher (2005) and using the average flux $F_m^{\rm ave}$ from Eq. 4, we find that producing a secondary VHE gamma-ray flare with a luminosity of $L_{\rm VHE} \sim 1.5 \times 10^{45}$ erg s^{-1} requires a total number density n_p of relativistic protons

$$n_p \sim 1.4 \times 10^5 \, \Gamma_1^{-11} \, \tau_{-1}^{-1} \, R_{16}^{-2} \, {\rm cm}^{-3}, \tag{4.6}$$

where $\tau_m = 0.1 \, \tau_{-1}$ is the fraction of incident flux reflected by the cloud. We have assumed that the protons have a power-law distribution in energy $N(\gamma_p) \propto \gamma_p^{-2}$ with a low-energy cut-off at $\gamma_{\rm p,min} = \Gamma$. This corresponds to a total (co-moving

frame) energy in relativistic protons in the blob of

$$E'_{b,p} \sim 3.2 \times 10^{49}\, \Gamma_1^{-10}\, \tau_{-1}^{-1}\, R_{16}\ \mathrm{erg}, \tag{4.7}$$

and a kinetic power in the jet, carried by relativistic protons, of

$$L_p \sim 7.3 \times 10^{45}\, \Gamma_1^{-8}\, \tau_{-1}^{-1}\, f\ \mathrm{erg\ s^{-1}}, \tag{4.8}$$

where f is the filling factor of the jet, i.e., the fraction of the jet length occupied by plasma containing relativistic protons.

The power requirement in Eq. 4.8 is quite moderate if one allows for a plausible filling factor $f \leq 0.1$. Also, note the extremely strong dependence of the estimates in Eqs. 4.6 – 4.8 on the Lorentz factor. A value of Γ just slightly above 10 will reduce all energy requirements to very reasonable values, corresponding to a population of relativistic protons with energies between 10 and 100 TeV.

4.4 Summary and Conclusions

We report contemporaneous broadband observations of the VHE-emitting blazar 1ES 1959+650, including 0.7 ks of strictly simultaneous *Swift* XRT and VERITAS observations occurring during a period of elevated VHE flux. This blazar has been shown to exhibit extreme flaring episodes with uncorrelated variation in the synchrotron and gamma-ray SED peaks in the past (Krawczynski et al., 2006), which

could be described in a mirrored non-thermal emission environment, with a blob of relativistic particles moving toward a dilute reflector made of gas or dust intrinsic to the blazar.

Motivated by the previous episode of uncorrelated variability as well as recent compelling evidence for the existence of dilute gas within the blazar, we investigate recent broadband observations using the mirrored emission paradigm. In applying this model to the available data, we use assumptions that the contemporaneous variable states show both the primary and secondary flaring periods, as predicted in the mirrored emission scenario. These flaring periods are separated by approximately five days and are used to estimate the distance to a dilute reflector. Additionally, in the application of this model, we assume that no variability went undetected during periods where no observations took place.

We find that due to the close proximity of the dilute reflector, the average X-ray flux is sufficiently bright to highly ionize the reflecting clouds and dust. Any X-ray flux above the average X-ray flux of 7.5×10^{-11} ergs $\mathrm{cm}^{-2}\mathrm{s}^{-1}$, in fact, would result in similar ionization of the cloud, showing that the proximity of the cloud plays a major role in the conclusions derived from the application of this model. The ionization of the cloud and dust makes Compton reflection on free electrons the most likely mode of re-processing the jet synchrotron emission. The emission from the ionized reflector re-enters the blob in the Klein-Nishina regime,

suppressing leptonic Compton up-scattering which might be responsible for an orphan gamma-ray flare.

In this case, however, we find that the production of an elevated gamma-ray peak flux is still possible if there are hadrons within the blob between energies of 10 and 100 TeV. This hadronic synchrotron mirror model, in which relativistic protons interact with the reflected emission to produce charged and neutral pions, provides a possible explanation of the uncorrelated gamma-ray variability as assumed from the broadband observations.

Evidence for hadrons as the source of the highest energy emissions from blazars would highlight these galaxies as sources for cosmic rays. However, the energy of the hadrons predicts a population with energies between 10 and 100 TeV, which is insufficient as an explanation for the source of the ultra-high-energy cosmic rays. Unfortunately, the expected neutrino number flux for the outlined scenario would be within a factor of two of the VHE photon number flux and is insufficient to be detected by current generation neutrino detectors such as IceCube Reimer et al. (2005).

Under the blazar evolutionary paradigm (Böttcher & Dermer, 2002; Ghisellini et al., 1998), 1ES 1959+650 would have a very small amount of gas, if any. The evolution along the sequence is proposed to be connected to the decrease in the accretion rate and to the onset of radiatively inefficient accretion (Ho, 2008; Trump et

al., 2011). At the beginning of the sequence, blazars have an appreciable external radiation field that facilitates effective cooling, resulting in low-frequency-peaked synchrotron and inverse-Compton emission. A progressively lower contribution of the external field along the sequence inhibits efficient cooling, resulting in an higher frequency peak of the synchrotron and inverse Compton emission (i.e. an HSP such as 1ES 1959+650). The spectral variations across different blazar subclasses can also be described by certain selection effects (Padovani & Giommi, 1995).

Based on the categorization of 1ES 1959+650, blazar evolution would support variability patterns which can be described by a simple SSC emission mechanism similar to that which is found for other VHE-emitting high-synchrotron-peaked (HSP) blazars (e.g. Acciari et al. (2009b); Acciari, et al. (2010)). The prior observations of molecular gas and an orphan flare suggest that this blazar does not follow the blazar evolutionary paradigm or, perhaps, is not truly an HSP BL Lac. Our application of mirrored emission to more recent broadband observations, although requiring various assumptions, support the deviation of 1ES 1959+650 from the HSP class. Stronger conclusions on the non-thermal emission mechanism at work within the jet of 1ES 1959+650 and a more reliable application of time-dependent modeling would be possible with a dataset which includes high cadence simultaneous observations from instruments such as *Swift* and VERITAS.

Part II

Using Very-High-Energy Emitting Blazars for Cosmological Insight

"The most exciting phrase to hear in science, the one that heralds new discoveries, is not 'Eureka!' (I found it!) but 'That's funny ' "

– Isaac Asimov (1920 - 1992)

In observational cosmology the diffuse background radiation fields that surround us provide invaluable insight into the history of our Universe. A prominent example of such a radiation field is the 2.7 K thermal afterglow of the Big Bang, the cosmic microwave background. At shorter wavelengths, from the ultraviolet to the far-infrared, the extragalactic background light (EBL) consists of the accumulated and reprocessed radiation of all starlight produced thus far (Primack et al., 2005; Gilmore et al., 2009; Finke et al., 2010; Dominguez et al., 2011). As such, measurements of the intensity and evolution of the EBL offer a critical test of cosmology and structure formation. Unfortunately, direct measurements of the EBL are difficult due to strong foreground sources in our solar system (Zodiacal light) and the Galaxy. Moreover, a direct measurement would only reflect the

current integrated state, which leaves the challenging task of modeling the EBL as a function of time.

These challenges can be overcome when absorption of VHE gamma rays from extragalactic sources is used to probe the EBL. VHE gamma rays that propagate through the intergalactic medium are absorbed by low energy EBL photons via pair production, $\gamma + \gamma \rightarrow e^+ + e^-$ (Nikishov, 1962; Gould & Shréder, 1967). This absorption process deforms the intrinsic VHE gamma-ray spectra emitted by extragalactic objects such as blazars. This deformation can be used to estimate the spectral properties of the EBL (Aharonian et al., 2006; Albert et al., 2008b; Orr et al., 2011; Dominguez et al., 2013).

If the redshift of the VHE-detected blazar is known, insight into the extragalactic propagation of VHE gamma rays and the relativistic particle processes within blazar jets is more accessible. The bright and featureless nature of the active galaxy core often outshines the underlying absorption and emission lines of the host galaxy, making spectroscopic redshift measurements difficult. In lieu of a spectroscopic redshift measurement, a strict lower limit on the distance can be placed through the observation of far UV absorption by the intergalactic medium. Additionally, the lack of absorption signatures beyond the highest redshift Lyman system observed can also be used to place a statistical upper limit on the distance to the blazar. These observations are possible with the *Hubble Space Telescope*

Cosmic Origins Spectrograph (HST/COS) and have thus far been completed for four VHE blazars (Danforth et al., 2010; Furniss et al., 2013a; Danforth et al., 2013a; Furniss et al., 2013b).

The redshift upper and lower limits for 3C 66A inferred from the observation of Lyman forest absorption show the VHE emitting blazar to be at a distance such that the archival VHE spectrum cannot be used to constrain the density of the EBL, as described in **Chapter 5**. The redshift lower limit found for PKS 1424+240 is unexpectedly high, and brings the general understanding of the gamma-ray propogation across extragalactic distances and the relativistic particles undergoing non-thermal emission within blazar jets into question, as described in **Chapter 6**.

Chapter 5

On the Redshift of the Very High Energy Blazar 3C 66A

This work has been published in the Astrophysical Journal (*Furniss et al. 2013, ApJ, 766, 35*). The corresponding author of the work is Amy Furniss. No content was modified aside from necessary formatting. The full author list of this work can be found in Appendix D.

Abstract

As a bright gamma-ray source, 3C 66A is of great interest to the high-energy astrophysics community, having a potential for placing cosmological constraints on models for the extragalactic background light (EBL) and the processes which contribute to this photon field. No firm spectroscopic redshift measurement has been possible for this blazar due to a lack of intrinsic emission and absorption features in optical spectra. We present new far-ultraviolet spectra from the Hubble Space Telescope/Cosmic Origins Spectrograph (HST/COS) of the BL Lac object 3C 66A covering the wavelength range 1132 to 1800 Å . The data show a smooth continuum with intergalactic medium absorption features which can be used to place a firm lower limit on the blazar redshift of $z \geq 0.3347$*. An upper limit is set by statistically treating the non-detection of additional absorbers beyond* $z = 0.3347$*, indicating a redshift of less than 0.41 at 99% confidence and ruling out* $z \geq 0.444$ *at 99.9% confidence. We conclude by showing how the redshift limits derived from the COS spectra remove the potential for this gamma-ray emitting blazar to place an upper limit on the flux of the EBL using high energy data from a flare in October of 2009.*

5.1 Introduction

Direct measurements of the extragalactic background light (EBL) are difficult due to strong foreground sources in our solar system (Zodiacal light) and the Galaxy (Hauser & Dwek, 2001). If a direct measurement were possible, it would only reflect the current integrated state, leaving still the model-dependent task of extracting the time evolution. These difficulties have been overcome through the use of extragalactic very-high-energy (VHE, E$\geq$ 100 GeV) gamma rays from blazars with known redshifts (e. g. Aharonian et al. (2006); Mazin & Raue (2007); Albert et al. (2008b); Gilmore et al. (2009); Orr et al. (2011)), the most commonly detected type of VHE extragalactic source. A blazar is a type of active galactic nucleus (AGN) that has a jet pointed towards the observer, and exhibits a highly polarized broadband spectrum from beamed, non-thermal emission processes.

The energy-dependent absorption of gamma rays by the EBL softens the intrinsic VHE gamma-ray spectra emitted by extragalactic objects. The details of the absorption depend on the shape of the EBL spectral energy distribution (SED) in the near-IR to optical band. Additionally, the total power and the shape of the SED of the EBL is shown to vary strongly with redshift in the currently available models, such as Dominguez et al. (2011); Gilmore et al. (2012); Kneiske & Dole (2010); Finke et al. (2010). To correctly account for the gamma-ray absorption, an accurate redshift of the VHE extragalactic target is required.

Approximately one-third of the current VHE extragalactic catalog[1] is made up by blazars at unknown or poorly-constrained redshift. 3C 66A is one of these blazars, with an uncertain spectroscopic redshift based on possible corroborating measurements of single lines (Miller et al., 1978; Kinney et al., 1991; Bramel et al., 2005). Despite multiple attempts, in particular two high signal-to-noise measurements using Keck I (shown in Figure 5.1), no solid spectroscopic measurement based on the detection of multiple lines from the host galaxy has been possible. The lack of spectral features is not surprising given that 3C 66A is a BL Lac-type active galactic nucleus that, by definition, displays weak or no lines.

To overcome the inherent featureless characteristic of the 3C 66A optical spectrum and enable deabsorption of the VHE spectrum with reliable redshift information, we have determined limits on the redshift of the blazar through the observation and statistical analysis of far UV (FUV) absorption by the low z intergalactic medium (IGM). This method, already applied to the VHE blazars PG 1553+113 and S5 0716+714 (Danforth et al., 2010, 2013a), sets a redshift lower limit using absorption lines caused by the intervening IGM. Further, given the expected distribution of IGM absorbers as a function of redshift, one can model any lack of absorption lines at longer wavelengths to statistically infer an upper limit on the blazar redshift.

[1] `http://tevcat.uchicago.edu/`

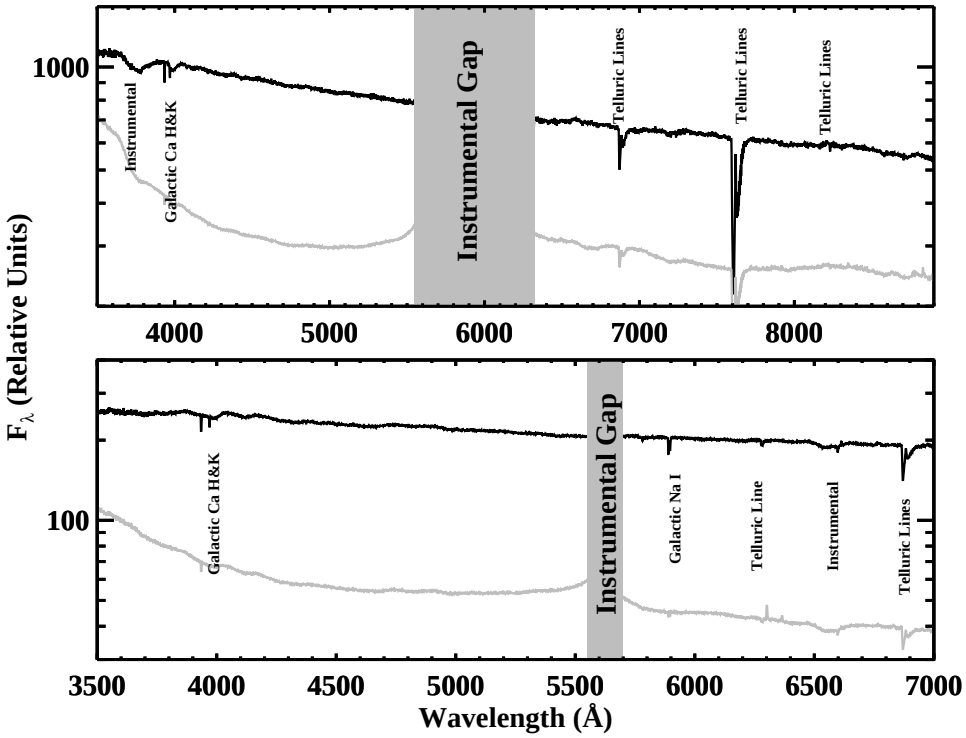

Figure 5.1: Keck/LRIS spectra (black) and error array (scaled by 50×; grey) of the optical emission from 3C 66A from September 2009 (top, relative high state) and October 2011 (bottom, relative low state). The gaps in the spectra are due to the dichroic filter of the instrument. We have additionally cut the 2011 spectrum at 7000 Å due to uncertainties introduced in calibration. All significant absorption features identified in the spectra are associated with the Earth or Milky Way. The details of this spectral analysis for each of these observations are completed as described in Abdo et al. (2011). Even at this exquisite S/N (over 100 per pixel for both exposures) there are no features with which to place a constraint on the redshift of this blazar.

5.2 Observations and Spectral Analysis

3C 66A was observed with the Cosmic Origins Spectrograph (COS) during two epochs as part of two different programs. The blazar was observed for five HST orbits on 1 November 2012, with the medium resolution G130M grating COS/G130M ($1135 < \lambda < 1450$ Å, 15.3 ksec) as part of program 12621 (PI: Stocke). Three more orbits were devoted to observations with the COS/G160M ($1400 < \lambda < 1795$ Å, 7.2 ksec) grating under program 12863 (PI: Furniss) on 8 November 2012. The calibrated, one-dimensional spectra for each exposure were obtained from the Mikulski Archive for Space Telescopes (MAST).

The G130M data show a flux mis-match between the short and long-wavelength segment of each exposure and a $\sim 8\%$ correction is applied to each before coaddition to bring them into the expected smooth continuum. The G160M data are considerably noisier; no flux discrepancy was observed and no correction was undertaken. The corrected exposures were then coadded with the standard IDL procedures described in detail by Danforth et al. (2010). This procedure includes an automatic scaling of the exposures taken during different epochs. The continuum flux level appears to have varied by $\sim 10\%$ during the week between observing epochs, well within the current flux calibration uncertainty.

The combined spectrum continuously covers the wavelength interval $1132 - 1800$ Å, and shows the expected smooth continuum and narrow absorption fea-

tures. The data quality varies over the spectral range due to the different sensitivities and exposure times in the two gratings. The mean signal to noise per pixel in the continuum is ~ 10 (~ 5) with nominal dispersions of 9.97mÅ /pixel (12.23Å /pixel) in the G130M (G160M) portion of the spectrum. Signal to noise values per seven-pixel resolution element are approximately twice these values (see Keeney et al. (2012)). For additional details on the COS instrument, see Ghavamian et al. (2009) and Kriss (2011).

Detailed analysis of these data and of the intervening absorption line systems will be presented in Danforth et al. (in prep.). In this paper, we exclusively focus on the spectral features that are useful to constrain the unknown redshift of the blazar ($z_{\rm blazar}$). The goal of the following analysis is to use absorption lines that arise from gas clouds in the IGM to establish a firm lower limit on the distance to 3C 66A and to set an upper limit for the blazar redshift based on a statistical argument.

A visual inspection of the spectrum reveals the presence of multiple absorption systems for which both Lyman$-\alpha$ and Lyman$-\beta$ (Lyα and Lyβ) lines are detected. Among those, we identify three clouds at $z_{\rm abs} \sim 0.3283$, 0.3333, and 0.3347 (see Figure 5.2). All other lines detected at >4 sigma significance redward of these three Lyα systems are identified as Milky Way absorption (see Figure 5.3). Thus, because of the presence of a system at $z = 0.3347$, we set a secure red-

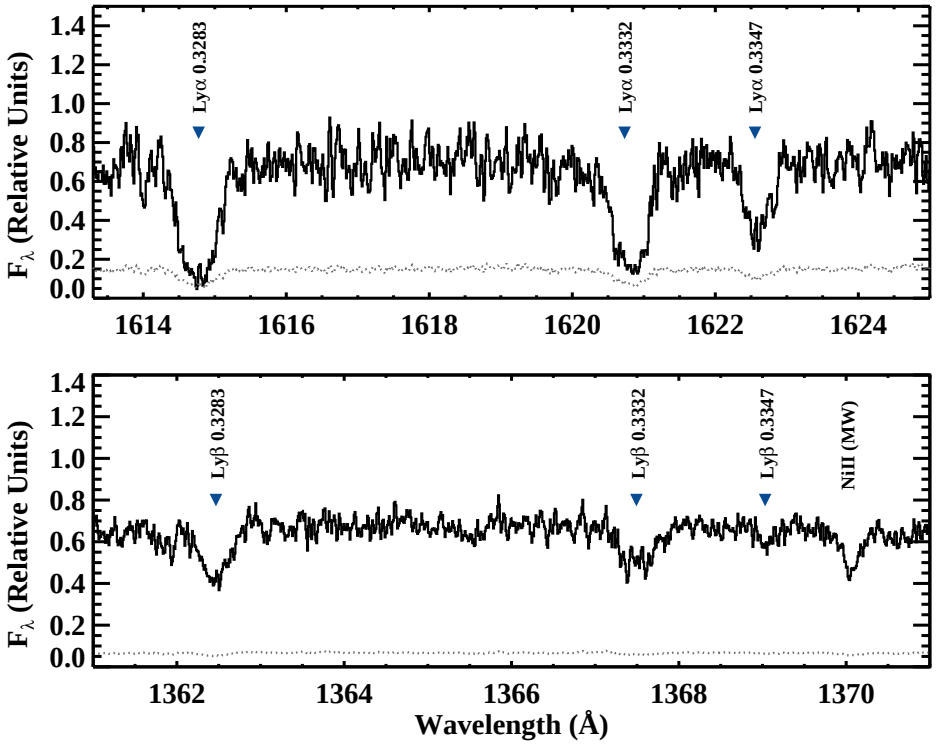

Figure 5.2: Detail of the COS spectrum of 3C 66A in the regions where we identify Lyα (top) and corresponding Lyβ (bottom) absorption lines for three gas clouds at $z_{\rm abs} \sim 0.3283$, 0.3333, and 0.3347. Absorption associated with Galactic Ni 2 is also labeled in the bottom panel.

shift lower limit of 3C 66A at $z_{\rm blazar} \geq z_{\rm ll} = 0.3347$. We also search the spectrum for O 6 ($\lambda\lambda 1031, 1037$) doublets that, owing to their bluer rest-frame wavelengths, could yield a more stringent redshift lower limit than the one set by absorption in the Lyman series. However, we do not find any instances of absorption beyond $z \sim 0.33$.

Next, we can exploit the lack of absorption beyond $z_{\rm ll} = 0.3347$ to set an upper limit $z_{\rm ul}$ to the blazar redshift following a statistical argument. The frequency

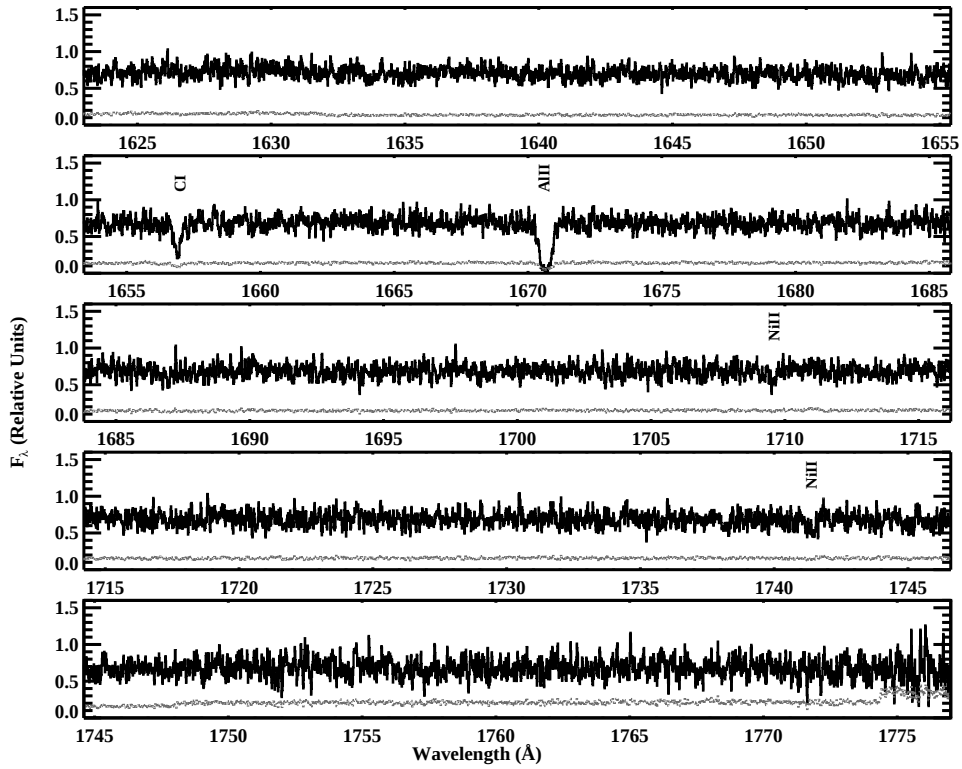

Figure 5.3: Red portion of the G160M spectrum, redward of where we identify Lyα lines at $z_{\rm abs} \sim 0.33$. All the labeled lines arise in the Milky Way. The lack of absorption of extragalactic origin places the redshift lower limit of 3C 66A at $z_{\rm blazar} \geq 0.3347$.

of absorption lines arising from the Lyman forest in the local universe has been measured along sightlines to extragalactic sources by different authors (e.g. Penton et al., 2004; Danforth & Shull, 2008). It is common to express this quantity with the function $dN(W > W_0)/dz$ which describes the average number of absorption lines with rest-frame equivalent width in excess to W_0 per unit redshift. We can therefore estimate the number of lines we expect to detect between $z_{\rm ll}$ and $z_{\rm ul}$, given the rest-frame limiting equivalent width $W_{\rm lim}$ of the COS spectrum. By comparing the predicted number of absorption lines in a given redshift interval with the lack of detection beyond $z_{\rm ll} = 0.3347$, we obtain redshift upper limit.

First, we generate 1000 mock spectra in the observed wavelength range $1215 - 1800$ Å by drawing Lyman forest lines from a distribution as a function of redshift such that the number of lines satisfies the observed $dN(W > W_0)/dz$. In this analysis, we assume no evolution in Lyman-α forest line incidence and adopt the frequency distribution from Danforth & Shull (2008), although a similar result is obtained if we adopted the distribution from Penton et al. (2004). Next, we assign to each line a Doppler parameter drawn from the observed distribution in the local IGM (Danforth & Shull, 2008). During this step, we assume that the Doppler parameter is not correlated with the equivalent width of the line. Given a line equivalent width, its redshift, and a Doppler parameter, we compute the observed limiting equivalent width $W_{\rm lim}$ (at 5σ) using the formalism developed for

COS spectra by Keeney et al. (2012) and we record only those lines which would be detected in the observed COS spectrum. Note that this procedure naturally accounts for "shadowing" due to Milky Way absorption lines.

The top panel of Figure 5.4 shows the number of intervening absorption lines detected in 1000 mock spectra within the redshift interval $0.335 \leq z \leq 0.444$. According to this Figure, we should expect to detect ~ 5 or more lines if 3C 66A lies at $z_{\rm ul} > 0.444$, and, although realizations with no lines are possible, they are extremely rare ($< 1\%$ of the total trials). Under the simplistic assumption that the number of absorption lines is not correlated in velocity space, the mock realizations shown in the top panel of Figure 5.4 follow a Poisson distribution. Therefore, we can adopt Poisson statistics to express the probability of finding no detected lines between $z_{\rm ll}$ and $z_{\rm ul}$, given a typical number of Lyman forest lines in that redshift interval $N(z_{\rm ll} < z < z_{\rm ul})$.

As shown in the bottom panel of Figure 5.4, the expected number of absorption lines increases proportionally to the redshift interval $\Delta z = z_{\rm ul} - z_{\rm ll}$ and the probability of finding no absorption lines $P(N = 0)$ exponentially decreases with redshift. At $z_{\rm ul} \sim 0.41$, $P(N = 0) \sim 0.01$, and therefore we conclude that 3C 66A is likely to lie between $0.3347 < z_{\rm blazar} \leq 0.41$. We can further rule out $z_{\rm blazar} \geq 0.444$ based on the fact that $P(N = 0) \sim 0.001$ for $z_{\rm ul} \sim 0.444$. We note that consistent probabilities can be recovered directly from the Monte Carlo sim-

ulations, without explicitly using Poisson statistics. However, it should be noted that our Monte Carlo simulations do not include correlated absorption systems in the Lyα forest. Further, this calculation does not account for mechanisms that could enhance (e.g. galaxy clustering) or suppress (photoionization along the line of sight) the incidence of Lyα lines in proximity to a blazar compared to the mean value observed in the IGM, although there is no evidence for highly ionized gas (i.e. N 5 absorption) at $z \sim 0.335$. With proximity effects included, the predicted limits are subject to ~ 1000 km s^{-1} uncertainty (i.e. ~ 0.003 in redshift space). Notably, there have been previous suggestions that 3C 66A is a member of a cluster at $z \sim 0.37$ (Butcher et al., 1976; Wurtz et al., 1993, 1997).

The limits placing the redshift between 0.3347 and 0.41 disfavor the past tentative measurements of $z = 0.444$ by Miller et al. (1978) and Kinney et al. (1991), both of which were based on the measurement of single, weak lines. The limits derived from the COS observations are, however, in good agreement with other past estimates of the blazar distance. Finke et al. (2008) set a lower limit of z ≥ 0.096, an estimation based on the expected equivalent widths of absorption features in the blazar host galaxy, while a distance estimate of $z \simeq 0.321$, noting a large error, was formed based on the assumption that host galaxies of a blazars could be taken as standard candles. An estimate for the blazar redshift of $z = 0.34 \pm 0.05$ was found by Prandini et al. (2010), who extracted the approximate redshift by

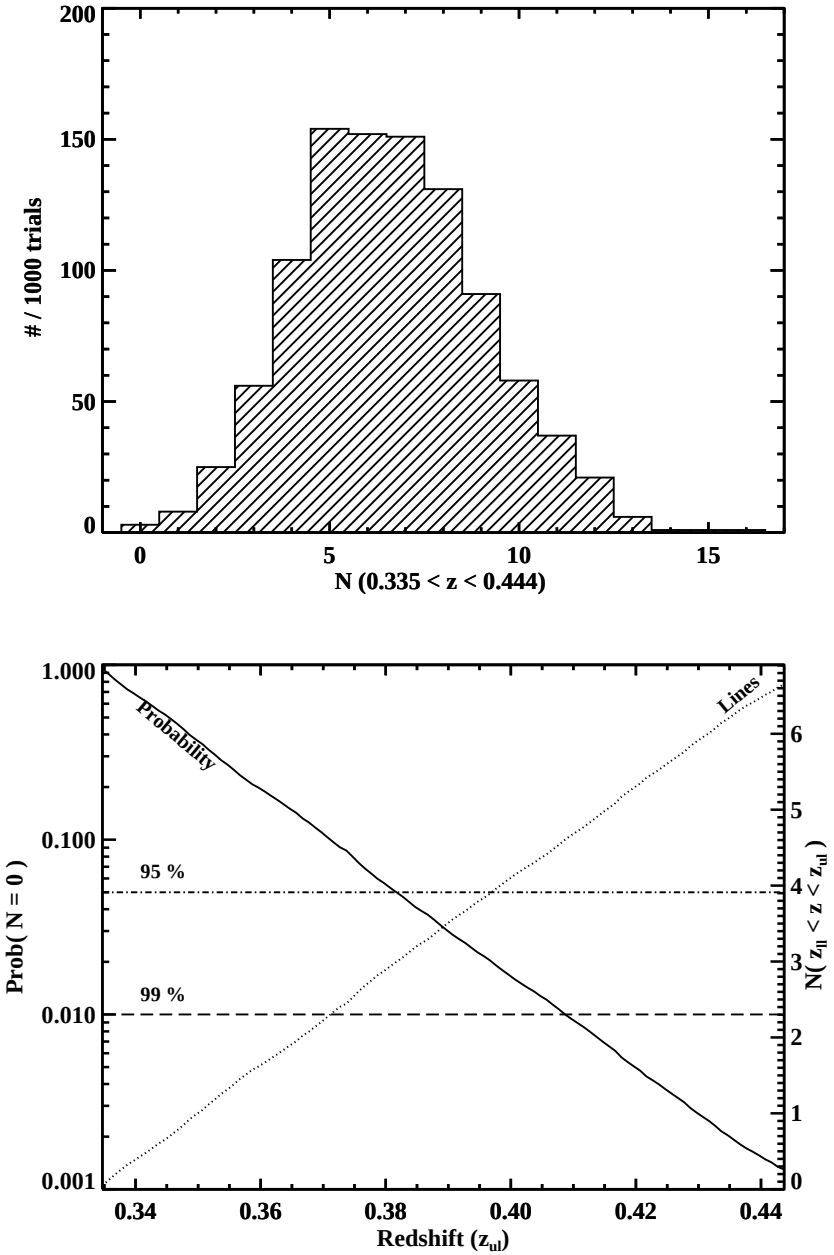

Figure 5.4: *Top* Distribution of the number of lines detected in 1000 mock spectra for $0.335 < z < 0.444$. *Bottom* The probability to observe no Lyα lines if 3C 66A lies beyond $z_{\rm ul}$ given the expected number of Lyα lines in the redshift interval $z_{\rm ll} < z < z_{\rm ul}$ derived from Monte Carlo simulations (dotted line).

correcting the TeV spectrum of the blazar for EBL absorption to match the index measured by the *Fermi* Large Area Telescope (LAT; Atwood et al. (2009)), most sensitive to gamma rays between 300 MeV and ∼100 GeV which are largely unaffected by the EBL. The redshift limits for 3C 66A are also in good agreement with a recent EBL model-independent study of the gamma-ray horizon, as determined by synchrotron self-Compton modeling of VHE blazar broadband spectra (Dominguez et al., 2013).

5.3 Absorption of Very High Energy Gamma-rays from 3C 66A

The energy- and redshift-dependent absorption of gamma rays by the EBL can be estimated using model-specific optical depths, $\tau(E, z)$, where the intrinsic flux (F_{int}) can be estimated by the observed flux (F_{obs}) using the relation $F_{int} \sim F_{obs} \times e^{\tau(E,z)}$. The intrinsic index of a blazar can be used to estimate the spectral properties of the EBL under the physically motivated assumption that the intrinsic spectrum of a source undergoing Fermi shock acceleration, characterized by the power-law dN/dE $\propto E^{-\Gamma}$, cannot be harder than $\Gamma = 1.5$. If the intrinsic VHE spectrum is significantly harder than the Γ=1.5 limit, it can be argued that the gamma-ray opacity of the EBL model which was used for deabsorption is too

high. The index limit of 1.5 is derived from the standard leptonic and hadronic emission scenarios used to describe blazar non-thermal emission. This limit is also in agreement with the hardest gamma-ray index reported by the *Fermi* LAT for a blazar (Nolan et al., 2012). The indices for sources derived from photons with energies of less than 100 GeV are not significantly affected by EBL absorption and so reflect the intrinsically emitted spectra of blazars in the high energy gamma-ray band.

Under the assumption that blazars do not harden with increasing energy, EBL flux constraints are also possible by comparing deabsorbed VHE spectra to the extrapolations based on the LAT-measured spectral indices. Using this method, the *Fermi* and VERITAS indices measured during a state of elevated flux from 3C 66A in October of 2009 ($\Gamma = 1.8 \pm 0.1_{stat}$ and $4.1 \pm 0.6_{stat}$, respectively; Abdo et al. (2011)) allow the investigation of possible constraints on the EBL density, pending a reliable distance measurement. Previously, the deabsorption of the VHE spectrum of 3C 66A has been completed with the uncertain spectroscopic redshift of $z = 0.444$ (e. g. Finke et al. (2010); Dominguez et al. (2011); Aleksić et al. (2011)). Notably, Gilmore et al. (2012) shows that the intrinsic spectrum derived from deabsorption of 3C 66A with the tentative redshift of $z = 0.444$ is the hardest of the deabsorbed VHE BL Lacertae objects.

Figure 5.5 shows the VERITAS measured VHE spectrum of the blazar 3C 66A

Table 5.1: Intrinsic indices (Γ) resulting from the deabsorption of the VERITAS observed spectrum reported in Abdo et al. (2011). Indices are calculated by taking the VERITAS-measured differential flux and flux errors and multiplying by e^{τ}, where τ is an energy and redshift dependent optical depth taken from the EBL models. The resulting flux in each bin is then fit with the differential power-law of the form $dN/dE = (E/E_o)^{-\Gamma}$, where E_o is 250 GeV.

EBL Model Used	Deabsorbed Index $z = 0.3347$	Deabsorbed Index $z = 0.41$
Gilmore et al. (2012)	2.8±0.6	2.3±0.6
Finke et al. (2010)	2.4±0.6	1.9±0.6
Kneiske & Dole (2010)	2.8±0.6	2.4±0.6
Dominguez et al. (2011)	2.6±0.6	2.1±0.6

from Abdo et al. (2011) (black solid line) when deabsorbed for the redshift upper and lower limits from this work. These deabsorbed spectra are calculated by multiplying the measured differential flux values by $e^{\tau(E,z)}$ for various EBL models. The resulting intrinsic flux estimates are then refit with a differential power-law for the redshift lower limit (top) and 99% upper limit (bottom). The fitted intrinsic indices for both the lower and upper limits on redshift are summarized in Table 5.1. The hardest deabsorbed spectra result from the Finke et al. (2010) EBL model, but all fitted power-laws provide indices softer than the $\Gamma = 1.5$ limit (shown for reference in Figure 5.5 by the grey solid line at a comparable normalization to the deabsorbed spectra). The resulting indices are also below the *Fermi*-LAT measured index of Γ=1.8±0.1.

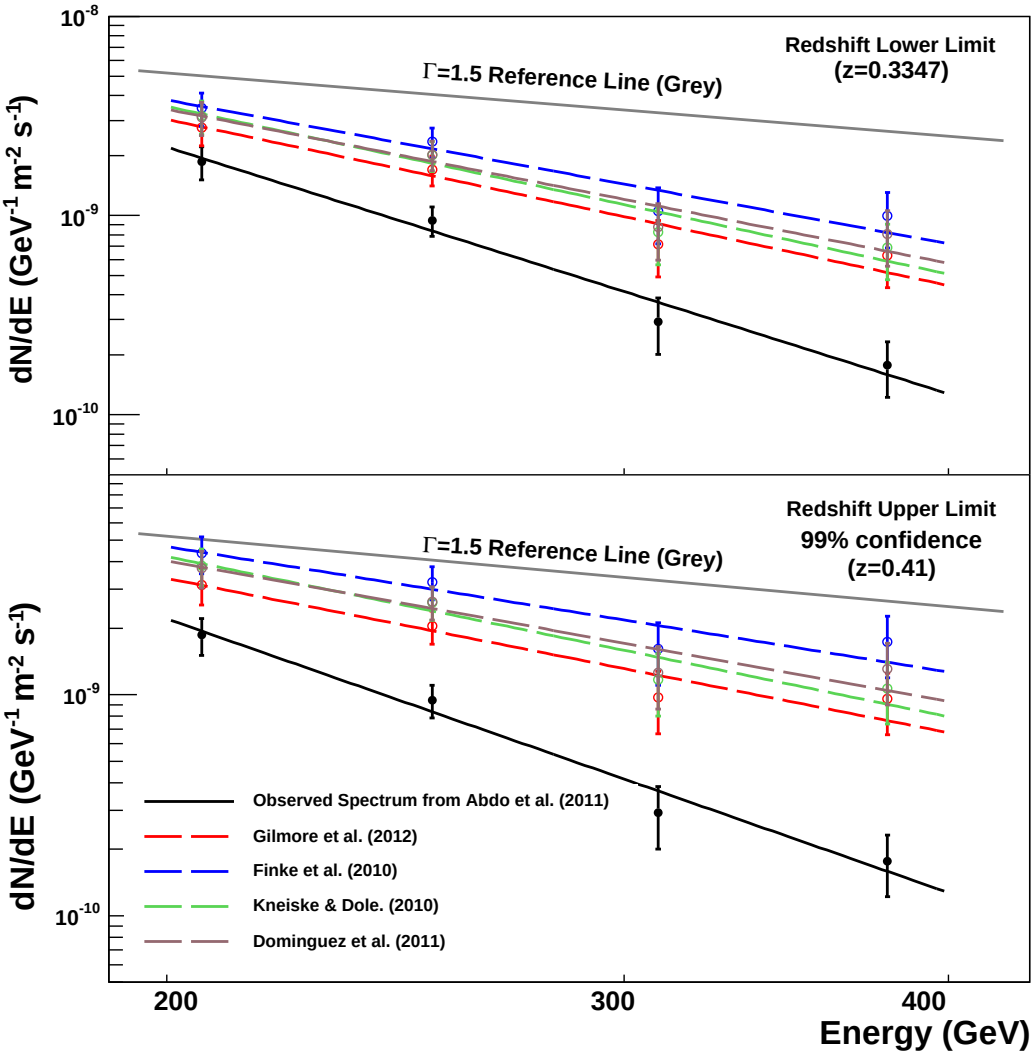

Figure 5.5: Deabsorbed spectra for 3C 66A for the $z_{\rm ll}$ of 0.3347 (top panel) and 99% confidence level $z_{\rm ul}$ of 0.41 (bottom panel), where the observed VHE spectrum (black solid line) is taken from Abdo et al. (2011), with an index of $\Gamma = 4.1 \pm 0.6_{stat}$ for the applied differential power-law of the form $dN/dE = (E/E_o)^{-\Gamma}$. For reference, a spectrum with an index of Γ=1.5 is shown as the theoretical limit for an intrinsic index, as explained in the text. The resulting indices for each redshift and model are summarized in Table 5.1.

5.4 Conclusion

Observation of the $z \sim 0$ Lyα forest in the direction of the 3C 66A with HST COS provides a direct lower and statistical upper redshift limit for the blazar. The detection of three clouds at $z_{\rm abs} \sim 0.3283$, 0.3333, and 0.3347 provide the $z = 0.3347$ lower limit on the blazar redshift. Assuming that the incidence of Lyman absorption systems is a Poisson distribution in z, we can conclude that the blazar is likely to lie $z_{\rm blazar} \leq 0.41$ (99% confidence level) and exclude a $z \geq 0.444$ at 99.9%.

Based on the assumption that the intrinsic index cannot be harder than $\Gamma = 1.5$, the redshift limits derived from the FUV observations do not place the blazar at a sufficient distance to utilize the observed VHE spectrum during an elevated state in October of 2009 to constrain the EBL density. Moreover, the distance is not sufficient to extract an upper limit on the EBL density based on the similar assumption that the intrinsic VHE index is not harder than the *Fermi* observed index.

Chapter 6

The Firm Redshift Lower Limit of the Most Distant TeV-Detected Blazar PKS 1424+240

This work has been published in the Astrophysical Journal Letters (*Furniss et al. 2013, ApJL, 768, 31*). The corresponding author of the work is Amy Furniss. No content was modified aside from necessary formatting. The full author list of this work can be found in Appendix E.

Abstract

We present the redshift lower limit of $z \geq 0.6035$ *for the very-high-energy (VHE;* $E \geq$*100 GeV) emitting blazar PKS 1424+240 (PG 1424+240). This limit is inferred from Lyman* β *and* γ *absorption observed in the far-ultraviolet spectra from the Hubble Space Telescope/Cosmic Origins Spectrograph. No VHE-detected blazar has shown solid spectroscopic evidence of being more distant. At this distance, VHE observations by VERITAS are shown to sample historically large gamma-ray opacity values at 500 GeV, extending beyond* τ*=4 for low-level models of the extragalactic background light (EBL) and beyond* τ *=5 for high-levels. The majority of the* $z = 0.6035$ *absorption-corrected VHE spectrum appears to exhibit a lower flux than an extrapolation of the contemporaneous LAT power-law fit beyond 100 GeV. However, the highest energy VERITAS point is the only point showing agreement with this extrapolation, possibly implying the overestimation of the gamma-ray opacity or the onset of an unexpected VHE spectral feature. A curved log parabola is favored when fitting the full range of gamma-ray data (0.5 to 500 GeV). While fitting the absorption-corrected VHE data alone results in a harder differential power law than that from the full range, the indices derived using three EBL models are consistent with the physically motivated limit set by Fermi acceleration processes.*

6.1 Introduction

Blazars are active galaxies with a jet closely aligned with the Earth line of sight (Urry & Padovani, 1995). These objects are the most commonly detected type of extragalactic source at very high energies (VHE; $E \geq$100 GeV). The VHE gamma rays which propagate through the intergalactic medium are absorbed by extragalactic background light (EBL) photons via pair production (Nikishov, 1962; Gould & Shréder, 1967). The EBL is difficult to directly measure due to strong foreground sources (Hauser & Dwek, 2001).

Various methods are used to estimate the density of the EBL. A selection of EBL models include a semi-analytical model (Gilmore et al., 2012), an observationally based model which utilizes observations of K-band rest frame galaxy luminosity functions in combination with galaxy spectral energy distribution fractions (Dominguez et al., 2011) and a model based on starlight emission and dust re-emission templates (Finke et al., 2010). Each of these estimate photon densities are above the lower limits set by galaxy counts (Werner et al. , 2004), and below the limits set by detection of extragalactic VHE photons (e.g., Aharonian et al. (2006)).

The interaction between VHE and EBL photons produces a "gamma-ray horizon," limiting the distance to which VHE sources can be detected. 3C 279 is the most distant VHE emitting blazar with a spectroscopically measured redshift. By

spectroscopically measured, we mean the detection of emission and/or absorption lines of the host galaxy. 3C 279 is a flat-spectrum radio quasar (FSRQ) at $z = 0.536$ (Marziani et al., 1996) and was observed above 50 GeV by MAGIC during a flare (Albert et al., 2008b).

FSRQs are blazars which show emission lines with an equivalent width of ≥ 5Å, providing strong host-galaxy emission and absorption for spectroscopic distance measurements. Conversely, BL Lacertae-type blazars display weak or no emission/absorption lines, and lack evidence for a Ca H+K break in their optical spectrum (Marcha et al., 1996; Healey et al., 2007). With this definition, it is not surprising that there are VHE-detected BL Lac objects that lack definite spectroscopic redshift measurements. Some notable VHE blazars without spectroscopic redshift are KUV 00311-1938, PG 1553+113, 3C 66A, S5 0716+714 and PKS 1424+240 (PG 1424+240).

KUV 00311-1938, detected at TeV energies by HESS (Becherini et al., 2012), has a tentative redshift of 0.61 from the observation of five features in a poor signal-to-noise ratio (SN) spectrum (Piranomante et al., 2007). Follow-up spectroscopy with improved SN did not confirm any $z = 0.61$ features, although an intervening Mg II absorption system at $z = 0.506$, not visible in the previous spectrum, was observed and sets a lower limit on the blazar distance (Pita et al., 2012).

Since BL Lac objects display bright and featureless spectra, strict lower limits

on the redshifts can be inferred through observation of far-UV (FUV) absorption by the low-z intergalactic medium (IGM). This method has been applied to PG 1553+113, 3C 66A, and S5 0716+714 showing lower limits of z =0.395, 0.3347 and 0.2314 (Danforth et al. (2010); Furniss et al. (2013a); Danforth et al. (2013a), respectively). We apply this technique to the VHE-detected blazar PKS 1424+240, constraining the blazar to $z \geq 0.6035$, making it the most distant VHE-detected blazar thus far.

6.2 Observations and Far-UV Spectral Analysis

PKS 1424+240 was observed under a *Hubble Space Telescope* (HST) program (12612, PI: Stocke) which uses flaring blazars as probes of intervening, weak IGM absorption. PKS 1424+240 is one of $\sim$ 200 objects monitored by a network of automated telescopes: the Katzman Automatic Imaging Telescope (KAIT, Filippenko et al. (2001)), the "NF/ Observatory" (Grauer et al., 2008) and the Small and Moderate-Aperture Remote Telescope System (SMARTS, Bonning et al. (2012)). Optical photometry in April of 2012 indicated that PKS 1424+240 was sufficiently bright to trigger a five-orbit HST/COS observation.

The blazar was observed on 19 April 2012, with the medium resolution ($\Delta v \approx$ 18 km s^{-1}), far-UV gratings G130M (1135 $< \lambda <$ 1450 Å, 6.4 ksec) and G160M (1400 $< \lambda <$ 1795 Å, 7.9 ksec). The flux-calibrated, one-dimensional spectra were

obtained from the Mikulski Archive for Space Telescopes and combined with the standard IDL procedures described in Danforth et al. (2010). Additional analysis details are given in Danforth et al. (2013b). The combined data show a continuum flux level of $\sim 1.4 \times 10^{-14}$ erg cm^{-2} s^{-1} Å^{-1} and a median SN per 7-pixel resolution element of ~ 19 over the entire spectrum. The spectrum was normalized with an iterative, spline-based procedure and an automated line-finding algorithm was used to locate $> 4\sigma$ absorption features (Danforth et al., 2013b).

We set a firm, observational lower limit to the source redshift by examining intervening absorbers. We see absorption consistent with higher-order H I Lyman absorption at $z \approx 0.6$ (Figure 6.1). The presence of absorption profiles consistent with Lyβ and Lyγ at three distinct redshifts provides unambiguous line identifications of absorbing gas along the line of sight (Table 6.1). The measurements summarized in Table 1 are made using Voigt-profile fits to the lines. The significance levels are calculated from the observed equivalent widths and flux errors and are calculated via the methods described in Keeney et al. (2012). The line identifications are bolstered in two cases by low-significance Lyδ detections.

In other cases where H I absorption is used to constrain blazar distance, the *lack* of absorbers past a certain redshift is used to place a statistical upper limit.

[1]Rest-frame equivalent width.
[2]Doppler parameter.
[3]Corresponding column density.
[4]Significance of line (according to Keeney et al. (2012)).

Table 6.1: Intervening Lyman Absorption Lines

Line	$\lambda_{\rm obs}$ (Å)	$W_{\rm r}$ (mÅ)[1]	b (km s^{-1})[2]	log N (cm^{-2})[3]	S.L. (σ)[4]
Lyβ	1624.6	89 ± 29	47 ± 7	14.18 ± 0.12	6
Lyγ	1540.2	73 ± 5	55 ± 8	14.52 ± 0.04	5
Lyβ	1637.1	180 ± 1	44 ± 3	14.52 ± 0.02	11
Lyγ	1552.1	60 ± 33	37 ± 5	14.44 ± 0.19	5
Lyδ	1515.7	19 ± 6	31 ± 5	14.3 ± 0.2	~ 2
Lyβ	1644.8	70 ± 11	14 ± 2	14.15 ± 0.06	7
Lyγ	1559.5	36 ± 10	15 ± 3	14.25 ± 0.08	4
Lyδ	1522.9	13:	10:	14.1 ± 0.3	~ 2

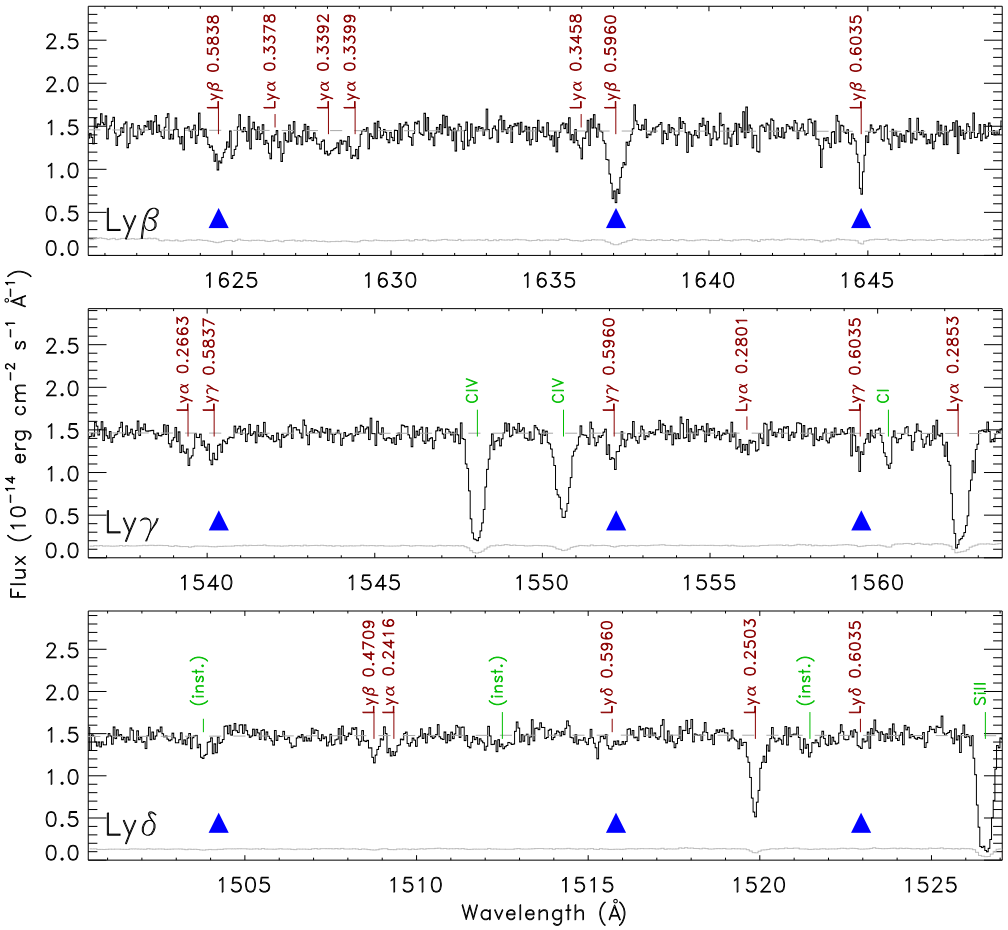

Figure 6.1: COS spectra show intervening absorption systems at $z = 0.5838$, $z = 0.5960$, and $z = 0.6035$ (arrows) toward PKS 1424+240 in Lyβ (1025.72Å), Lyγ (972.54 Å), and Lyδ (949.74 Å). COS flux and error (grey) vectors are binned by four pixels (about half a resolution element). Continuum fit is shown with dashed line. Other intervening absorption is identified with species and redshift in red. Galactic ($v \approx 0$) absorption and instrumental features are labeled in green.

For PKS 1424+240, the Lyα forest extends to the red end of the FUV detector ($\sim$ 1800 Å, $z = 0.47$). Absorbers at higher redshift are detected through paired Lyβ and Lyγ lines visible at $z < 0.75$. However this technique is less sensitive to H I absorbers than detection via Lyα since both Lyβ *and* Lyγ lines must be detected to unambiguously identify an absorber and $(f\,\lambda)_{\mathrm{Ly}\gamma}$ is only $\sim 5\%$ that of Lyα.

No H I absorbers are seen between the reddest system ($z = 0.6035$) and the red edge of the detector in Lyβ ($z = 0.75$) for a line-free path length $\Delta z = 0.15$. The spectral data quality is such that we should detect lines at $\mathrm{Log}\, N_{\mathrm{H\ I}} \geq 14.0$ ($W_{\mathrm{Ly}\beta} \geq 60$ mÅ, $W_{\mathrm{Ly}\gamma} \geq 20$mÅ) at a 4σ level. The frequency of lines of this strength or higher at low redshift is $dN/dz \approx 24$ (Danforth & Shull, 2008), so we would expect $N = 3.5^{+3.1}_{-1.8}$ absorbers to be present if the source were at $z > 0.75$. Since no lines are seen, we can rule out $z > 0.75$ at approximately 2σ confidence. More detailed simulations may refine the redshift upper limit, but near-UV spectra and a direct search for Lyα lines at $z \sim 1$ will be less ambiguous.

The redshift lower limit is significantly higher than the conservative estimates of $z \geq 0.06$ (Scarpa et al., 1995) and $z = 0.23$ (Meisner & Romani, 2010), derived from host-galaxy assumptions. Notably, the redshift estimates in Meisner & Romani (2010) are in close agreement with other blazar distance limits derived from the observation of absorption systems. The redshift limit for PKS 1424+240

is also below the upper limits of $z = 0.66$ and 1.19 derived from correcting VHE observations for EBL absorption to match the *Fermi* Large Area Telescope (LAT) data in Acciari et al. (2010) and Yang & Wang (2010), respectively.

6.3 Absorption of Very High Energy Photons

The energy- and redshift-dependent absorption of VHE gamma rays by the EBL can be estimated using the model-specific optical depth, $\tau(E, z)$, where the absorption-corrected (deabsorbed) flux, F_{cor}, can be estimated from the observed flux, F_{obs}, using the relation $F_{cor} = F_{obs} \times e^{\tau(E,z)}$. We investigate the deabsorbed VHE spectrum of PKS 1424+240 at the redshift lower limit of $z = 0.6035$, using three EBL models to explore the effect of relatively low, medium, and high levels of EBL photon density. The lowest density EBL model used is from Gilmore et al. (2012), which estimates a $z \sim 0$ EBL spectral energy distribution nearing the required lower limits on the EBL density set by galaxy counts. We use the Dominguez et al. (2011) model to estimate VHE absorption by a intermediate level EBL density and the Finke et al. (2010) model to represent a relatively high level of EBL density.

6.3.1 Constraining the Opacity of the EBL

The blazar VHE spectral index can be used to estimate the EBL spectral properties under the assumption that the intrinsic spectrum, characterized by the power-law $dN/dE \propto E^{-\Gamma}$, cannot be harder than $\Gamma = 1.5$, as described in Aharonian et al. (2006). The limit is physically motivated by the shock acceleration paradigm, where the hardest index obtained for the accelerated leptons is 1.5.

Notably, the hardest blazar spectral index measured by the LAT has an index of 1.1 but is in statistical agreement with the theoretical limit (Ackermann et al., 2011; Nolan et al., 2012). Since the LAT is most sensitive to photons at energies where EBL absorption is negligible, the indices derived from LAT observations reflect the intrinsically emitted gamma-ray spectrum. A more conservative limit equal to the LAT measured index can be placed under the assumption that blazars do not harden with increasing energy. For PKS 1424+240, the contemporaneous LAT-measured index is 1.80±0.07 (Acciari et al., 2010) (Figure 6.3).

A power-law fit can be applied to the absorption-corrected points for the redshift lower limit of $z = 0.6035$, as summarized in Table 6.2 for each of the EBL models. The fitted indices for the deabsorbed spectra using the relatively low and medium EBL models (Gilmore et al. (2012) and Dominguez et al. (2011), respectively) are well within the Γ=1.5 and $\Gamma = 1.80 \pm 0.07$ limits. However, the $\Gamma = 0.6 \pm 0.8$ index resulting from deabsorption with the relatively more opaque

model from Finke et al. (2010) is below, but still consistent with, either of the expectations. Improved gamma-ray observations may reveal that this model is too dense. Other explanations, such as time-dependent stochastic accelerated inverse-Compton scenarios (Lefa et al., 2011a,b) and internal gamma-gamma absorption (Aharonian et al., 2008), can also account for unusually hard VHE emission spectra.

Table 6.2: Fitting results for the power-law fit (4 degrees of freedom; DOF) to the absorption-corrected VHE points from Acciari et al. (2010). Additionally, we show the fits to the full range of data (0.5-500 GeV) for a differential power law ($dN/dE \propto (E/E_o)^{-\Gamma}$, 9 DOF) and log parabola ($dN/dE \propto (E/E_o)^{-\Gamma-\beta \mathrm{Log}(E)}$, 8 DOF). The fits for the Dominguez et al. (2011) model are shown in Figure 6.3 in blue dashed and dotted lines, respectively.

EBL Model Used	**VHE Range Deabsorbed Power-law Index** Γ	χ^2	**Full Range Deabsorbed Power-law Index** Γ	χ^2	**Full Range Deabsorbed Log-parabola Index** Γ	**Full Range Deabsorbed Log-parabola Curvature** β	χ^2
Gilmore et al. (2012)	1.5±0.8	3.4	2.07±0.03	20.4	2.04±0.04	0.10±0.03	11.3
Dominguez et al. (2011)	1.0±0.7	3.5	2.01±0.03	18.4	1.99±0.04	0.08±0.03	11.8
Finke et al. (2010)	0.6±0.8	3.3	1.97±0.04	17.0	1.96±0.04	0.07±0.03	11.8

6.3.2 The Gamma-ray Horizon

Intergalactic gamma-ray opacity due to the EBL has direct consequences for the estimation of the intrinsic gamma-ray spectra of extragalactic VHE targets, with the source emitted flux being suppressed by $e^{-\tau(E,z)}$. This energy- and redshift-dependent flux suppression requires sources to be exponentially brighter at larger distances in order to be detectable at VHE.

The opacities probed through the VHE observation of blazars with redshift information provides insight into the possibility of a pair-production anomaly, as investigated in Horns & Meyer (2012). In the seven VHE blazar spectra which probe opacities in the range $1 \leq \tau \leq 2$, an upturn of the absorption-corrected spectra is apparent with a significance of 4.2σ at the $\tau \geq 2$ transition energy. Due to the different energies of the $\tau \geq 2$ transition for the blazars studied, source-intrinsic features are an unlikely explanation.This study was limited by the number of VHE blazars probing opacities $\tau \geq 2$ with known redshift. PKS 1424+240 can now be included in the study, expanding the limited opacity parameter space available.

Before the determination of the redshift lower limit of PKS 1424+240, the highest sampled gamma-ray optical depth probed was associated with the detection of 3C 279 during an elevated state, probing a $\tau(\mathrm{E} = 475\,\mathrm{GeV}, z = 0.536) = 3.2$, 3.9 or 4.3 when estimated with the Gilmore et al. (2012); Dominguez et al. (2011);

Finke et al. (2010) models, respectively. Now, with PKS 1424+240, the highest opacity sampled is between 4.1 and 5.3 (if estimated with the Gilmore et al. (2012) and Finke et al. (2010) models, respectively.)

We show the highest opacity sampled by the VHE detection of 3C 279 compared to the opacity probed with the detection of PKS 1424+240 in Figure 6.2, as derived for the Dominguez et al. (2011) model. The spectral points are plotted along with the $\tau(E, z) = 1 - 5$ horizons. For reference, we also show published spectral points of every VHE-detected blazar with a spectroscopically measured redshift above 0.2 (four sources, as compared to the more than 30 VHE blazars with $z < 0.2$). Since the redshift of PKS 1424+240 represents a lower limit, the maximum opacity sampled by the VHE detection is illustrated with a right-pointing arrow.

6.4 Absorption-Corrected Gamma-ray Emission

The observed gamma-ray peak is reproduced from Acciari et al. (2010) in Figure 6.3, illustrating the contemporaneous LAT and VERITAS data with black squares and circles, respectively. Additionally, we correct the observed VHE spectrum for EBL absorption at the minimum redshift of $z = 0.6035$ using the intermediate model (Dominguez et al., 2011), illustrated by grey circular points. Absorption of the LAT data is negligible.

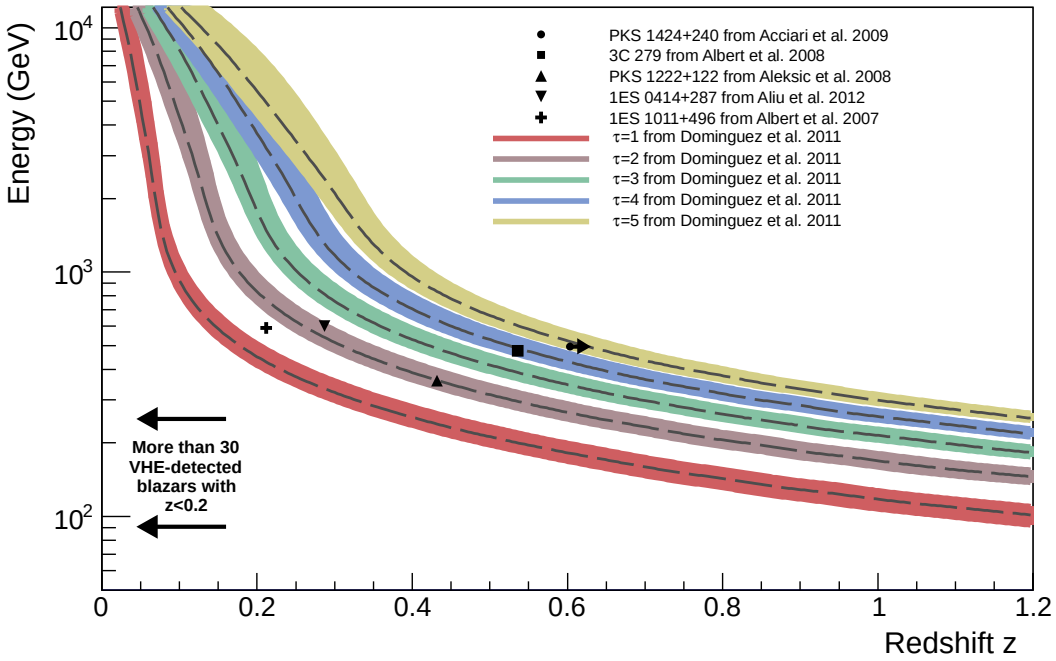

Figure 6.2: The highest energy points of all VHE detected blazars with published VHE data and spectroscopic redshifts beyond 0.2. There are only five spectroscopically measured blazars with published VHE data which reside beyond $z = 0.2$, as compared to the more than 30 at $z < 0.2$. The close proximity of the majority of VHE blazars is a direct result of the gamma-ray opacity of the Universe. The $\tau = 1 - 5$ gamma-ray horizon contours are shown as bands, including the errors from the model, representing the energy and redshift dependent $e^{-\tau}$ suppression of the VHE flux for extragalactic sources as calculated from Dominguez et al. (2011, 2013). The VHE detection of PKS 1424+240 is shown with a rightward arrow, indicating that the redshift $z = 0.6035$ is a lower limit.

The LAT and VERITAS gamma-ray observations extend from 0.5 to 500 GeV. This full range, when corrected for EBL absorption at $z = 0.6035$, is not well fit with a power law (dashed blue line), while a curved log parabola provides an improved fit (dotted blue line). We note than neither the power-law nor the log-parabolic fit represents the data well. The fit results for each EBL model are summarized in Table 6.2. Both the power-law and log-parabolic fits find indices of $\Gamma \sim 2$, with a significantly curved log-parabolic fit. Notably, the highest energy VERITAS point at 500 GeV appears to deviate from the fits, matching the LAT extrapolated power-law (red dashed line). This deviation is not expected by standard blazar emission models, but is only about two standard deviations at the redshift lower limit.

A break between the LAT and VERITAS absorption-corrected data is apparent. This discrepancy is not likely an issue of instrumental cross-calibration, as agreement between VERITAS and LAT observations have been found for other contemporaneous blazar observations (e.g., Aliu et al. (2011a, 2012a)). A portion of this feature may be due to a small level of undetected variability. Although short intervals of variability are difficult to rule out, no long-term variability is detected (Acciari et al., 2010), making it unlikely that the spectral feature between the LAT and VERITAS instruments is due to variability alone.

Since $z = 0.6035$ is a lower limit, it is conceivable that the discontinuity

between the LAT and VERITAS data may, in fact, be an unphysical effect arising from the incomplete correction for absorption by the EBL. The first differential flux point of the VHE spectrum at 150 GeV cannot be made to match the LAT extrapolated spectrum without deabsorbing the flux for a redshift of 1.2 (blue stars in Figure 6.3). This deabsorbed spectrum is shown for the Dominguez et al. (2011) model, but is representative of the required distances of $z = 1.5$ and $z = 1.0$ when corrected with the Gilmore et al. (2012) and Finke et al. (2010) models, respectively.

The $z = 1.2$ corrected VHE spectrum results in a *rising* slope, i.e. with an index $\Gamma = -2.5 \pm 1.0$ when fit with a differential power law. A VHE spectrum with a rising power law is difficult to produce in even the most extreme emission scenarios. Although this redshift value is still in agreement with the redshift upper limit set by Yang & Wang (2010), we interpret the unphysical VHE spectrum as evidence that the blazar does not reside at this distance.

6.4.1 Possible Signature of Intrinsic Gamma-ray Absorption

Assuming that the blazar resides near $z = 0.6035$, the apparent discontinuity between the LAT and VERITAS energy ranges may be due to gamma-ray absorption in the vicinity of the blazar. It has been shown that absorption of gamma-

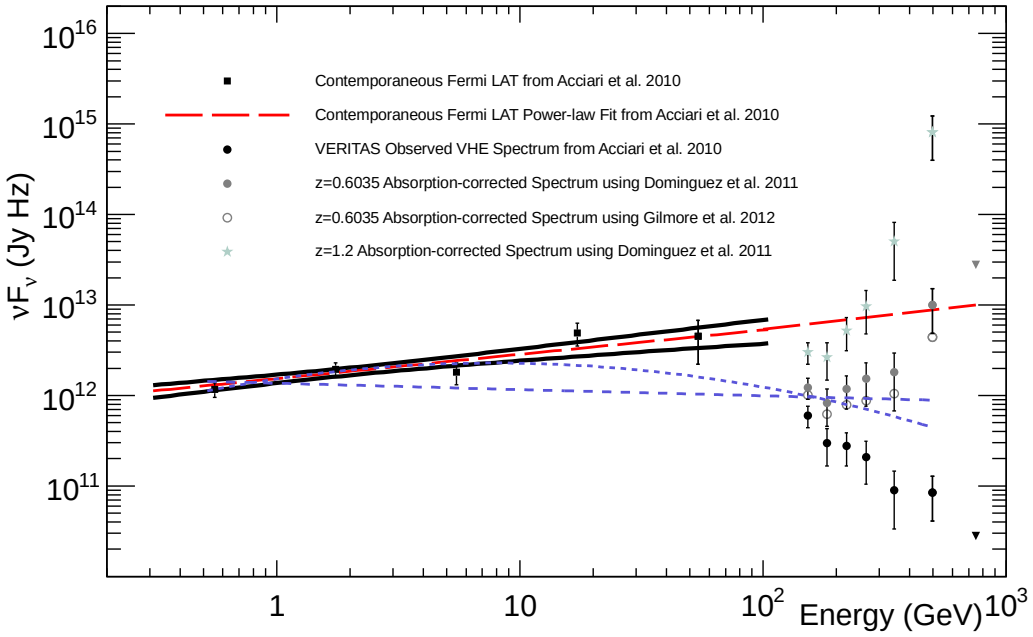

Figure 6.3: The gamma-ray peak of the spectral energy distribution of PKS 1424+240, with *Fermi* LAT (squares and power-law fit contour) and VERITAS observations (black circles) taken from Acciari et al. (2010). An upper limit at 750 GeV is shown with a downward pointing arrow. The LAT data have been selected to be contemporaneous with the VERITAS observations. The absorption-corrected VHE spectrum is shown with the grey circles, using opacities from the Dominguez et al. (2011) EBL model. For references, the absorption-corrected points using the Gilmore et al. (2012) model are shown in open circles. The *Fermi* LAT power-law fit has been extrapolated up to VHE (dashed red line). Power-law and log-parabolic fits to the full range (0.5-500 GeV) are shown in the blue dashed and dotted lines, respectively, with fitting results in Table 6.2. To bring the first absorption-corrected VERITAS spectral point to match the *Fermi* observed spectrum, the blazar needs to be corrected for absorption expected for $z \approx 1.2$, shown by blue stars (the upper limit for this deabsorption is off-scale).

rays by a broad line region (BLR) can produce broken power-law spectra in bright LAT-detected blazars (Poutanen & Stern, 2010). However, this type of absorption is not immediately expected for an intermediate/high-synchrotron-peaked source such as PKS 1424+240, expected to exhibit a clean radiation environment (Böttcher & Dermer, 2002; Ghisellini & Tavecchio, 2008).

The absorption-corrected VHE point at 500 GeV matches the LAT power-law extrapolation, with a distinct mismatch to the 100 through 400 GeV points. A source of gamma-ray opacity that is only sensitive to photons between 100 GeV and ∼400 GeV is difficult to explain with an ion continuum such as that present in a BLR. It has been shown that the optical depth of a BLR containing UV-continuum and ionization lines produces a constant optical depth from tens of GeV to beyond 30 TeV (Tavecchio & Mazin, 2009). Since PKS 1424+240 is not expected to harbor a BLR, it is perhaps more likely that the EBL model is slightly overcorrecting for the photon absorption around 500 GeV. The observed hard spectrum might also be explained by secondary gamma rays produced in cosmic-ray interactions along the line of sight (Essey & Warren, 2012; Aharonian et al., 2013).

6.5 Conclusions

We present the strict redshift lower limit of $z \geq 0.6035$ for PKS 1424+240, set by the detection of Lyβ and γ lines from intervening hydrogen clouds. This lower limit makes PKS 1424+240 the most distant VHE-detected source. At this distance, VHE observations of the source out to energies of 500 GeV probe gamma-ray opacities of up to $\tau \sim 5$.

An investigation of possible constraint on the opacity of the EBL shows that the absorption-corrected power-law fits do not lie significantly outside of the standard spectral limitations. However, deabsorption with the Finke et al. (2010) model produces the hardest intrinsic VHE spectrum. If the blazar resides at a redshift beyond the lower limit, the deabsorbed indices may become constraining to even the lowest level EBL model.

This redshift information allows the investigation of the EBL absorption-corrected gamma-ray emission. Correcting the VHE spectrum for the minimum redshift of $z = 0.6035$ shows an unexpected spectral shape. The elevated flux around 500 GeV, while not high significance, may be due to an overcorrection of absorption by the EBL model. This feature is still present when using the Gilmore et al. (2012) model (open circles in Figure 6.3), which predicts a low EBL density and therefore might be evidence for a pair-production anomaly, such as might occur if VHE photons mixed with axion-like particles.

The spectral feature occurring between the LAT and VERITAS energy bands cannot be reasonably removed by correcting for additional absorption due to a larger distance. Instead, deabsorption for a higher redshift to match the LAT and VERITAS fluxes results in a non-physical spectrum and an extreme distance of $z = 1.2$. It is possible, although unlikely, that the EBL absorption-corrected gamma-ray spectrum of PKS 1424+240 is exhibiting gamma-ray absorption within an intrinsic photon field such as a BLR. As the most distant VHE BL Lac object, probing historically high values of gamma-ray opacity, this source requires additional gamma ray observations and a tighter constraint on the redshift to further investigate the intrinsic emission.

Part III

Conclusions: Striving for a Complete View

"Measure what can be measured, and make measureable what cannot be measured."

– Galileo Galilei (1564 - 1642)

Despite decades of scrutiny, the nature of the relativistic particles within blazar jets largely remain a mystery. As summarized in this work, a common technique used to investigate the extreme processes within blazar jets is the application of non-thermal broadband emission models. Unfortunately, studies and conclusions drawn from the modeling of blazar broadband emission can be compromised by the lack of critical parameter constraints. It is common to apply these models without experimental evidence for the identity of the emitting particles, the size and/or density of the emission region, the intrinsic energy spectrum of the relativistic particles and/or the distance to the blazar. The realistic modeling of the large parameter space is further complicated by the absence of strictly simultaneous broadband datasets for gamma-ray blazars, targets which have been seen to vary significantly on minute timescales.

More recently, the lack of parameter constraints and the need for simultaneous broadband observations has been driving the development of new observing strategies. Connections between astronomical bands, both theoretical and observational, are providing the means to overcome the critical shortcomings of historical broadband blazar studies.

The use of the *Fermi* LAT observations for the selection of candidate VHE emitting blazars is a prime example of multi-band collaboration, helping to provide an expanded population of VHE blazars available for study. Additionally, the study of previously unavailable information such as relativistic particle population energetics and environmental characteristics through the search for signatures of X-ray absorption may become a viable method for constraining the relativistic emission from blazars. These efforts can be supplemented by the collection of contemporaneous broadband observations of VHE blazars, enabling a more accurate emission model application.

The techniques mentioned in this work allow a more complete view of the intrinsic processes at work within VHE blazars, a necessity when using VHE blazars as cosmological probes of the extragalactic background light. An accurate understanding of blazar emission, paired with knowledge of the blazar distance can provide the means to sample the signature of the EBL absorption of VHE photons. As described in this work, collecting spectroscopic redshift measurements for VHE

emitting blazars can be challenging due to the featureless spectra. In the absence of detectable host galaxy spectral features, indirect blazar distance limits can be obtained with far-UV observations of intervening Lyman absorption systems in the blazar direction.

The new insight derived from broadband observations of distant blazars can be used to test the viability of the available EBL models and is motivating the consideration of non-standard scenarios for relativistic particle emission and pair-production processes. More specifically, the VHE detection of a blazar more distant than any previous VHE source has revealed unexpected spectral characteristics in the gamma-ray emission from the blazar, bringing widely accepted blazar emission paradigms into question. Additionally, the intrinsic gamma-ray emission from this distant blazar is might suggest the possibility of an exotic theory of anomalous pair-production (Meyer et al., 2011).

As more complete broadband datasets for these extreme sources are collected, we are coming to realize that they are more complicated than we have come to believe from looking at biased, incomplete data. Blazars are now known to display SEDs which are not easily described by currently available non-thermal emission mechanisms. With the new targets and methods presented here, we have the tools to help unravel the puzzles of these extraordinary accretion driven processes as well as the density of the extragalactic background light and whether anomalous

particle interactions play a role.

Continued VHE blazar studies will be enhanced through the collection of additional data, including the broadband study of VHE blazars at redshifts beyond historical distance boundaries. Fortunately, the collection of contemporaneous broadband observations has become the norm for blazar studies and is benefiting from the wide array of sensitive instruments.

Aside from VERITAS and *Fermi* in the gamma-ray regimes, *NuStar* and *Swift* X-ray telescopes and various robotic optical telescopes also provide opportunities for simultaneous observations. These instruments will be joined by the most sensitive arrays at both ends of the energy range.

The millimeter instrument Atacama Large Millimeter Array (ALMA) is already in partial operation and will be an array of antennas acting as a single telescope of revolutionary design. This instrument is an imaging instrument which is sensitive to all atomospheric windows between 350 micrometers and 10 millimeters. When completed, the array will be composed of 66 high precision antennas, located on a plateau in northern Chile 5000 meters above sea level. The sensitivity is estimated to be more than 20 times that of the Very Large Array, with a spatial resolution of 10 milliarcseconds (ten times better than the Very Large Array and five times that of *HST*) [5].

On the opposite extreme of the electromagnetic spectrum, the gamma-ray

[5] `www.almaobservatory.org`

band will be made more accessible through the Cherenkov Telescope Array (CTA), an innovative instrument in the process of prototype testing. There are plans to build two arrays, one in each of the northern and sourthern hemispheres to allow for a full view of the sky. A possible design scenario for the northern hemisphere array consists of three types of telescopes with different mirror sizes in order to cover a wider energy range. The combination of low, medium and high energy instruments would allow sensitivity between a few tens of GeV through more than 100 TeV with a factor of ten more sensitivity than any existing VHE gamma-ray array. For the first time in this band, the observatory will be open to the astrophysics community, providing a public view into the non-thermal high-energy universe[6].

The unprecedented sensitivities of ALMA and CTA will provide a deeper view of the cosmological formation history of the Universe and most extreme processes through the study of VHE blazars. With the capabilities of current and upcoming instruments, we can rest assured that the science is entering a revolutionary period of exciting discovery.

[6] www.cta-observatory.org

Appendix A

Full Author List for ApJ 742, 127 (2011)

E. Aliu[1], T. Aune[2], M. Beilicke[3], W. Benbow[4], M. Böttcher[5], A. Bouvier[2], S. M. Bradbury[6], J. H. Buckley[3], V. Bugaev[3], A. Cannon[7], A. Cesarini[8], L. Ciupik[9], M. P. Connolly[8], W. Cui[10], G. Decerprit[11], R. Dickherber[3], C. Duke[12], M. Errando[1], A. Falcone[13], Q. Feng[10], G. Finnegan[14], L. Fortson[15], A. Furniss[2,0], N. Galante[4], D. Gall[16], G. H. Gillanders[8], S. Godambe[14], S. Griffin[17], J. Grube[9], G. Gyuk[9], D. Hanna[17], B. Hivick[5], J. Holder[18], H. Huan[19], G. Hughes[11], C. M. Hui[14], T. B. Humensky[19], P. Kaaret[16], N. Karlsson[15], M. Kertzman[20], D. Kieda[14], H. Krawczynski[3], F. Krennrich[21], G. Maier[11], P. Majumdar[22], S. McArthur[3], A. McCann[17], P. Moriarty[23], R. Mukherjee[1], T. Nelson[30], R. A. Ong[22], M. Orr[21], A. N. Otte[2],

N. Park[19], J. S. Perkins[24,25], A. Pichel[26], M. Pohl[27,11], H. Prokoph[11], J. Quinn[7], K. Ragan[17], L. C. Reyes[19], P. T. Reynolds[28], E. Roache[4], H. J. Rose[6], J. Ruppel[27,11], D. B. Saxon[18], G. H. Sembroski[10], C. Skole[11], A. W. Smith[29], D. Staszak[17], G. Tesić[17], M. Theiling[4], S. Thibadeau[3], K. Tsurusaki[16], J. Tyler[17], A. Varlotta[10], V. V. Vassiliev[22], S. P. Wakely[19], T. C. Weekes[4], A. Weinstein[21], D. A. Williams[2],

B. Zitzer[10] S. Ciprini[33], M. Fumagalli[31,0], K. Kaplan[4], D. Paneque[34,0], J. X. Prochaska[32]

[0]Corresponding authors: A. Furniss: afurniss@ucsc.edu, D. Paneque: dpaneque@mppmu.mpg.de, M. Fumagalli: miki@ucolick.org

[1]Department of Physics and Astronomy, Barnard College, Columbia University, NY 10027, USA

[2]Santa Cruz Institute for Particle Physics and Department of Physics, University of California, Santa Cruz, CA 95064, USA

[3]Department of Physics, Washington University, St. Louis, MO 63130, USA

[4]Fred Lawrence Whipple Observatory, Harvard-Smithsonian Center for Astrophysics, Amado, AZ 85645, USA

[5]Astrophysical Institute, Department of Physics and Astronomy, Ohio University, Athens, OH 45701, USA

[6]School of Physics and Astronomy, University of Leeds, Leeds, LS2 9JT, UK

[7]School of Physics, University College Dublin, Belfield, Dublin 4, Ireland

[8]School of Physics, National University of Ireland Galway, University Road, Galway, Ireland

[9]Astronomy Department, Adler Planetarium and Astronomy Museum, Chicago, IL 60605, USA

[10]Department of Physics, Purdue University, West Lafayette, IN 47907, USA

[11]DESY, Platanenallee 6, 15738 Zeuthen, Germany

[12]Department of Physics, Grinnell College, Grinnell, IA 50112-1690, USA

[13]Department of Astronomy and Astrophysics, 525 Davey Lab, Pennsylvania State University, University Park, PA 16802, USA

[14]Department of Physics and Astronomy, University of Utah, Salt Lake City, UT 84112, USA

[15]School of Physics and Astronomy, University of Minnesota, Minneapolis, MN 55455, USA

[16]Department of Physics and Astronomy, University of Iowa, Van Allen Hall, Iowa City, IA 52242, USA

[17]Physics Department, McGill University, Montreal, QC H3A 2T8, Canada

[18]Department of Physics and Astronomy and the Bartol Research Institute, University of Delaware, Newark, DE 19716, USA

[19]Enrico Fermi Institute, University of Chicago, Chicago, IL 60637, USA

[20]Department of Physics and Astronomy, DePauw University, Greencastle, IN 46135-0037, USA

[21]Department of Physics and Astronomy, Iowa State University, Ames, IA 50011, USA

[22]Department of Physics and Astronomy, University of California, Los Angeles, CA 90095, USA

[23]Department of Life and Physical Sciences, Galway-Mayo Institute of Technology, Dublin Road, Galway, Ireland

[24]CRESST and Astroparticle Physics Laboratory NASA/GSFC, Greenbelt, MD 20771, USA.

[25]University of Maryland, Baltimore County, 1000 Hilltop Circle, Baltimore, MD 21250, USA.

[26]Instituto de Astronomia y Fisica del Espacio, Casilla de Correo 67 - Sucursal 28, (C1428ZAA) Ciudad Autnoma de Buenos Aires, Argentina

[27]Institut für Physik und Astronomie, Universität Potsdam, 14476 Potsdam-Golm,Germany

[28]Department of Applied Physics and Instrumentation, Cork Institute of Technology, Bishopstown, Cork, Ireland

[29]Argonne National Laboratory, 9700 S. Cass Avenue, Argonne, IL 60439, USA

[30]School of Physics and Astronomy, University of Minnesota, 116 Church St. SE, Minneapolis, MN 55455, USA

[31]Department of Astronomy and Astrophysics, University of California, 1156 High Street, Santa Cruz, CA 95064

[32]Department of Astronomy and Astrophysics, UCO/Lick Observatory, University of California, 1156 High Street, Santa Cruz, CA 95064
[33]Dipartimento di Fisica, Università degli Studi di Perugia, I-06123 Perugia, Italy
[34]Max-Planck-Institut für Physik, D-80805 München, Germany

Appendix B

Full Author List for ApJ 759, 102 (2012)

E. Aliu[1], S. Archambault[2], T. Arlen[3], T. Aune[4], M. Beilicke[5], W. Benbow[6], M. Böttcher[33], A. Bouvier[4], J. H. Buckley[5], V. Bugaev[5], A. Cesarini[7], L. Ciupik[8], E. Collins-Hughes[9], M. P. Connolly[7], W. Cui[10], R. Dickherber[5], C. Duke[11], J. Dumm[12], M. Errando[1], A. Falcone[13], S. Federici[14,15], Q. Feng[10], J. P. Finley[10], G. Finnegan[16], L. Fortson[12], A. Furniss[4,0], N. Galante[6], D. Gall[17], S. Godambe[16], S. Griffin[2], J. Grube[8], G. Gyuk[8], D. Hanna[2], J. Holder[18], H. Huan[19], P. Kaaret[17], N. Karlsson[12], Y. Khassen[9], D. Kieda[16], H. Krawczynski[5], F. Krennrich[20], K. Lee[5], A. S Madhavan[20], G. Maier[14], P. Majumdar[3], S. McArthur[5], A. McCann[21], P. Moriarty[22], R. Mukherjee[1], T. Nelson[12], A. O'Faoláin de Bhróithe[9], R. A. Ong[3], M. Orr[20],

A. N. Otte[23], N. Park[19], J. S. Perkins[24,25], A. Pichel[26], M. Pohl[15,14], H. Prokoph[14], J. Quinn[9], K. Ragan[2], L. C. Reyes[27], P. T. Reynolds[28], E. Roache[6], D. B. Saxon[18], G. H. Sembroski[10], D. Staszak[2], I. Telezhinsky[15,14], G. Tešić[2], M. Theiling[10], S. Thibadeau[5], K. Tsurusaki[17], A. Varlotta[10], V. V. Vassiliev[3], S. Vincent[14], M. Vivier[18], S. P. Wakely[19], T. C. Weekes[6], A. Weinstein[20], R. Welsing[14], D. A. Williams[4],

B. Zitzer[29], P. Fortin[6,0], D. Horan[30,0], M. Fumagalli[31], K. Kaplan[31] and J. X. Prochaska[32]

[0]Corresponding authors: A. Furniss: afurniss@ucsc.edu, P. Fortin: pafortin@cfa.harvard.edu, D. Horan: deirdre@llr.in2p3.fr

[1]Department of Physics and Astronomy, Barnard College, Columbia University, NY 10027, USA

[2]Physics Department, McGill University, Montreal, QC H3A 2T8, Canada

[3]Department of Physics and Astronomy, University of California, Los Angeles, CA 90095, USA

[4]Santa Cruz Institute for Particle Physics and Department of Physics, University of California, Santa Cruz, CA 95064, USA

[5]Department of Physics, Washington University, St. Louis, MO 63130, USA

[6]Fred Lawrence Whipple Observatory, Harvard-Smithsonian Center for Astrophysics, Amado, AZ 85645, USA

[7]School of Physics, National University of Ireland Galway, University Road, Galway, Ireland

[8]Astronomy Department, Adler Planetarium and Astronomy Museum, Chicago, IL 60605, USA

[9]School of Physics, University College Dublin, Belfield, Dublin 4, Ireland

[10]Department of Physics, Purdue University, West Lafayette, IN 47907, USA

[11]Department of Physics, Grinnell College, Grinnell, IA 50112-1690, USA

[12]School of Physics and Astronomy, University of Minnesota, Minneapolis, MN 55455, USA

[13]Department of Astronomy and Astrophysics, 525 Davey Lab, Pennsylvania State University, University Park, PA 16802, USA

[14]DESY, Platanenallee 6, 15738 Zeuthen, Germany

[15]Institute of Physics and Astronomy, University of Potsdam, 14476 Potsdam-Golm, Germany

[16]Department of Physics and Astronomy, University of Utah, Salt Lake City, UT 84112, USA

[17]Department of Physics and Astronomy, University of Iowa, Van Allen Hall, Iowa City, IA 52242, USA

[18]Department of Physics and Astronomy and the Bartol Research Institute, University of Delaware, Newark, DE 19716, USA

[19]Enrico Fermi Institute, University of Chicago, Chicago, IL 60637, USA

[20]Department of Physics and Astronomy, Iowa State University, Ames, IA 50011, USA

[21]Kavli Institute for Cosmological Physics, University of Chicago, Chicago, IL 60637, USA

[22]Department of Life and Physical Sciences, Galway-Mayo Institute of Technology, Dublin Road, Galway, Ireland

[23]School of Physics and Center for Relativistic Astrophysics, Georgia Institute of Technology, 837 State Street NW, Atlanta, GA 30332-0430

[24]CRESST and Astroparticle Physics Laboratory NASA/GSFC, Greenbelt, MD 20771, USA.

[25]University of Maryland, Baltimore County, 1000 Hilltop Circle, Baltimore, MD 21250, USA.

[26]Instituto de Astronomia y Fisica del Espacio, Casilla de Correo 67 - Sucursal 28, (C1428ZAA) Ciudad Autnoma de Buenos Aires, Argentina

[27]Physics Department, California Polytechnic State University, San Luis Obispo, CA 94307, USA

[28]Department of Applied Physics and Instrumentation, Cork Institute of Technology, Bishopstown, Cork, Ireland

[29]Argonne National Laboratory, 9700 S. Cass Avenue, Argonne, IL 60439, USA

[30]Laboratoire Leprince-Ringuet, École polytechnique, CNRS/IN2P3, Palaiseau, France

[31]Department of Astronomy and Astrophysics, University of California, 1156 High Street, Santa Cruz, CA 95064

[32]Department of Astronomy and Astrophysics, UCO/Lick Observatory, University of California, 1156 High Street, Santa Cruz, CA 95064

[33]Astrophysical Institute, Department of Physics and Astronomy, Ohio University, Athens, OH 45701, USA

Appendix C

Full Author List for 'The Blazar Emission Environment: Insight from Soft X-ray Absorption

A. Furniss[1], M. Fumagalli[2,3,4], D. A. Williams[1] and A. Falcone[5]

[1]Santa Cruz Institute of Particle Physics and Department of Physics, University of California Santa Cruz, 1156 High Street, Santa Cruz, CA 95064, USA.

[2]Carnegie Observatories, 813 Santa Barbara Street, Pasadena, CA 91101, USA.

[3]Department of Astrophysics, Princeton University, Princeton, NJ 08544-1001, USA.

[4]Hubble Fellow

[5]Department of Astronomy and Astrophysics, 525 Davey Lab, Pennsylvania State University, University Park, PA 16802, USA

Appendix D

Full Author List for ApJ 766, 35 (2013)

A. Furniss[1], M. Fumagalli[2,3,4], C. Danforth[5], D. A. Williams[1] and J. X. Prochaska[6]

[1]Santa Cruz Institute of Particle Physics and Department of Physics, University of California Santa Cruz, 1156 High Street, Santa Cruz, CA 95064, USA.

[2]Carnegie Observatories, 813 Santa Barbara Street, Pasadena, CA 91101, USA.

[3]Department of Astrophysics, Princeton University, Princeton, NJ 08544-1001, USA.

[4]Hubble Fellow

[5]CASA, Department of Astrophysical and Planetary Sciences, University of Colorado, 389-UCB, Boulder, CO 80309, USA.

[6]Department of Astronomy and Astrophysics, UCO/Lick Observatory, University of California, 1156 High Street, Santa Cruz, CA 95064, USA.

Appendix E

Full Author List for ApJL, 786, 31 (2013)

A. Furniss[1], D. A. Williams[1], C. Danforth[2], M. Fumagalli,4,5[3], J. X. Prochaska[6], J. Primack[1], C. M. Urry[7], J. Stocke[2], A. V. Filippenko[8], and W. Neely[9]

[1]Santa Cruz Institute of Particle Physics, and Department of Physics, University of California Santa Cruz, 1156 High Street, Santa Cruz, CA 95064, USA.

[2]CASA, Department of Astrophysical and Planetary Sciences, University of Colorado, 389-UCB, Boulder, CO 80309, USA.

[3]Carnegie Observatories, 813 Santa Barbara Street, Pasadena, CA 91101, USA.

[4]Department of Astrophysics, Princeton University, Princeton, NJ 08544-1001, USA.

[5]Hubble Fellow.

[6]Department of Astronomy and Astrophysics, UCO/Lick Observatory, University of California, 1156 High Street, Santa Cruz, CA 95064, USA.

[7]Department of Astronomy, Yale University, New Haven, CT 06520-8120.

[8]Department of Astronomy, University of California, Berkeley, CA 94720-3411.

[9]NF/

Bibliography

Abdo, A. et al. 2009a, Astroparticle Physics, 32, 193

Abdo, A. A., Ackermann, M., Ajello, M. et al. 2009b, ApJL, 706, 138

Abdo, A. et al. 2010a, ApJS, 188, 405

Abdo, A. A., Ackermann, M., Ajello, M. et al. 2010b, ApJ, 715, 429

Abdo, A. et al. 2010c, ApJ, 716, 30

Abdo, A. A., Ackermann, M., Ajello, M. et al. 2011, ApJ, 726, 43

Abramowski, A., Acero, F., Aharonian, F. et al. 2012, arXiv:1204.1964

Abrassart, A. & Czerny, B. 2000, A&A, 356, 475

Acciari, V., Aliu, E., Arlen, T. et al. 2008, ApJ, 679, 142

Acciari, V., Aliu, E., Arlen, T. et al. 2009a, ApJ, 693, 104

Acciari, V. A., Aliu, E., Arlen, T. et al. 2009b, ApJ, 695, 1370

Acciari, V. A. et al. 2009c, ApJ, 707, 612

Acciari, V., Aliu, E., Arlen, T. et al. 2010, ApJL, 708, 100

Acciari, V. A.. Aliu, E., Arlen, T. et al. 2010, ApJ, 715, 49

Achterberg, A., Gallant, Y., Kirk, J. & Guthmann, A. 2001, MNRAS, 328, 393

Ackermann et al. 2011, ApJ, 743, 171

Aharonian,F., Coppi, P. & Volk, H. 1994, ApJL, 423, 5

Aharonian, F., Belyanin, A., Derishev, E., Kocharovsky, V., Kocharovsky, V. 2002, PhysRevD, 66, 023005

Aharonian, F., Akhperjanian, A., Bazer-Bachi, A. et al. 2006, Nature, 440, 1018

Aharonian, F., et al. 2007, ApJL, 664, 71

Aharonian, F., Khanguljan, D. & Costamante, L. 2008, MNRAS, 387, 1206

Aharonian, F., Essey, W., Kusenko, A. & Prosekin, A. 2013, Phys. Rev. D, 87, 063002

Albert, J., Aliu, E., Anderhub, H. et al. 2007, ApJL, 666, 17

Albert, J., Aliu, E., Anderhub, H. et al. 2008a, ApJ, 674, 1037

Albert, J., Aliu, E., Anderhub, H. et al. 2008b, Science, 320, 1752

Alekseè, J. Antonelli, L. A., Antoranz, P. et al. 2011, ApJ, 726, 58

Aleksić J., Alvarez, E. A., Antonelli, L. A. et al. 2012, A&A, 542, 100

Aliu, E., Aune, T., Beilicke, M., et al. 2011a, ApJ, 742, 127

Aliu, E., Aune, T., Beilicke, M. et al. 2011b, ApJ, 743, 62

Aliu, E., Aune, T., Beilicke, M. et al. 2012a, ApJ, 750, 92

Aliu, E., Aune, T., Beilick, M., et al. 2012b, ApJ, submitted

Aliu, E., Arlen, T., Aune, T. et al. 2013a, ApJ, submitted

Aliu, E. et al. 2013b, ApJ in prep.

Appenzeller, I., Thiering, I., Zickgraf, F. et al. 1998, ApJS, 117, 319

Arnal et al. 2000, A&AS, 142, 35

Atwood, W. B., et al. 2009, ApJ, 697, 1071

Bajaja et al. 2005, A&A, 440, 767

Bauer, F., Condon, J., Thuan, T., Broderick, J. 2000, ApJS, 129, 547

Becherini, Y., Boisson, C., & Cerruti, M. 2012, AIP Conference Series, 1505, 490

Becker, R. et al. 1991, ApJS, 75, 1

Bednarek, W. 1993, ApJL, 402, 29

Berge, D., Funk, S., Hinton, J. 2007, A&A, 466, 1219

Bondi, M., Marcha, M., Dallacasa, D., Stanghellini, C. 2001, MNRAS, 325, 1109

Bonning, E., Urry, C. M., Bailyn, C. et al. 2012, ApJ, 756, 13

Böttcher, M., & Chiang, J., 2002, ApJ, 581, 127

Böttcher, M. & Dermer, C. D. 2002, ApJ, 564, 86

Böttcher, M., 2005, ApJ, 621, 175 (Erratum: ApJ, 641, 1233 [2006])

Böttcher, M. 2007, Ap&SS, 309, 95B

Böttcher, M., 2010, in proc. of "Fermi Meets Jansky", eds. T. Savolainen, E. Ros, R. W. Porcas, & J. A. Zensus; p. 41

Bramel, D. A., Carson, J., Covault, C. E. et al. 2005, ApJ, 629, 108

Brinkmann, W., Siebert, J., Feigelson, E. D et al. 1997, A&A, 323, 739

Brinkmann, W., Laurent-Muehleisen, S., Voges, W. et al. 2000, A&A, 356, 445

Burrows, D.N., Hill, J.E., Nousek, J.A., et al. 2005, SSR, 120, 165

Butcher, H., Oemler, A. Tapia, S. & Tarenghi, M. 1976, ApJL, 209, 11

Cash, W. 1979, ApJ, 228, 939

Cardelli, J., Clayton, G., Mathis, J. 1989, ApJ, 345, 245

Cogan, P. 2008, Proc. 30th Int. Cosmic Ray Conf., Vol 3, The VERITAS Gamma-ray Analysis Suite, ed. R. Caballero, J. C. D'Olivo, G.Medina-Tanco, L. Nellen, F. A. Sánchez & J. F. Valdeé-Galicia (Mexico City, Mexico: Universidad Nacional Autónoma de México), 1385

Colla, G., Fanti, C., Fanti, R. et al. 1973, A&AS, 11, 291

Costamante, L. et al. 2001, A&A, 371, 512

Costamante, L. & Ghisellini, G. 2002, A&A, 384, 56

Danforth, C. W., & Shull, J. M. 2008, ApJ, 679, 194

Danforth, C. W., Keeney, B. A., Stocke, J. T., Shull, J. M., & Yao, Y. 2010, ApJ, 720, 976

Danforth, C. W., Nalewajko, France & Keeney 2013a, ApJ 764, 57

Danforth, C. W. et al. 2013b, *in prep.*

Daniel, M. 2008, Proc. 30th Int. Cosmic Ray Conf., Vol 3, The VERITAS Standard Data Analysis, ed. R. Caballero, J. C. D'Olivo, G.Medina-Tanco, L. Nellen, F. A. Sánchez & J. F. Valdeé-Galicia (Mexico City, Mexico: Universidad Nacional Autónoma de México), 1325

A. Dar & A. Laor 1997, ApJL, 478, 5

Dermer, C., Schlickeiser, R., Mastichiadis, A. 1992, A&A, 256, 27

Dermer, C., Murase, K., & Takami, H. 2012, ApJ, 755, 147

Dimitrakoudis, S. et al. 2012, Int. Jour. Modern Physics Conf. Ser., 8, 19

Dominguez, A., Primack, J., Rosario, F. et al. 2011, MNRAS, 410, 2556

Dominguez, A. et al. 2013, ApJ, accepted

Dwek, E. & Krennrich, F. 2005, ApJ, 618, 657

Essey, W. & Kusenko, A., 2012, ApJ, 751, 11

Evans, P., Beardmore, A. P. Page, K. L. et al. 2009, MNRAS, 397, 1177

Ficarra, A., Grueff, G., Tomassetti, G. 1985, A&AS, 59, 255

Filippenko, A. V., Li, W. D., Treffers, R. R., & Modjaz, M. 2001, in Small-Telescope Astronomy on Global Scales, ed. W. P. Chen, C. Lemme, & B. Paczyński (San Francisco: Astron. Soc. Pacific, Conf. Ser. Vol. 246), 121

Fitzpatrick, E. 1999, PASP, 111, 63

Finke, J., Shields, J. Böttcher, M. & Basu, S. 2008, A&A, 477, 513

Finke, J. et al. 2010, ApJ, 712, 238

Fischer, J., Hasinger, G., Schwope, A. et al. 1998, Astron. Nachr., 319, 347

Fomin, V. P. et al. 1994, Astropart. Phys., 2, 137

Fossati, G., Maraschi, L., Celotti, A., Comastri, A., Ghisellini, G. 1998, MNRAS, 299, 433

Franceschini, A., Rodighiero, G., & Vacciari, M. 2008, A&A, 487, 837

Fumagalli, M. et al. 2012, MNRAS, 424, 2276

Furniss, A. et al. 2013a, ApJ, 766, 35

Furniss, A. et al. 2013b, ApJL, 786, 31

Furniss, A., Fumagalli, M., Falcone, A. & Williams, D. A. 2013c, ApJ, accepted

Gehrels, N. et al. 2004, ApJ, 611, 1005

Ghavamian, P. et al. 2009, COS Instrument Science Report 2009-01(v1), Preliminary Characterization of the Post-Launch Line Spread Function of COS (Baltimore: STScI)

Ghisellini, G. et al. 1998, MNRAS, 301, 451

Ghisellini, G. & Tavecchio, F. 2008, MNRAS, 387, 1669

Gilmore, R. et al. 2009, MNRAS, 399, 1694

Gilmore, R., Somerville, R., Primack, J. & Dominguez, A. 2012, MNRAS, 422, 3189

Giommi, P. et al. 2005, A&A, 434, 385

Glover, S. & Clark, P. C. 2012, MNRAS, 421, 9

Gould, R. J. & Shréder, G. 1967, Phys. Rev. 155, 1408

Graff, P. et al. 2008, ApJ, 689, 68

Grauer, A. D., Neely, A. W., & Lacy, C. H. S. 2008, PASP, 120, 992

Haakonsen, C. B. et al. 2009, ApJS, 184, 138

Hales, S., Masson, C., Warner, P. & Baldwin, J. 1990, MNRAS, 246, 256

Hartmann, D., & Burton, W. B. 1997, Atlas of Galactic Neutral Hydrogen (Cambridge University Press), ISBN 0521471117

Hauser, M. & Dwek, E. 2001, ARAA, 39, 249

Healey, S. et al. 2007, ApJS, 171, 61

Helene, O. 1983, Nuclear Instruments & Methods in Physics Research, 212, 319

Ho, L. C. 2008, ARA&A, 46, 475

Hoffman, W. 2010, ATel #2743

Holder, J., Bond, I. H., Boyle, P. J. et al. 2003, ApJL, 583, 9

Holder, J. et al. 2006, Astropart. Phys., 25, 391

Horan, D. & Wakely, S. 2008, HEAD, 10.4106

Horns, D. & Meyer, M. 2012, JCAP, 2, 33

Kalberla, P. et al. 2005, A&A, 440, 775

Kaplan et al. 2012, in preparation

Keeney, B. A., Danforth, C. W., Stocke, J. T., France, K., & Green, J. C. 2012, PASP, 124, 830

Kelner, S. R. & Aharonian, F. A., 2008, Phys. Rev. D., 78, 3, 034013

Kinney, A. L., Bohlin, R. C., Blades, J.C. & York, D. G. 1991, ApJS, 75, 645

Kirsch, M. G., Briel, U. G., Burrows, D. et al. 2005, SPIE, 5898, 22

Kneiske, T. M. & Dole, H. 2010, A&A, 515, 19

Kusunose, M. & F. Takahara 2006, ApJ, 651, 113

Krawczynski, H., Carter-Lewis, D., Duke, C. et al. 2006, APh 25, 380

Kriss, G. A. 2011, COS Instrument Science Report 2011-01(v1), Improved Medium Resolution Line Spread Functions for COS FUV Spectra (Baltimore: STScI)

Krumholz, M. McKee, C. F., &Tumlinson, J. 2009, ApJ 693, 216

Laurent-Muehleisen, S., Kollgaard, R., Ciardullo, R. et al. 1998, ApJS, 118, 127

Laurent-Muehleisen, S., Kollgaard, R., Feigelson, E., Brinkmann, W., Siebert, J. 1999, ApJ, 525, 127

Lefa, E., Rieger, F. M. & Aharonian, F. 2011a, ApJL, 740, 64L

Lefa, E., Aharonian, F., & Rieger, F. 2011b, ApJL, 743, 19L

Li, T. & Ma, Y. 1983, ApJ, 272, 317

Liu, H. T. & Bai, J. M. 2006, ApJ, 653,1089

Mannheim, K. 2000, A&A, 269, 67

Maraschi, L., Ghisellini, G. Celotti, A. 1992, ApJL, 397, 5

Marcha, M. et al. 1996, MNRAS, 281, 425

Mariotti, M. 2011a, ATel #3100

Mariotti, M. 2011b, ATel #3719

A. Marscher & R. Protheroe 2000, AIPC, 515, 149

Mazin, D. & Raue, M. 2007, A&A, 471, 439

Mazin, D., Lindfors, E., Berger, K. et al. 2009, eprint arXiv:0907.0366

Marziani, P., Sulentic, J. W., Dultzin-Hacyan, D., Calvani, M. & Moles, M. 1996, ApJS, 104, 37

Massaro, F. et al. 2004, A&A, 413, 489

Massaro, F. et al. 2006, A&A, 448, 861

Massaro, F., Tramacere, A., Cavaliere, A., Perri, M. & Giommi, P. 2008, A&A, 478, 395

Matsuoka, M. et al. 2009, PASJ, 61, 999

Mattox, J. et al. 1996, ApJ, 461, 396

Meli, A., & Quenby, J., 2003, ApJ, 19, 649

Meisner, A. & Romani, R. 2010, ApJ, 712, 14

Meyer, E., Fossati, G., Georganopoulos, M. & Lister, M. 2011, ApJ, 740, 98

Mickaelian, A., Hovhannisyan, L., Engels, D., Hagen, H. & Voges, W. 2006, A&A, 449, 425

Miller, J. S., French, H. B., & Hawley, S. A. 1978, in Pittsburgh Conf. BL Lac Objects, ed. A. M. Wolfe, 176

Morrison, R. & McCammon, D. 1983, ApJ, 270, 119

Motch, C. et al. 1998, A&AS, 132, 341

A. Mücke & R. Protheroe 2000, AIPC, 515, 149

Mukherjee, R. 2001, AIP Conf. Proc., 558, 324

Mushotzky, R., Done, C. & Pounds, K. 1993, ARA&A, 31, 717

Nass, P., Bade, N., Kollgaard, R. et al. 1996, A&A, 309, 419

Nieppola, E., Tornikoski, M., Valtaoja, E. 2006, A&A, 445, 441

Nikishov, A. I. 1962, JETP, 14, 393

Nolan, P. L., Abdo, A. A., Ackermann, M. et al. 2012, ApJS, 199, 31

Ong, R. 2010a, ATel #2786

Ong, R. 2010b, ATel #2301

Ong, R. 2010c, ATel #2309

Orr, M., Krennrich, F. & Dwek, E. 2011, ApJ, 733, 77

Padovani, P. & Giommi, P., 1995, ApJ, 444, 567

Paggi, A., Massaro, F., Vittorini, V. et al. 2009, A&A, 504, 821

Penton, S. V., Shull, J. M., & Stocke, J. T. 2000, ApJ, 544, 150

Penton, S. V., Stocke, J. T., & Shull, J. M. 2004, ApJS, 152, 29

Perlman, E. S. 2000 AIP Conf. Proc., 515, 53

Piranomante, S., Perri, M., Giommi, P. Landt, H. & Padovani, P. 2007, A&A, 470, 787

Pita, S., Goldoni, P., Boisson, C. et al. 2012, AIP Conference Series, 1505, 566

Prandini, E., Bonnoli, G., Maraschi, L., Mariotti, M. & Tavecchio, F. 2010, MNRAS, 405, 76

Pohl, M. & Schlickeiser, R. 2000, A&A, 354, 395

Poole et al. 2008, MNRAS, 383, 627

Poutanen, J. & Stern, B. 2010, ApJL, 717, 118

Primack, J., Bullock, J., Somerville, R. 2005, AIPC, 745, 23

Primack, J., Domnguez, A., Gilmore, R., & Somerville, R. 2011, AIPC, 1381, 72

Reimer, A. Böttcher, M. & Postnikov, S. 2005, ApJ, 630, 186

Rolke, A., Wolfgang, A., López & A. Conrad, J. 2005, Nucl. Instrum. Meth, A551, 493

Roming, P., Koch, T., Oates, S. et al. 2009, ApJ, 690, 163

Rybicki, G. B. & Lightman, A. P. 1979, Radiative Processes in Astrophysics (New York:Wiley)

Sbarufatti, B. et al. 2005, ApJ, 635, 173

Scarpa, R. & Falomo, R. 1995, A&A, 303, 656

Scatcher, J. et al. 1993, ApJ, 412, 541

Shlegel, D. et al. 1998, ApJ, 500, 525

Sikora, M., Begelman, M. & Rees, M. 1994, ApJ, 421, 153

Sironi, L., & Spitkovsky, A. 2011, ApJ, 726, 75

Stecker, F., de Jager, O. & Salamon, M. 1992, ApJL, 390, 49

Stecker, F. & de Jager, O. 1993, ApJL, 415, 71

Stecker, F. W. et al. 1996, ApJL, 473, 75

Stecker, F., Malkan, M. & Scully S. 2006, ApJ, 648, 774

Summerlin, E. J. et al. 2012, ApJ, 745, 63

Tagliaferri, G. et al. 2003, A&A, 412, 711

Tagliaferri, G. et al. 2008, ApJ, 679, 1029

Tavecchio, F., Maraschi, L., Ghisellini, G. et al. 2002, ApJ, 575, 137

Tavecchio, F. & Mazin, D. 2009, MNRAS, 392, 40

Teshima, M. 2009, Astronomer's Telegram, #2098

Thompson, D., Bertsch, D., Fichtel, C. et al. 1993, ApJS, 86, 629

Tielenn & Hollenbach, D. 1985, ApJ, 291, 722

Tramacere, A. et al. 2007, A&A, 467, 501

Tramacere, A., Massaro, E. & Taylor, A. M. 2011, ApJ, 739, 66

Trump, J. R. et al. 2011, ApJ, 733, 60

Turriziani, S., Cavazzuti, E. & Giommi, P. 2007, A&A, 472, 699

Urry, C. M. & Padovani 1995, PASP, 107, 803

Vagnetti, F., Turriziani, S. & Trevese, D. 2011, A&A, 536, 84

Virtanen, J. et al. 2005, ApJ, 621, 313

Wachter, K., Strauss, M. & Filippenko, A. 1988, ApJ, 330, 91

Weekes, T. C. et al. 2002, Astropart. Phys., 17, 221

Werner, M., Roellig, T. L., Low, F. J., et al. 2004, ApJS, 154, 1

Wurtz, R., Ellingson, E., Stocke, J. & Yee, H. 1993, AJ, 106, 869

Wurtz, R., Stocke, J., Ellingson, E. & Yee, H. 1997, ApJ, 480, 547

Yang, J. & Wang, J. 2010, A&A, 522, 12

Young, J. S. et al. 1991, ARA&A, 29, 581